Charged particle motion and radiation in strong electromagnetic fields

A. Gonoskov, T. G. Blackburn, and M. Marklund

Department of Physics, University of Gothenburg, SE-41296 Gothenburg, Sweden

S. S. Bulanov

Lawrence Berkeley National Laboratory, Berkeley, California 94720, USA

(published 7 October 2022)

The dynamics of charged particles in electromagnetic fields is an essential component of understanding the most extreme environments in our Universe. In electromagnetic fields of sufficient magnitude, radiation emission dominates the particle motion and effects of quantum electrodynamics (QED) in strong fields are crucial, which triggers electron-positron pair cascades and counterintuitive particle-trapping phenomena. As a result of recent progress in laser technology, high-power lasers provide a platform to create and probe such fields in the laboratory. With new large-scale laser facilities on the horizon and the prospect of investigating these hitherto unexplored regimes, this review explores the basic physical processes of radiation reaction and QED in strong fields, how they are treated theoretically and in simulation, the new collective dynamics they unlock, recent experimental progress and plans, and possible applications for high-flux particle and radiation sources.

DOI: 10.1103/RevModPhys.94.045001

CONTENTS

I. INTRODUCTION

Over the last 100 years elementary particle physics has made tremendous progress in the exploration of the high-energy regime, culminating in the standard model and its verification at grand-scale experimental facilities such as LEP, LEP II, SLAC, Tevatron, and LHC. A new pathway in fundamental physics research has opened by the use of electromagnetic fields of focused laser pulses to explore the high-intensity regime. Here the high density and the simultaneous interaction of the participating particles provide a fruitful basis for the creation of extreme environments, which can be described theoretically only using nonperturbative methods in quantum electrodynamics (QED). While powerful, this theory is insufficient outside highly idealized interaction configurations or when collective dynamics dominate. Understanding how single-particle QED processes couple to large-scale plasma phenomena, and vice versa, is a significant unsolved problem. Experimental investigation of this little-explored regime is therefore of fundamental interest, as well as being of practical importance. This includes the effects of extreme environments on the next generation of particle accelerators and the formation of dense electron-positron plasmas, which occur in astrophysical phenomena and could be exploited to create extraordinary particle and radiation sources. In light of this, the purpose of this review is to assess the current state of the art in our theoretical understanding of the strong-field regime and upcoming experimental programs aimed at the exploration of such opportunities.

Increasingly strong electromagnetic (EM) fields significantly modify particle dynamics, thereby giving rise to phenomena that are not encountered in either classical or perturbative quantum theories of these interactions. To illustrate this, we consider the "cube of theories" shown in Fig. 1, which was proposed by Bulanov, Schroeder *et al.* (2013) in analogy with the cube shown by Okun' (1991). This cube has three orthogonal axes, defined by the constants c (the speed of light in vacuum), $\hbar$ (the reduced Planck's constant), and E_{cr} (the critical field of quantum electrodynamics, which does equal the electron rest energy over a single Compton length). These three axes give the strength of relativistic, quantum, and strong-field effects, respectively. Each vertex of the cube corresponds to a physical theory: $(0,0,0)$ is nonrelativistic mechanics, $(c,0,0)$ is special relativity, and $(0,\hbar,0)$ is quantum mechanics. Quantum field theory, which combines quantum and relativistic effects, is found at $(c,\hbar,0)$. Classical electrodynamics corresponds to the vertex $(c,0,E_{\mathrm{cr}})$ and atomic, molecular, and optical physics corresponds to $(0,\hbar,E_{\mathrm{cr}})$. The vertex that interests us is located at $(c,\hbar,E_{\mathrm{cr}})$, which encompasses strong-field quantum electrodynamics (SFQED).

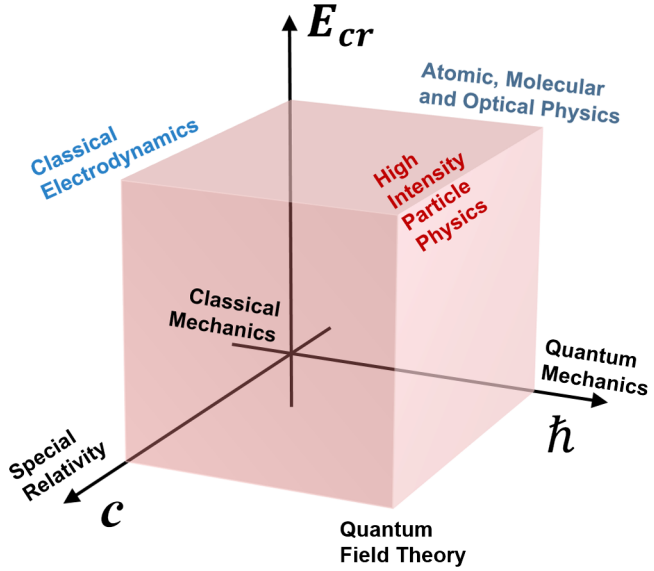

FIG. 1. Cube of theories. Its three axes correspond to relativistic (c), quantum ($\hbar$), and high-intensity effects (E_{cr}) and its vertices correspond to the theories: $(0,0,0)$ is classical mechanics; $(c,0,0)$ is special relativity; $(0,\hbar,0)$ is quantum mechanics; $(c,\hbar,0)$ is quantum field theory; $(c,0,E_{\mathrm{cr}})$ is classical electrodynamics; $(0,\hbar,E_{\mathrm{cr}})$ is atomic, molecular, and optical physics; and $(c,\hbar,E_{\mathrm{cr}})$ is high-intensity particle physics. Here $E_{\mathrm{cr}} = m^2c^3/e\hbar$ is the critical field of QED, where m is the electron mass and e is the elementary charge. Adapted from Bulanov, Schroeder *et al.*, 2013.

The "strong-field" aspect of quantum electrodynamics significantly alters the physics of the interactions, as we discuss in this review. With the increase of field strength, the interaction between particles and electromagnetic fields enters the so-called radiation-dominated regime, and as the particle energies increase nonlinear quantum effects then come into play. These phenomena fall under the umbrella of "high-intensity particle physics," a new, emerging branch of physics that occupies a significant region in the standard model parameter space and is largely unexplored. It is crucial for understanding extreme astrophysical environments, including neutron stars, magnetars, and black holes, and will be important for the design of future lepton and γ-γ colliders.

The reason that interest in this field has grown significantly in recent years is the progress in the development of large-scale, high-intensity laser facilities (Danson *et al.*, 2019) in the "petawatt revolution" following the invention of chirped pulse amplification (CPA) (Strickland and Mourou, 1985). Indeed, the intensities achieved over the past decade have now reached 10^{23} W cm^{-2} (Yoon *et al.*, 2021).

Until recently experimental studies were limited to a single example from the 1990s, namely, E144 at SLAC, where a 46.5 GeV electron beam interacted with a 10^{18} W/cm^2 laser pulse, producing high-energy photons, which in turn transformed into electron-positron pairs in the electromagnetic field of the laser pulse (Bula *et al.*, 1996; Burke *et al.*, 1997). The situation changed with two experiments on radiation reaction at the Rutherford Appleton Laboratory, which reported radiative energy loss, and quantum corrections

thereto, of an electron beam in the interaction with a counterpropagating, high-intensity laser pulse (Cole *et al.*, 2018; Poder *et al.*, 2018).

Today experiments on radiation emission and pair creation in the strong-field regime form part of the planned experimental programs at almost every major petawatt or multipetawatt laser facility, including the Extreme Light Infrastructure (ELI) (Weber *et al.*, 2017; Gales *et al.*, 2018), Apollon (Papadopoulos *et al.*, 2016), the Station of Extreme Light (Cartlidge, 2018), the Center for Relativistic Laser Science (CoReLS) (Yoon *et al.*, 2021), J-KAREN-P (Kiriyama *et al.*, 2020), the Omega Laser Facility (Bromage *et al.*, 2019), and the Zetawatt-Equivalent Ultrashort Pulse Laser System (ZEUS) (Nees *et al.*, 2020), as well as conventional accelerator facilities (Abramowicz *et al.*, 2019; Meuren, 2019).

A. The strong electromagnetic field

When we characterize an electromagnetic field as "strong" or "weak," we implicitly compare its magnitude to a scale of some kind. The theory of quantum electrodynamics defines such a scale through the electron mass m, which yields a characteristic energy mc^2, length $ƛ = \hbar/mc$, and the elementary charge e:

$$E_{\mathrm{cr}} = \frac{m^2c^3}{e\hbar} = 1.323 \times 10^{18}\ \mathrm{V\,m^{-1}}. \tag{1}$$

We refer to Eq. (1) as the *critical field of quantum electrodynamics*. Such a field does work equal to the electron rest energy over a reduced Compton length $ƛ = 3.86 \times 10^{-11}$ cm; the gyroradius r_c of an electron in a magnetic field of equivalent strength ($B_{\mathrm{cr}} = E_{\mathrm{cr}}/c = 4.41 \times 10^9$ T) would be $r_c = ƛ$. E_{cr} is often called the Schwinger field, in honor of Schwinger (1951), although it previously appeared in the work of Sauter (1931) and Heisenberg and Euler (1936). It is constructed from fundamental constants and is therefore ubiquitous in the study of quantum effects in strong electromagnetic fields (Di Piazza *et al.*, 2012).

It is possible to define an equivalent of Eq. (1) within the framework of classical electrodynamics by exchanging the Compton length $ƛ = \hbar/mc$ for the classical electron radius $r_e = e^2/4\pi\epsilon_0 mc^2 = 2.82 \times 10^{-13}$ cm:

$$E_{\mathrm{cr}}^{\mathrm{clas}} = \frac{4\pi\epsilon_0 m^2c^4}{e^3} = \frac{E_{\mathrm{cr}}}{\alpha} = 1.813 \times 10^{20}\ \mathrm{V\,m^{-1}}. \tag{2}$$

The *classical critical field* in Eq. (2) is larger than the QED-critical field by a factor of $1/\alpha$, where $\alpha \simeq 1/137$ is the fine-structure constant, which hints that quantum effects lead the hierarchy of corrections to the usual Lorentz force equation; see Sec. II.A.1.

Both classical and quantum electrodynamics are relativistic theories, so the comparison of a field strength to E_{cr} (or $E_{\mathrm{cr}}^{\mathrm{clas}}$) must be done in a way that is invariant under Lorentz transformations. The quantities available to us are the particle four-momentum $p^\mu = \gamma m(c, \mathbf{v})$ and the field tensor $F_{\mu\nu}$. Here $\gamma = (1 - \mathbf{v}^2/c^2)^{-1/2}$ is the Lorentz factor associated with three-velocity $\mathbf{v}$. The equivalent quantity for a photon with wave vector $\mathbf{k}$ and energy $\hbar\omega$ is the four-vector $\hbar k^\mu = (\hbar\omega/c)(1, \mathbf{n})$, where $\mathbf{n}$ is its unit direction of propagation.

The symmetry properties of $F_{\mu\nu}$ restrict the number of nonzero invariant combinations of p^μ and $F_{\mu\nu}$ to four if the field is constant and homogeneous (Ritus, 1985; Baier, Katkov, and Strakhovenko, 1998). Two are purely field dependent, and two are particle dependent as well. The first two are the following Poincaré invariants (Schwinger, 1951; Dunne, 2005):

$$\mathcal{F} = -\frac{F_{\mu\nu}F^{\mu\nu}}{2E_{\mathrm{cr}}^2} = \frac{\mathbf{E}^2 - c^2\mathbf{B}^2}{E_{\mathrm{cr}}^2}, \tag{3}$$

$$\mathcal{G} = -\frac{F_{\mu\nu}\tilde{F}^{\mu\nu}}{4E_{\mathrm{cr}}^2} = \frac{c\mathbf{B}\cdot\mathbf{E}}{E_{\mathrm{cr}}^2}. \tag{4}$$

In Eqs. (3) and (4) we use the dual field tensor $\tilde{F}_{\mu\nu} = (1/2)\epsilon_{\mu\nu\alpha\beta}F^{\alpha\beta}$, where $\epsilon_{\mu\nu\alpha\beta}$ is the antisymmetric tensor, and implicitly sum over repeated indices. Replacing $F_{\mu\nu}$ with $\tilde{F}_{\mu\nu}$ in Eqs. (5) and (6) yields the same invariants. Additional combinations are possible if the field is not homogeneous (in the four-dimensional sense), involving terms of the form $\partial_\mu F^{\alpha\beta}$. There is no contribution from terms such as $\partial_\mu F^{\mu\nu}$ and $\partial_\mu \tilde{F}^{\mu\nu}$, as these are zero by virtue of Maxwell's equations.

The physical meaning of these invariants is as follows. A field that satisfies $\mathcal{F} > 0$ and $\mathcal{G} = 0$ is *electric type* and is unstable against spontaneous decay to electron-positron pairs (Schwinger, 1951). This occurs for any field magnitude in principle, but it is exponentially suppressed unless $\mathcal{F} \gtrsim 1$. (This is equivalent to $\mathbf{E}^2 \gtrsim E_{\mathrm{cr}}^2$ if $\mathbf{E}^2 \gg c^2\mathbf{B}^2$.) Fields of *magnetic type*, with $\mathcal{F} < 0$ and $\mathcal{G} = 0$, are stable against vacuum pair creation but do induce birefringence effects (Erber, 1966; Marklund and Shukla, 2006). A special role is played by *crossed fields*, in which the electric and magnetic fields are mutually perpendicular and have equal magnitudes (up to a factor of c, $|\mathbf{E}| = c|\mathbf{B}|$) because of the possibility of approximating an arbitrary electromagnetic field as a crossed field under certain conditions (Nikishov and Ritus, 1964; Ritus, 1985). (We return to this point in Sec. II.B.4.) Crossed fields are not susceptible to vacuum pair creation, regardless of their amplitude (Heisenberg and Euler, 1936; Schwinger, 1951).

The two invariants that mix particle and field properties are the *quantum nonlinearity parameters*[1]:

[1]The literature includes alternative notation for χ_e such as Υ (Erber, 1966; Chen, 1992; Harding and Lai, 2006) and η (Bell and Kirk, 2008). Note also that it is possible for χ_γ to be defined by normalizing the photon energy $\hbar\omega$ to $2mc^2$, rather than mc^2 as we did here, particularly in the astrophysical literature (Erber, 1966; Harding and Lai, 2006). The rationale for doing so is that electron-positron pair creation by a photon creates two particles of mass m, so $2mc^2$ is a natural energy scale.

$$\chi_e = \frac{\sqrt{-(F_{\mu\nu}p^\nu)^2}}{mcE_{\rm cr}} = \gamma\frac{\sqrt{(\mathbf{E}+\mathbf{v}\times\mathbf{B})^2-(\mathbf{E}\cdot\mathbf{v}/c)^2}}{E_{\rm cr}}, \tag{5}$$

$$\chi_\gamma = \frac{\hbar\sqrt{-(F_{\mu\nu}k^\nu)^2}}{mcE_{\rm cr}} = \frac{\hbar\omega}{mc^2}\frac{\sqrt{[\mathbf{E}+(c^2\mathbf{k}/\omega)\times\mathbf{B}]^2-[\mathbf{E}\cdot(c\mathbf{k}/\omega)]^2}}{E_{\rm cr}}. \tag{6}$$

Hereafter, wherever the distinction is not necessary, we use the term particle in relation to both photons and electrons (positrons), denoting the corresponding quantities by the subscripts γ and e, respectively. We omit the subscript in situations where it is clear that we are referring to either a photon or an electron or positron.

For the electron, χ_e compares the field strength observed in its instantaneous rest frame with $E_{\rm cr}$ (Ritus, 1985), or the typical energy of the radiation spectrum ($\simeq\hbar\omega_c$), the synchrotron critical frequency; see Eq. (22) with its energy γmc^2 (Sokolov and Ternov, 1968). It therefore parametrizes the importance of quantum corrections to the particle dynamics and radiation emission.

A photon does not have a rest frame, so a physical interpretation of χ_γ is obtained by considering the following argument (Bassompierre *et al.*, 1995). For a photon with momentum $\hbar\omega\mathbf{n}/c$, embedded in an electromagnetic field, to create an electron-positron pair there must be a transfer of energy from the field of $\Delta\mathcal{E}\simeq m^2c^4/\hbar\omega$. This energy transfer must take place over $\Delta t\simeq mc/eE_{\rm eff}$, the time taken for the electron and positron to gain a transverse momentum of mc if the field has an effective magnitude $E_{\rm eff}=\gamma|\mathbf{E}_\perp+c\mathbf{n}\times\mathbf{B}|$ (we have assumed that $\hbar\omega\gg mc^2$ and $\gamma\gg1$). The uncertainty principle requires that $\Delta\mathcal{E}\Delta t<\hbar$ or, equivalently, that $\chi_\gamma>1$. This condition then defines the regime where electron-positron pair creation becomes probable.

In a null field, where $\mathcal{F}=\mathcal{G}=0$, it is χ_e and χ_γ that control the importance of quantum effects. A crossed field is a null field where the electric and magnetic fields have the same magnitude (up to a factor of c) and are perpendicular to each other. A particularly important case of a crossed field is the plane electromagnetic wave, where the electric and magnetic fields oscillate with an angular frequency ω_0 and the phase fronts propagate along a null wave vector κ^μ. Here the dynamics are characterized by the following additional invariant parameter (Nikishov and Ritus, 1964)[2]:

$$a_0 = \frac{1}{mc^2}\frac{e\sqrt{-(F_{\mu\nu}p^\nu)^2}}{\kappa_\mu p^\mu} = \frac{eE_0}{mc\omega_0}, \tag{7}$$

where $E_0=|\mathbf{E}|=c|\mathbf{B}|$. a_0 is called the normalized amplitude of the wave, the field amplitude in relativistic units (i.e., in units of $mc\omega_0/e$), the strength parameter, or the normalized vector potential. The reason for the last item is that a_0 is often defined as $a_0=e\sqrt{-A_\mu A^\mu}/mc$ using the wave's four potential A^μ; this gives an equivalent result under the conventional choice of Lorenz gauge ($\partial_\mu A^\mu=0$); see the discussions of gauge invariance given by Reiss (1979) and Heinzl and Ilderton (2009). As the transverse momentum acquired by an electron in a wave with potential A^μ is $p_\perp^\mu=eA^\mu$, $a_0=|p_\perp|/mc$ measures the importance of relativistic effects, i.e., the classical nonlinearity of the dynamics.

The parameter a_0 also functions as a measure of the multiphoton, or nonlinear, nature of the electromagnetic interaction. Consider the motion of an electron, driven by a circularly polarized EM wave, in its average rest frame: in this frame, the electron performs circular motion with radius r', angular frequency $\omega'=1/r'$, and constant Lorentz factor $\gamma'=\sqrt{1+a_0^2}$, emitting radiation with a characteristic frequency of $\omega_c'=\gamma'^3/r'$. The effective harmonic order, which indicates how many photons are absorbed, is $n=\omega_c'/\omega'\simeq a_0^3$. From the quantum perspective, Eq. (7) compares the work done by the electromagnetic wave over a Compton length ($eE_0\lambda\!\!\!^{-}$) to the energy of a photon of that wave ($\hbar\omega_0$); if $a_0\gg1$, the interaction is unavoidably nonlinear in the number of participating photons.

An alternative interpretation relates a_0 to the *Keldysh parameter* $\gamma_K=\omega_0\sqrt{2mV_0}/eE_0$, which characterizes the ionization of an atomic electron with binding energy V_0 by an electromagnetic wave with amplitude E_0 and frequency ω_0 (Keldysh, 1965; Popov, 2004). If $\gamma_K\ll1$ (the tunneling regime), the ionization occurs on a timescale much shorter than the period of the wave and the electron tunnels through the potential barrier; if $\gamma_K\gg1$ (the multiphoton regime), simultaneous absorption of several photons promotes the electron to the continuum. The laser strength parameter a_0 is equivalent to $1/\gamma_K$ for $V_0\simeq mc^2$; thus, we identify $a_0\gg1$ as the tunneling regime for SFQED processes (Di Piazza *et al.*, 2012) such as electron-positron pair creation (Reiss, 1962). Finally, we note that a critical normalized vector potential a_0 may be defined as follows by setting $E_0=E_{\rm cr}$ in Eq. (7):

$$a_{\rm cr} = mc^2/\hbar\omega_0. \tag{8}$$

Equation (8) is equivalent to $a_{\rm cr}\approx4.1\times10^5\lambda\!\!\!^{-1}$ [μm].

B. Relevant environments

We now turn to the question of what fields satisfy the criteria to be strong, as defined in Sec. I.A, and where they can be found. Here we discuss the five major cases: the magnetic fields surrounding compact astrophysical objects such as pulsars, magnetars, and black holes; the boosted, collective Coulomb fields of ultrarelativistic, dense lepton bunches, as found at the final focus of conventional particle accelerators; the electric fields around high-Z nuclei; the coherently summed, nuclear electric fields observed by ultrarelativistic leptons traveling through a crystal along an axis of symmetry;

[2]The use of a_0 is conventional in the laser- and plasma-physics communities, but it can be denoted as ξ in the SFQED literature (Di Piazza *et al.*, 2012).

and the electromagnetic fields produced by focusing high-power lasers.

A commonality among these five cases is the exploitation of the relativistic factor γ in Eq. (5); even though an electromagnetic field may be weak in the laboratory frame ($|\mathbf{E}|/E_{\mathrm{cr}} \ll 1$), it can still induce nonlinear quantum effects if it is probed by an ultrarelativistic particle, with γ sufficiently large that $\chi \simeq \gamma|\mathbf{E}|/E_{\mathrm{cr}} \ll 1$. In the majority of scenarios that follow, the origin of this ultrarelativistic particle is external to the field, i.e., electrons are accelerated by some mechanism to $\gamma \gg 1$ before encountering the electromagnetic field.

A distinct class of interactions is possible with high-intensity lasers, which can, at large a_0, accelerate initially stationary electrons to sufficiently high energy to make radiation losses and quantum effects important. In this case the laser plays the role of both accelerator and target (Bell and Kirk, 2008). This fact is crucial to understanding the richness of the dynamics induced in this scenario, which we discuss in Sec. IV.

It is unknown whether fields that satisfy $\mathcal{F} \simeq 1$ rather than $\chi \simeq 1$ can be created using lasers (Bulanov, Esirkepov *et al.*, 2010; Fedotov *et al.*, 2010), as they should trigger electron-positron cascades that efficiently absorb and reflect the electromagnetic energy; see Sec. IV.F.

1. Highly magnetized astrophysical environments

Magnetic fields of extraordinary strength can be found around compact objects, including neutron stars and black holes. A pulsar, for example, is a highly magnetized, rotating neutron star formed after the supernova of a massive star and the collapse of its core. Characteristic values of the magnetic-field strength at the surface B_s (as inferred from the spin-down rate) and the rotation period are 10^7–10^9 T and 1.5 ms–8 s, respectively (Harding and Lai, 2006). The rotation drives a wind of relativistic particles and powers the emission of electromagnetic radiation along the magnetic axis of the pulsar; as energy is lost, the pulsar spins down and the rotation period increases. In the "standard model" of a pulsar, the electric field that is induced by the rotation of its magnetic field is shorted out by an electron-positron plasma (Goldreich and Julian, 1969; Sturrock, 1971), except in small regions where particle acceleration takes place. The creation of this pair plasma is a nonsteady process that is now studied with large-scale simulations of the pulsar magnetosphere (Schoeffler *et al.*, 2019; Chen, Cruz, and Spitkovsky, 2020).

The rotation of the pulsar magnetic field creates a voltage drop across the open field lines large enough to drive the acceleration of electrons and positrons to energies of at least 10 TeV (Harding and Lai, 2006). The combination of high particle energy and strong magnetic field in the region above the polar cap causes cascades of photon emission and electron-positron pair creation (Daugherty and Harding, 1982), with extremely high multiplicity (Timokhin and Harding, 2015). [Photons with energies below the pair-creation threshold can instead drive a *photon splitting* cascade (Adler, 1971; Baring and Harding, 2001).] Coherent emission from pulsars is suspected to be linked to the dynamics of the pair cascade (Sturrock, 1971; Philippov, Timokhin, and Spitkovsky, 2020; Cruz, Grismayer, and Silva, 2021).

Even larger magnetic fields ($B_s \sim 10^{10} - 10^{11}$ T) (Olausen and Kaspi, 2014) are believed to exist near magnetars (Duncan and Thompson, 1992), giving rise to exotic effects such as vacuum birefringence, an observation of which was reported by Mignani *et al.* (2017); see also Capparelli *et al.* (2017). Gamma-ray emission (Hirotani and Pu, 2016) and pair creation (Crinquand *et al.*, 2020) also occur around black holes. Some models of the supermassive black hole at the center of M87 predict that millimeter-wave radio emission is dominated by electron-positron pairs produced by photon-photon collisions that are accelerated by unscreened electric fields (Akiyama *et al.*, 2019).

2. Beam-beam interactions

Lepton colliders use high-energy particle beams to probe fundamental physics at the smallest spatial scales (Schael *et al.*, 2013). These are conventionally electron positron, but there are projects to build muon-antimuon and electron-electron colliders using both conventional and plasma technologies (U.S. Department of Energy, 2016; Cros and Muggli, 2019; Cros *et al.*, 2019; Adolphsen *et al.*, 2022). As the cross sections for the sought-after processes are usually small, high particle flux is needed and therefore the particle beam has to be focused to small radii at the interaction point. The combination of a high Lorentz factor and charge density leads to the creation of strong collective electromagnetic fields, which can deflect the particles of the oncoming beam (Yokoya and Chen, 1992). This deflection, which is focusing (defocusing) for electron-positron (electron-electron) collisions, is known as *disruption* (Hollebeek, 1981; Chen and Yokoya, 1988) and it is associated with the emission of radiation, called *beamstrahlung* (Blankenbecler and Drell, 1987; Noble, 1987).

The power and spectral properties of the beamstrahlung are controlled by the electron quantum parameter χ_e (often referred to as the "beamstrahlung parameter" and denoted by Υ in this context). Its average value is given by (Chen, 1992)

$$\langle \chi_e \rangle \simeq \frac{0.11\mathcal{E}_0[10\ \mathrm{GeV}]Q[\mathrm{nC}]}{\sigma_z[\mu\mathrm{m}](\sigma_x[\mu\mathrm{m}] + \sigma_y[\mu\mathrm{m}])}, \tag{9}$$

where $\mathcal{E}_0$ is the energy of the beams, Q is the charge per bunch, and σ_i are the root-mean-square radii of the charge distribution in the directions parallel (z) and perpendicular (x, y) to the collision axis. The normalized amplitude a_0 can be obtained by treating the beam field as a half-cycle electromagnetic wave with wavelength $\lambda \simeq 4\sigma_z$, i.e., $a_0 \simeq 4.5Q[\mathrm{nC}]/\sigma_\perp[\mu\mathrm{m}]$, for a round beam with $\sigma_\perp = \sigma_x = \sigma_y$ (Del Gaudio *et al.*, 2019).

Beamstrahlung is viewed as undesirable because it reduces the center-of-mass energy of the collision and because both the photons themselves and the secondary electron-positron pairs they can create (Chen and Telnov, 1989) are additional sources of background. In future linear colliders, where the beam energy will exceed 100 GeV, it can be minimized by the use of long, flat particle beams (Behnke *et al.*, 2013; Boland *et al.*, 2016). On the other hand, maximizing χ_e by the use of round beams could lead to a high-luminosity photon-photon

collider (Blankenbecler and Drell, 1988) or a high-brightness source of photons and secondary electron-positron pairs (Del Gaudio *et al.*, 2019) or could facilitate the study of the fully nonperturbative regime of SFQED (Yakimenko *et al.*, 2019b) (see Sec. II.B.5) and might be more advantageous from the point of view of acceleration in the plasma-based colliders (U.S. Department of Energy, 2016; Cros and Muggli, 2019; Cros *et al.*, 2019). Codes that simulate beam-beam interactions, accounting for the relevant strong-field processes of photon emission and pair creation (see Sec. II.B.4), include CAIN (Chen *et al.*, 1995), a successor to ABEL (Yokoya, 1986), and GUINEA-PIG++ (Rimbault *et al.*, 2007).

3. Nuclear electric fields

The Coulomb field of a heavy atomic nucleus can be strong in the sense outlined in Sec. I.A if the number of protons $Z \gg 1$; for example, the field strength at the radius of the $1s$ orbital is given by $\mathcal{F}^2 \simeq (\alpha Z)^6$. Indeed, there is a critical value of $Z = Z_{\mathrm{cr}}$ above which the lowest energy bound state falls into the Dirac sea, i.e., the negative-energy continuum, and spontaneous electron-positron pair creation becomes probable (Reinhardt and Greiner, 1977). This threshold is estimated to be $Z_{\mathrm{cr}} = 1/\alpha \simeq 137$ by solution of the Dirac equation for an electron in the Coulomb potential of a pointlike nucleus (Darwin, 1928; Gordon, 1928); it is increased to $Z_{\mathrm{cr}} \simeq 173$ by finite-size effects. Such nuclei exist only transiently, at a timescale of 10^{-23} s (Ruffini, Vereshchagin, and Xue, 2010). Nevertheless, $Z \gtrsim 80$ has proven to be sufficient for observation of Delbrück scattering (Milstein and Schumacher, 1994; Schumacher, 1999) and photon splitting (Akhmadaliev *et al.*, 2002), nonlinear QED processes that are triggered in the polarized vacuum surrounding the nucleus. Such processes could also be explored using polarized γ rays (Koga and Hayakawa, 2017) or an intense optical laser (Di Piazza, Hatsagortsyan, and Keitel, 2008; Di Piazza and Milstein, 2008).

Even stronger electromagnetic fields are generated in the collision of heavy nuclei that are moving with relativistic velocity (Gershtein and Popov, 1973; Baur, Hencken, and Trautmann, 2007; Tuchin, 2013); see also Popov (2001) and references therein. In a peripheral collision between two nuclei with the atomic number Z and the Lorentz factor γ, a characteristic electromagnetic field strength of $E \simeq cB \simeq Ze\gamma/\epsilon_0 b^2$ is sustained over a duration of $\Delta t \simeq b/\gamma c$ in the laboratory frame (the peripheral indicates that b, the impact parameter, is greater than the sum of the radii of the two nuclei). The field invariants $|\mathcal{F}|$ and $\chi_{e,\gamma}$ are much greater than unity for typical heavy-ion collider parameters; however, the short duration means that $a_0 \simeq eE\Delta t/mc^2 \simeq Z\alpha < 1$ for a typical impact parameter of a Compton length (Baur, Hencken, and Trautmann, 2007), and thus the interaction occurs in the perturbative rather than the tunneling regime; see Sec. I.A. The boosted Coulomb field of a nucleus can be treated as a flux of *quasireal* photons (Baur *et al.*, 2002), which has allowed photon-photon scattering to be observed for the first time (d'Enterria and da Silveira, 2013; Aaboud *et al.*, 2017). These photons can also create lepton pairs (Bottcher and Strayer, 1989; Şengül *et al.*, 2016). Electromagnetic processes of this kind must be separated from QCD phenomena such as quark-gluon plasma formation and chiral magnetic effects (Huang, 2016).

4. Aligned crystals

An experimental scenario in which strong electromagnetic fields of nuclear origin extend over macroscopic volumes is afforded by aligned crystals (Baier, Katkov, and Strakhovenko, 1998); see also the review by Uggerhøj (2005) and references therein. Ultrarelativistic positrons traveling through a crystal can be "channeled" along an axis of symmetry (Bøgh, Davies, and Nielsen, 1964; Lindhard, 1964), where the screened electric fields of the nuclei sum coherently to a macroscopic, continuous field of magnitude $E \simeq 10^{13}$ V m^{-1}, which is typically a few millimeters in size. This corresponds to a quantum parameter $\chi_e \simeq \mathcal{E}_0[100\ \mathrm{GeV}]$, where $\mathcal{E}_0$ is the energy of the positron. The equivalent strength parameter may be estimated as $a_0 \simeq p_\perp/mc$, where $p_\perp \simeq \mathcal{E}_0\theta/c$ and $\theta \ll 1$ is the angle between the trajectory and the crystal axis. Planar channeling occurs when $\theta < \theta_c = \sqrt{2U_0/\mathcal{E}_0}$ (for positively charged particles). Setting $\theta = \theta_c$ and taking $U_0 \simeq 50$ eV as a typical value of the crystal potential (Uggerhøj, 2005), we obtain $a_0 \lesssim 6\mathcal{E}_0^{1/2}[100\,\mathrm{GeV}]$. (The true value must be inferred.) Lepton beams with the necessary 100-GeV energies, available at the Super Proton Synchrotron at CERN, have been used to measure photon emission (Kirsebom *et al.*, 2001; Andersen *et al.*, 2012) and electron-positron pair creation (Belkacem *et al.*, 1987) in the strong-field regime. The effect of radiation reaction, the modification to the charge dynamics caused by the emission of multiple hard photons, was recently measured in the radiation emitted by channeled positrons (Wistisen *et al.*, 2018, 2019). In all these cases, the processes of interest must be distinguished from a background of single-nucleus effects, including bremsstrahlung (Uggerhøj, 2005).

5. High-intensity lasers

Laser systems create strong fields by focusing ultrashort, energetic pulses of electromagnetic radiation, exploiting the high degree of spatial coherence to reach near-diffraction-limited focal spot sizes. The electric-field strength at the focus E_0 is related to the peak intensity I_0 by $E_0 = \sqrt{2I_0/\epsilon_0 c}$ (assuming linear polarization); the strength parameter follows as

$$a_0 \simeq 0.85 I_0^{1/2}[10^{18}\ \mathrm{W\,cm^{-2}}]\lambda[\mu\mathrm{m}], \tag{10}$$

where λ is the wavelength. In terms of the power $\mathcal{P}$ per unit area A, $a_0 \simeq 270\mathcal{P}^{1/2}[\mathrm{PW}]\lambda[\mu\mathrm{m}]/A^{1/2}[\mu\mathrm{m}^2]$.

The peak powers necessary to reach the highly nonlinear regime $a_0 \gg 1$ are typically obtained by amplifying femtosecond-duration optical pulses to energies of tens or hundreds of joules. This was made possible by the invention of CPA (Strickland and Mourou, 1985), and the subsequent petawatt revolution has seen the development of high-power laser facilities across the globe (Danson *et al.*, 2019). Intensities as high as 10^{22-23} W cm^{-2} have already been reported (Yanovsky *et al.*, 2008; Sung *et al.*, 2017; Kiriyama *et al.*, 2018; Yoon *et al.*, 2021), while

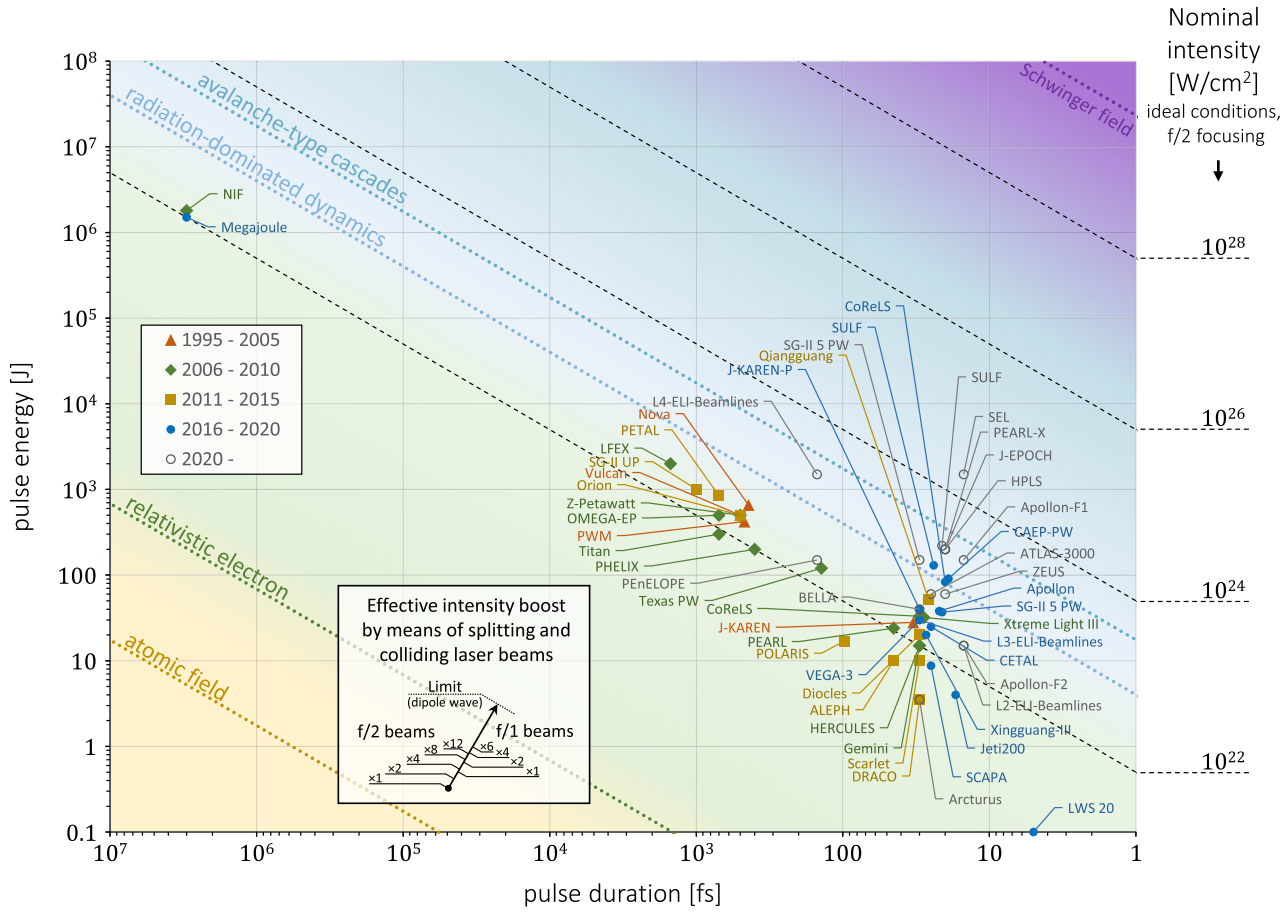

FIG. 2. Laser facilities on the map of pulse energy and pulse duration. Data were taken from National Academies of Sciences, Engineering, and Medicine (2018), Danson *et al.* (2019), and individual facilities; see Table II. For illustration, we show the nominal peak intensity levels estimated, assuming ideal $f/2$ focusing of a linearly polarized pulse with Gaussian spatial and temporal profiles and a nominal wavelength of $\lambda = 1$ μm. The physics in access is denoted by color and the following characteristic intensity scales (see Sec. I.C): 3.5×10^{16} W/cm^2 [atomic field corresponding to a field strength of 1 a.u.; see Krausz and Ivanov (2009)], 1.37×10^{18} W/cm^2 (relativistic electron corresponding to $a_0 = 1$), 8×10^{22} W/cm^2 [radiation-dominated dynamics corresponding to $L_d = \lambda$, assuming that $\gamma = a_0$; see Eq. (13)], 3.5×10^{23} W/cm^2 [avalanche-type cascades corresponding to $L_p = \lambda$, assuming that $\gamma = a_0$; see Eq. (16)], and 4.65×10^{29} W/cm^2 (corresponding to the Schwinger field strength). Inset: effective intensity boost that one would gain by splitting the laser power among the specified number of beams and colliding them so that the electric field is summed up coherently; see the Appendix of Gonoskov *et al.* (2014). The boost is shown via the corresponding relative shift of location on the map for the cases using $f/2$ (left side) and $f/1$ (right side) focusing, and the dotted line shows the ultimate boost given by the dipole wave; see Sec. V.E.3.

$10^{23\text{–}24}$ W cm^{-2} is expected in upcoming laser facilities such as Apollon (Papadopoulos *et al.*, 2016), the pillars of the Extreme Light Infrastructure (Weber *et al.*, 2017; Gales *et al.*, 2018), and the Shanghai Coherent Light Facility (Shen *et al.*, 2018). Current petawatt-scale laser facilities, and those soon to be commissioned, are shown in Fig. 2 in terms of their nominal pulse energy, duration, and date of commissioning. Note that the dashed lines do not indicate the intensity actually achieved but rather the hypothetical values estimated for ideal $f/2$ focusing. In reality, reaching high values of the Strehl ratio can be hindered by optical and chromatic abberations.

Moreover, high-power laser systems are, or are planned to be, colocated with other experimental platforms, including conventional electron accelerators (Abramowicz *et al.*, 2019; Yakimenko *et al.*, 2019a; Meuren *et al.*, 2020) and x-ray free electron lasers (Shen *et al.*, 2018). The former enabled the first demonstration of SFQED effects in a landmark experiment that measured nonlinearities in Compton scattering and electron-positron pair creation at a laser intensity of 10^{18} W cm^{-2} (Bula *et al.*, 1996; Burke *et al.*, 1997; Bamber *et al.*, 1999). However, recent developments in laser-driven wakefield acceleration (Tajima and Dawson, 1979) [see Esarey, Schroeder, and Leemans (2009) for details] have made it possible to produce multi-GeV electron beams (Kim *et al.*, 2013; Wang *et al.*, 2013; Leemans *et al.*, 2014; Gonsalves *et al.*, 2019), and therefore to perform "all-optical" laser-electron collision experiments (Bulanov *et al.*, 2011). These have been realized in the dual-pulse laser systems Diocles (S. Chen *et al.*, 2013; Yan *et al.*, 2017) and Gemini (Sarri *et al.*, 2014; Cole *et al.*, 2018; Poder *et al.*, 2018). Many of the forthcoming systems shown in Fig. 2 are multibeam facilities designed to deliver several laser pulses simultaneously to the same target chamber, which is in most

cases a requirement for a facility to be able to conduct SFQED experiments (Zhang *et al.*, 2020).

This facilitates a range of possible experimental geometries, which we discuss in Sec. IV.A. Broadly, there are three characteristic geometries in which strong-field effects are manifested (Bulanov *et al.*, 2011; Blackburn, 2020): laser–electron-beam, laser-plasma, and laser-laser geometries. In the first, the electrons are accelerated to high energy before the collision, and therefore the laser pulse acts only as the "target"; the chararacteristic quantum parameter scales as

$$\chi_e \simeq 0.18\mathcal{E}_0[\mathrm{GeV}]I_0^{1/2}[10^{21}\ \mathrm{W\,cm^{-2}}], \tag{11}$$

where $\mathcal{E}_0$ is the initial energy of the electron beam and I_0 is the laser intensity. It is also possible to use the electron beam to generate high-energy photons, which then collide with the high-intensity laser; see Sec. V.C. In the last two geometries, the laser is simultaneously the accelerator and the target (Bell and Kirk, 2008). The requirement that the laser fields be strong enough to accelerate the electrons from rest to suitably high energies means that there is a different scaling of quantum parameter with laser intensity. Assuming that the Lorentz factor $\gamma \simeq a_0$, which is a suitable estimate in both the laser-solid (Wilks *et al.*, 1992) and laser-laser cases (Zel'Dovich, 1975), we obtain

$$\chi_e \simeq 0.09I_0[10^{23}\ \mathrm{W\,cm^{-2}}]\lambda[\mu\mathrm{m}] \tag{12}$$

for an interaction driven primarily by a laser rather than an electron beam. See the discussion in Sec. IV.

C. Physical regimes

Having introduced what strong electromagnetic fields are and where they may be found, we now consider the various phenomena that they induce and how these phenomena permit classification of different physical regimes. We focus, in particular, on high-intensity lasers, as progress in their development has opened up new experimental opportunities to reach regimes where radiation-reaction and QED effects play a significant role in particle dynamics; see Sec. V. The parameter space shown in Fig. 3 is that of the classical and quantum nonlinearity parameters a_0 [Eq. (7)] and χ [Eqs. (5)

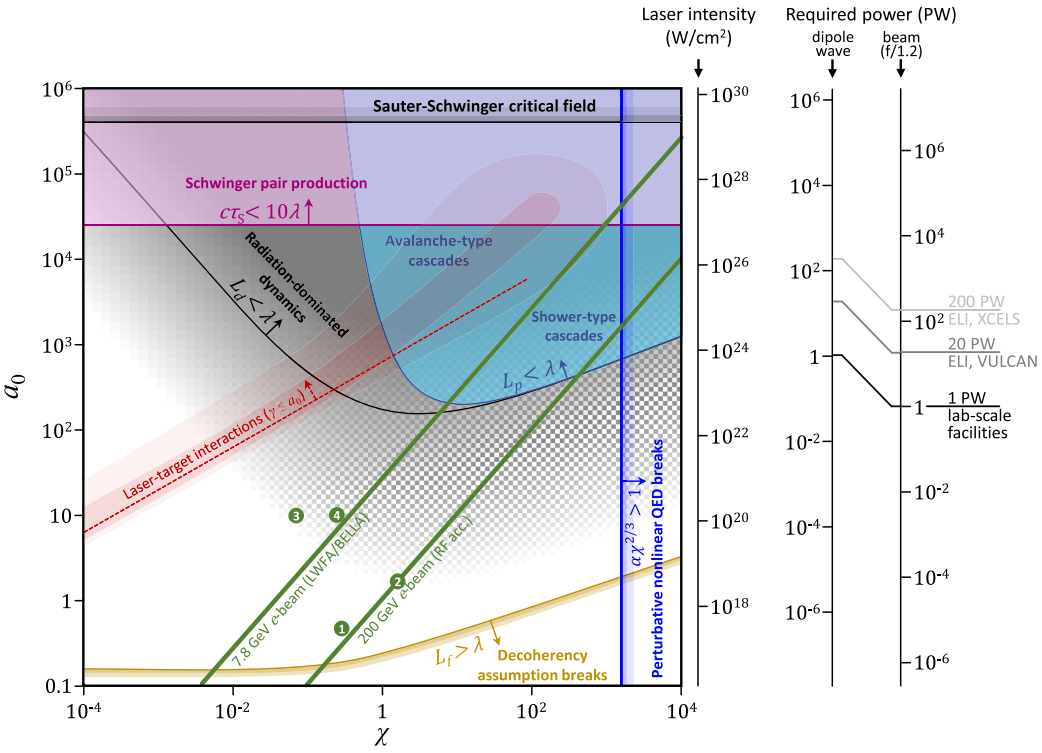

FIG. 3. Interaction regimes in the space of the normalized field amplitude a_0 and the quantum nonlinearity parameter χ. We identify the importance of different processes by comparing key space scales with a characteristic laser wavelength $\lambda = 1\ \mu$m. The decreasing depletion length L_d [Eq. (13)] denotes the transition from weak to strong radiation losses ($L_d > 10^3\lambda$ in white, $L_d < \lambda$ in dark gray). A quantization length L_q [Eq. (14)] comparable to λ indicates that the discrete nature of radiation emission is important ($L_q > \lambda$, checkered area). As the pair-creation length L_p [Eq. (16)] becomes smaller than λ, electron-positron pair creation by photons in strong fields becomes prolific ($L_p < \lambda$ in light blue). The field amplitude necessary for the onset of vacuum pair creation by the Schwinger mechanism, shown in violet, assumes a nonzero $\mathcal{F} = a_0(\hbar\omega_0/mc^2)$. Key limits on theoretical treatments are as follows: the field cannot be assumed to be constant if the formation length $L_f < \lambda$ [Eq. (15)] (yellow line), perturbation theory in SFQED is expected to break down when $\alpha\chi^{2/3} \gtrsim 1$ (blue line), and a general electromagnetic field cannot be approximated as crossed if $\chi^2 < \mathcal{F}, \mathcal{G}$. We also outline the prospects for laser experiments in interactions with a stationary plasma target ($\gamma \lesssim a_0$, red dashed line) or ultrarelativistic electron beams (green lines). Numbered green points indicate experiments that have probed the strong-field regime (in order of publication): (1) Bula *et al.* (1996) and Burke *et al.* (1997), (2) Wistisen *et al.* (2018), (3) Cole *et al.* (2018), and (4) Poder *et al.* (2018).

TABLE I. Scalings of the probability rates and their associated length scales with a_0, χ, and γ. γ refers either to a Lorentz factor for an electron or to $\hbar\omega/mc^2$ for a photon, as appropriate.

Quantity	$\chi \ll 1$	$\chi \gg 1$
Photon-emission rate ($c/\lambda\!\!\!^{-}$)	$1.44\alpha\gamma^{-1}\chi$	$1.46\alpha\gamma^{-1}\chi^{2/3}$
Radiation power ($mc^3/\lambda\!\!\!^{-}$)	$2\alpha\chi^2/3$	$0.37\alpha\chi^{2/3}$
Mean photon energy (mc^2)	$0.43\gamma\chi$	0.25γ
rms divergence angle	$1.1\gamma^{-1}$	$1.3\gamma^{-1}\chi^{1/3}$
Pair-creation rate ($c/\lambda\!\!\!^{-}$)	$0.23\alpha\gamma^{-1}\chi e^{-8/(3\chi)}$	$0.38\alpha\gamma^{-1}\chi^{2/3}$
Depletion length L_d (λ)	$33a_0^{-1}\chi^{-1}$	$55a_0^{-1}\chi^{1/3}$
Mean free path L_q (λ)	$48a_0^{-1}$	$15a_0^{-1}\chi^{1/3}$
Formation length L_f (λ)	$0.18a_0^{-1}$	$0.21a_0^{-1}\chi^{1/3}$
Pair-creation length L_p (λ)	$95a_0^{-1}e^{8/(3\chi)}$	$57a_0^{-1}\chi^{1/3}$

and (6)], which provide Lorentz-invariant proxies for the field amplitude and particle energy. The importance of a given process is quantified by comparing its characteristic length scale with the characteristic length scale of the external field, which is the laser wavelength $\lambda = 2\pi c/\omega_0$ (for frequency ω_0). As most high-power lasers operate at near-infrared or optical wavelengths (see Fig. 2), we set this to a nominal value of $\lambda = 1\ \mu$m. Scalings for the lengths introduced in this section are given in Table I.

The nature of radiative energy losses can be characterized by two length scales: one classical and the other quantum. The following depletion length L_d is the distance over which an electron, accelerated by a strong electromagnetic field, radiates away energy equal to its own kinetic energy:

$$L_d = \frac{\gamma mc^3}{\mathcal{P}_{\mathrm{rad}}}. \tag{13}$$

In Eq. (13) $\mathcal{P}_{\mathrm{rad}}$ is the radiated power [see Eq. (36)] for an electron accelerated by an electromagnetic field with normalized amplitude a_0, i.e., $\chi = \chi_e = \gamma a_0 \hbar\omega_0/mc^2$. To permit a simple interpretation of this scale length, we neglect the self-consistent reduction of $\mathcal{P}_{\mathrm{rad}}$ due to energy loss; see Sec. IV.B for self-consistent solutions.[3] $L_d < \lambda$ marks the transition to the radiation-dominated regime (Bulanov *et al.*, 2004; Koga, Esirkepov, and Bulanov, 2005; Hadad *et al.*, 2010). This is equivalently expressed as $R_c = \alpha a_0 \chi > 1$ if $\chi \ll 1$, where R_c is the classical radiation-reaction parameter (Di Piazza, 2008; Harvey *et al.*, 2011).

The quantization length gives the typical distance between the emissions of individual photons, which may be defined as the ratio of the mean energy of the photon spectrum $\langle\hbar\omega\rangle$ to the radiated power, as follows:

$$L_q = \frac{\langle\hbar\omega\rangle c}{\mathcal{P}_{\mathrm{rad}}}. \tag{14}$$

If $L_q > \lambda$, the discrete nature of the radiation emission becomes dynamically important, leading to the phenomena of stochastic broadening, straggling, and quenching; see Sec. IV.C. This is equivalently expressed as $R_q = \alpha a_0 < 1$ if $\chi \ll 1$ (Di Piazza, Hatsagortsyan, and Keitel, 2010). If $L_d \ll \lambda$ and $L_q \gtrsim \lambda$, recoils due to photon emission are infrequent but individually strong (Gonoskov *et al.*, 2015).

The shading in Fig. 3 characterizes radiation losses according to the two length scales L_d and L_q: the tone shows their strength, from weak ($L_d > 10^3\lambda$, white) to strong ($L_d < \lambda$, dark gray), while the texture indicates whether quantization effects are negligible ($L_q = 0$, uniform) or important ($L_q > \lambda$, sharply checkered).

Finally, we can define the formation length L_f as the typical distance over which a single photon is emitted. Physically, we may understand it as the distance traveled before the electron is deflected sufficiently to separate from its radiation cone (Kirk, Bell, and Arka, 2009). We have

$$L_f = \frac{c\langle\theta^2\rangle^{1/2}}{\omega_{\mathrm{eff}}}, \tag{15}$$

where $c/\omega_{\mathrm{eff}} \simeq \lambda\!\!\!^{-}\gamma^2/\chi$ is the instantaneous radius of curvature of the electron trajectory and $\langle\theta^2\rangle$ is the mean-square divergence of the emitted radiation (Baier, Katkov, and Strakhovenko, 1998); see Sec. II.B.3 for a discussion. This definition is chosen for illustrative purposes: we discuss other definitions that are available in the literature, from a classical (Jackson, 1999) or quantum perspective (Ritus, 1985; Baier, Katkov, and Strakhovenko, 1998), in Sec. II.B.3. The condition in which $L_f \ll \lambda$ is required for interference effects to be negligible, i.e., the emission of many photons may be treated as sequential and incoherent (Di Piazza, Hatsagortsyan, and Keitel, 2010). This is discussed in Sec. II.B.4.

The dominant physical process for photons propagating through a strong electromagnetic field is electron-positron pair creation via the multiphoton Breit-Wheeler process, as it appears at first order in an expansion in α. This is the generalization of the two-photon pair-creation mechanism (Breit and Wheeler, 1934) to the highly multiphoton, strong-field regime (Reiss, 1962; Nikishov and Ritus, 1964); see Sec. II.B.2. Its importance is characterized by the pair-creation length

$$L_p = cP_b^{-1}, \tag{16}$$

where P_b is the pair-creation probability rate; see Eq. (43) for a photon propagating in an electromagnetic field with a normalized amplitude a_0. The photon energy $\hbar\omega$ is defined such that $\chi_\gamma = \chi = a_0(\hbar\omega)(\hbar\omega_0)/(mc^2)^2$. If $L_p \gg \lambda$, the photon is likely to escape the strong-field region.

The Schwinger mechanism for pair creation, in contrast to the multiphoton Breit-Wheeler process, is driven by the field itself. However, as stated in Sec. I.A, a crossed field such as a plane electromagnetic wave cannot produce pairs via this mechanism, regardless of its amplitude a_0. Noncrossed fields, created by the superposition of multiple noncopropagating plane waves, can. In Fig. 3 the uppermost horizontal black line, with shading on one side, denotes the a_0 value that is equivalent to the critical field strength, assuming that we have

[3]Accounting for the self-consistent energy loss in the classical regime $\chi_e \ll 1$ and assuming that $\gamma \gg a_0$, L_d is the distance traveled before the electron loses half of its initial energy.

N counterpropagating laser beams, each with a normalized amplitude a_0/N and a frequency ω_0 equivalent to 1 μm, i.e., $\mathcal{F} = a_0(\hbar\omega_0/mc^2) = 1$ from Eq. (3). It is worth noting that the Schwinger pair-creation rate yields, on average, one pair within a spacetime volume of $10\lambda^4/c$, which is equivalent to multiple 10-cycle laser pulses focused into a λ^3 volume, for a significantly lower field strength $a_0 \simeq 2.5 \times 10^4$ (Narozhny *et al.*, 2004b; Bulanov *et al.*, 2006); this is shown as the magenta line in Fig. 3.

Also outlined in Fig. 3 is the region where $\alpha\chi^{2/3} > 1$, where the perturbative treatment of nonlinear QED is predicted to break down (Narozhny, 1980; Ritus, 1985). A theory that is applicable in this regime is yet to be developed; see Sec. VII.A.

The green and red lines show the expected capability of laser-based experiments to reach large values of χ, either by colliding a beam of ultrarelativistic electrons (energy given next to the line) with a laser pulse of peak amplitude a_0 (green lines) or by direct irradiation of a plasma target (red lines), which accelerates electrons to energies of the order of $\gamma \sim a_0$ (Wilks *et al.*, 1992). The green labels numbered (1), (3), and (4) correspond to experiments performed in the colliding beam geometry. Label (2) indicates the equivalent χ and a_0 for a recent crystal-based experiment; see Sec. I.B.4.

The scales on the right-hand side of Fig. 3 indicate the total laser power necessary to reach a given a_0, either by focusing a single laser beam or by creating a dipole wave with multiple colliding beams (Bulanov, Mur *et al.*, 2010; Gonoskov *et al.*, 2013). The latter is the theoretical limit on the a_0 achievable at a given power (Bassett, 1986; Gonoskov *et al.*, 2012). The scalings of the quantities discussed in this section are collected in Table I for convenience. Full expressions for the rates are given in Sec. II.B.2.

Figure 3 is plotted while assuming a laser wavelength of 1 μm, which is most relevant for present-day laser technology. Although it would increase experimental difficulties (see Sec. V.E.1), changing the wavelength would open up new avenues for the exploration of strong-field effects. Esirkepov *et al.* (2015), Bulanov *et al.* (2017), Jeong *et al.* (2020), and Zhang *et al.* (2020) noticed that the wavelength plays an important role in determining what interaction regimes are accessible with a given radiation power. These are shown in Fig. 4 for varying wavelengths λ and amplitudes a_0. Here we assume that the electron energy is determined by the laser amplitude, $\gamma = a_0$, as would approximately be the case in a laser-laser or laser-plasma interaction. While the wavelength is not Lorentz invariant, its value in the laboratory frame is nevertheless useful, as the laboratory frame coincides with the average rest frame in the case of a standing-wave interaction. Optical or near-infrared lasers provide opportunities to explore radiation reaction (RR) in both its quasicontinuous and discrete forms, whereas for larger (smaller) wavelengths, RR has a more continuous (discrete) form.

Ultrashort-wavelength lasers have the advantage of reaching the quantum regime ($\chi = 1$) more easily because of reduced radiation losses. Note that the region $L_d < \lambda$ is reached at a higher a_0 the more the wavelength is reduced. While a technology able to produce short wavelength lasers with required power is not yet developed, there are proposals

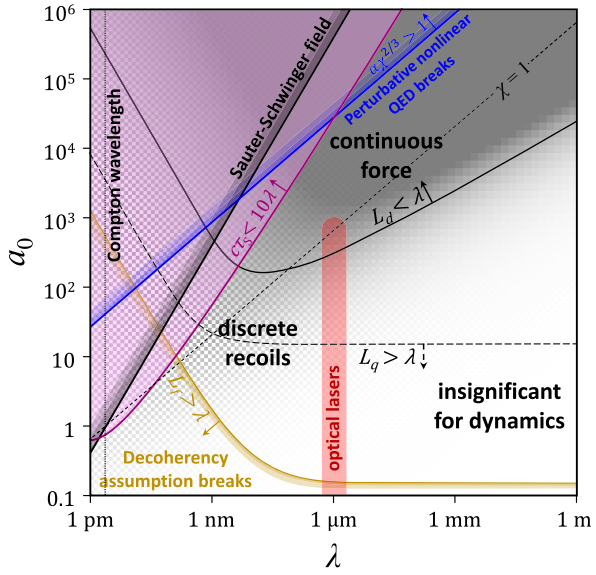

FIG. 4. Interaction regimes as a function of the amplitude a_0 and the wavelength λ of the electromagnetic wave driving an electron, using the same key as in Fig. 3. The importance of RR effects is parametrized by L_d [Eq. (13)] and L_q [Eq. (14)], which are both wavelength dependent.

to use relativistic flying mirrors (Bulanov, Esirkepov, Kando, Pirozhkov, and Rosanov, 2013) and high-harmonic generation (Bulanov, Naumova, and Pegoraro, 1994; Gordienko *et al.*, 2005) to create high-frequency EM pulses with ultrahigh intensity; see Sec. VII.B. On the other hand, the overlap between the radiation-dominated and quantum-dominated regimes are reached almost simultaneously if $\lambda \simeq 1$ μm, at an a_0 achievable with 10 PW of laser power. Thus, current optical or near-infrared lasers are well placed to access a regime where relativistic plasma dynamics is strongly affected by both radiation and quantum effects.

D. Overview and scope of this review

No review can be absolutely comprehensive, as the boundaries between fields of study are not themselves absolute. Here we limit ourselves to a region of parameter space where the most significant interaction is between particles and EM fields. We do not consider the direct interaction of EM fields with themselves, which encompasses vacuum modification or decay, and point the interested reader to the reviews by Marklund and Shukla (2006), Mourou, Tajima, and Bulanov (2006), Ehlotzky, Krajewska, and Kamiński (2009), Di Piazza *et al.* (2012), and King and Heinzl (2016). We focus on SFQED effects that can be experimentally studied at existing or next-generation high-power laser facilities. As such, the scope of this review article is the interaction of electrons, positrons, and photons with strong electromagnetic fields, emergent phenomena that arise from this interaction, possible routes toward experimental investigation, and applications thereof.

To facilitate this program, we organize the review in the following way. We begin with an overview of fundamental physics concepts of SFQED. In Sec. II, the essential elements

of the classical and quantum descriptions of charged particle interactions with strong fields are given. First, the development of classical radiation reaction is reviewed, with particular emphasis on the Lorentz-Abraham-Dirac and Landau-Lifshitz equations, and the limits of classical theory are given. Second, we discuss the multiphoton Compton and Breit-Wheeler processes, which are the basic building blocks of SFQED, the approximations customarily used to study these effects, radiative corrections, higher-order processes, and phenomenological aspects.

In Sec. III we discuss the state-of-the-art numerical methods used to simulate these interactions, including practical aspects of how the computational demand of multiscale simulations can be controlled.

Charged particle dynamics, i.e., emergent phenomena that are consequences of the fundamental processes described in Sec. II, is covered in Sec. IV. First discussed are the typical interaction setups, which correspond to different types of charged particle dynamics in strong fields. We show how the increase in field strength and particle energy leads to a nontrivial evolution of the particle dynamics, from well-characterized classical trajectories to trapping in different configurations of EM fields, and from chaotic motion to strange attractors and limit cycles. Here we encounter *cascades*, one of the most fascinating processes of SFQED, where a few initial particles are transformed into many, high-energy photons, and electron-positron pairs via iterated multiphoton Compton and Breit-Wheeler processes. These cascades can be so intense that they can change the properties of the strong field itself.

Although such particle dynamics requires laser intensities that are not yet available, existing facilities have been able to conduct groundbreaking experiments on the topic. We review them in Sec. V, beginning with those that were carried out at conventional accelerator facilities, where the laser was used only as a target for high-energy electron beams, and progressing to all-optical setups, where electrons were accelerated by laser-plasma interactions and then collided with laser pulses. We also discuss possible future directions, including the generation and diagnosis of ultrastrong fields. The study of particle dynamics in strong EM fields opens up possibilities for the generation of various particle and radiation sources, which are discussed in Sec. VI.

In the course of this review, we repeatedly stress that there are many unanswered questions and yet-to-be-studied phenomena in SFQED. We summarize them in Sec. VII.A, along with a description of possible future experimental programs. We conclude in Sec. VIII. At the end of the review we provide a List of Symbols and Abbreviations.

II. THEORY OF STRONG ELECTROMAGNETIC FIELDS

A. Classical radiation reaction

1. The problem of radiation reaction

We begin with a historical perspective on the problem of accounting for the recoil from the electromagnetic radiation emitted by an accelerated charge, a puzzle that has engaged the community for over a century. More in-depth discussions were given by Caldirola (1979), Klepikov (1985), Weinberg (1995), and Rohrlich (2007). In a picture of electrodynamics where matter is treated as a continuous fluid, recoil due to radiation emission is self-consistently embedded in the Vlasov-Maxwell system (Vlasov, 1938), which implies the existence of a continuity equation for both energy and momentum. However, the discovery of the electron by Thompson in 1897 raised conceptual difficulties because the electromagnetic field energy of a point charge diverges (Pryce, 1938).

An early attempt to resolve these difficulties was made by Lorentz (1892, 1904), who modeled the electron as a sphere of small but finite radius r such that the entirety of the electron mass could be attributed to its electromagnetic energy $e^2/6\pi\epsilon_0 c^2 r$. Under acceleration, an imbalance between the electromagnetic forces exerted between different parts of the sphere leads to an additional force $\propto d^3\mathbf{x}/dt^3$, where $\mathbf{x}$ is the position of the charge center. The magnitude of this force is consistent with the momentum loss due to radiation emission, as described by the nonrelativistic Larmor formula (Larmor, 1897). A relativistic force using the relativistic formulation of the radiated power (Heaviside, 1902) was presented by Abraham (1902).

Left unresolved, however, was the question of what held the charge together. A perfectly rigid sphere would not be consistent with relativity, whereas deformation of the sphere would indicate internal degrees of freedom of unknown origin. This motivated Dirac to revisit the problem. He derived a relativistic equation of motion by enforcing energy-momentum conservation of the electromagnetic flux through a small surface surrounding a charge of still unknown structure (Dirac, 1938). No higher-order terms (in the radius of the charge r) need to be omitted. The equation of motion, referred to as the Lorentz-Abraham-Dirac (LAD) equation, is given by (Dirac, 1938)

$$\frac{dp^\mu}{d\tau} = -\frac{eF^{\mu\nu}p_\nu}{mc} + g^\mu, \tag{17}$$

$$g^\mu_{\mathrm{LAD}} = \tau_{\mathrm{rad}}\left[\frac{d^2p^\mu}{d\tau^2} + \frac{p^\mu}{(mc)^2}\frac{dp^\nu}{d\tau}\frac{dp_\nu}{d\tau}\right], \tag{18}$$

where $\tau_{\mathrm{rad}} = 2\alpha\lambda\!\!\!^{-}/3c = 2r_e/3c$ and τ is the proper time. The second term g^μ is the additional four force that arises from radiation reaction. An interesting consequence is that the observed mass of the electron, i.e., the scaling factor m between the velocity $dx^\mu/d\tau$ and the momentum $p^\mu = m(dx^\mu/d\tau)$, is the difference between a divergent quantity, electromagnetic in origin, and a "bare" mass; this predates the renormalization later applied in quantum field theory. The LAD model is not completely self-consistent, which is manifested by pathological solutions that describe self-accelerating (runaway) charges; see Spohn (2000) and Burton and Noble (2014). These solutions can be eliminated by imposing a boundary condition of zero acceleration in the distant future (Dirac, 1938). However, the pathological behavior can be restarted and then terminated through hard collisions (Eliezer, 1943). Another approach is to reduce the order of the equation, which we discuss in Sec. II.A.2. Other classical theories of radiation reaction were proposed by Eliezer (1948), Mo and Papas (1971), Bonnor (1974),

Herrera (1977), Caldirola (1979), Ford and O'Connell (1991), and Sokolov (2009); see the review by Burton and Noble (2014).

Distinguishing between these models is perhaps best accomplished by appealing to a more fundamental theory of electrodynamics. The development of quantum theory led to a paradigm shift in how the "localization" of the charge of an electron could be understood. Furthermore, in a scattering matrix approach conservation of momentum applies directly to the in-state and out-state, which can contain arbitrary numbers of additional particles, including photons. The quantum formalism established a broader framework that now accompanies discussions of radiation reaction and its implications in strong-field environments (Ruffini, Vereshchagin, and Xue, 2010; Di Piazza *et al.*, 2012). We discuss the limits of the classical theory in Sec. II.A.3 and radiation reaction, as the classical limit of a QED result, in Sec. II.C.

2. From Lorentz-Abraham-Dirac to Landau-Lifshitz equations

The pathological behavior in solutions of the Lorentz-Abraham-Dirac equation (18) is driven by the second derivative of the momentum. Note that these pathological solutions arise because of the specific form of the second derivative, not its mere presence (Burton and Noble, 2014). The "critical surface," which is the manifold of physical solutions to the LAD equation, is repulsive: small deviations from it grow and the solutions run away to infinity (Spohn, 2000). These runaways can be prevented by requiring the acceleration to vanish in the asymptotic future (Dirac, 1938), which provides the necessary third boundary condition after the initial position $x^\mu(0)$ and momentum $p^\mu(0)$; however, the question of the solution's uniqueness follows (Spohn, 2000). Moreover, eliminating the runaways in this fashion leads to the problem of "preacceleration," where the charge moves in advance of the applied force (Klepikov, 1985; Rohrlich, 2007).

Landau and Lifshitz proposed eliminating the second derivative through a reduction of order process, expanding Eq. (18) in the small parameter $\tau_{\rm rad}$ (Landau and Lifshitz, 1987). This requires radiation reaction to be weak compared to the Lorentz force in the instantaneous rest frame of the charge (Eliezer, 1948). At lowest order, this has the effect of replacing $dp_\mu/d\tau \to eF_{\mu\nu}p^\nu/mc$ in Eq. (18), yielding the following radiation-reaction force in the Landau-Lifshitz (LL) prescription:

$$g^\mu_{\rm LL} = \frac{\tau_{\rm rad}}{(\lambda\!\!\!^{-}/c)^2}\left[-\frac{(\partial_\sigma F^{\mu\nu})p_\nu p^\sigma}{mcE_{\rm cr}/\lambda\!\!\!^{-}} + \frac{F^{\mu\nu}F_{\nu\sigma}p^\sigma}{E_{\rm cr}^2} - \chi_e^2 p^\mu\right]. \tag{19}$$

In Eq. (19) we anticipate Sec. II.A.3 by expressing the result in terms of quantum parameters such as $E_{\rm cr}$ and χ_e; nevertheless, all factors of $\hbar$ cancel as required. We see that Eq. (19) is first order in the momentum, and therefore that only two boundary conditions, the initial position $x^\mu(0)$ and the momentum $p^\mu(0)$, are required to solve it. Spohn (2000) argued that solutions to the Landau-Lifshitz equation lie on the same manifold as physical solutions of the LAD equation. Moreover, for a given $x^\mu(0)$ and $p^\mu(0)$, there is exactly one solution on the critical surface, which also satisfies the asymptotic boundary condition $\lim_{\tau\to\infty} dp^\mu/d\tau \to 0$ (Spohn, 2000). Investigations of higher-order approximations to the LAD equation in the nonrelativistic (Zhang, 2013) and relativistic cases (Ekman, Heinzl, and Ilderton, 2021b) show that the effect of RR is to drive the particle toward the regime where the LL equation is valid. More details concerning the relation between the LAD and Landau-Lifshitz equations are given in the reviews by Di Piazza *et al.* (2012) (Sec. VI) and Burton and Noble (2014).

Implementations of classical radiation reaction in plasma simulation codes have focused almost exclusively on the Landau-Lifshitz equation, which we discuss in Sec. III. It is possible to solve the Landau-Lifshitz equation analytically for the trajectory of a charge in a plane EM wave (Heintzmann and Grewing, 1972; Di Piazza, 2008; Hadad *et al.*, 2010; Harvey *et al.*, 2011), as well as to obtain analytical results for aspects of its radiation spectrum (Di Piazza, 2018). The light-front momentum $p^- \equiv \kappa\cdot p/\kappa^0$ (here κ^μ is the wave vector) is not conserved under radiation reaction (Harvey *et al.*, 2011). [This is true in general, but Harvey *et al.* (2011) worked only to first order in $\tau_{\rm rad}$, reflecting the fact the Landau-Lifshitz equation is an expansion in that parameter.] Thus, a charge can gain or lose energy in a plane EM wave, in violation of the Lawson-Woodward theorem (Lawson, 1979). Note that continuing the expansion of Eq. (18) to all orders in $\tau_{\rm rad}$ and resuming the resulting divergent series recover the problematic solutions of the LAD equation (Zhang, 2013).

Differences between the predictions of the LAD and Landau-Lifshitz equations are small if the external electromagnetic field's wavelength λ and magnitude E_0 satisfy $\lambda \gg r_e$ and $E_0 \ll E_{\rm cr}^{\rm clas} = E_{\rm cr}/\alpha$ in the particle's rest frame (Landau and Lifshitz, 1987). Note that the restriction on wavelength is a restriction on the timescale of variation of the field. If the Landau-Lifshitz equation is used in a situation where there are abrupt jumps in the electromagnetic field strength, errors in energy and momentum conservation follow (Baylis and Huschilt, 2002); see Shi (2019) for a discussion of signatures in a proposed experiment.

Furthermore, the Landau-Lifshitz and Ford-O'Connell equations (Ford and O'Connell, 1991) were compared for the collision of an ultrarelativistic electron and a pulsed plane EM wave by Kravets, Noble, and Jaroszynski (2013), where it was shown that energy losses due to radiation reaction prevent the electron from entering the regime where the two equations predict significantly different behavior.

Radiative energy losses are why the threshold for quantum effects is reached long before the breakdown of the Landau-Lifshitz equation. Consider the steady-state energy of an electron, orbiting in a rotating electric field that has an amplitude a_0 and an angular frequency ω_0 (a model for fields at the magnetic node of a circularly polarized standing wave). Differences between the LAD and Landau-Lifshitz equations become visible at $\varepsilon_{\rm rad}a_0 \simeq 0.1$, where $\varepsilon_{\rm rad} = (2\alpha/3)\hbar\omega_0/mc^2$; see Fig. 5, which was adapted from Bulanov, Esirkepov *et al.* (2011). However, the quantum parameter χ_e is already unity when $\varepsilon_{\rm rad}a_0 = (2\alpha/3)^2 \ll 0.1$, and a QED-critical field strength is reached at $\varepsilon_{\rm rad}a_0 = 2\alpha/3 < 0.1$. Indeed, considering the interaction of an electron with a plane EM wave (normalized amplitude a_0) reveals that the terms neglected

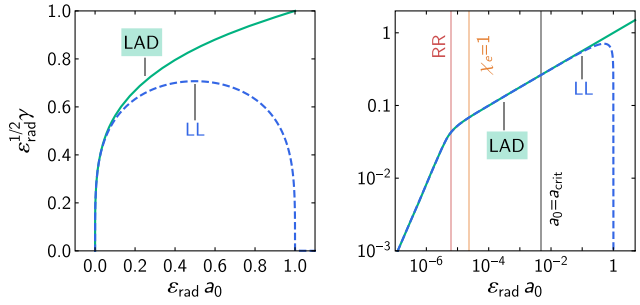

FIG. 5. The Lorentz factor γ of an electron in a rotating electric field of normalized amplitude a_0, as predicted by the LAD and Landau-Lifshitz equations, Eqs. (18) and (19), respectively: linear (left panel) and log scaled (right panel). The vertical lines indicate, from left to right, onset of classical radiation-reaction effects, Eq. (73) (red line); a quantum parameter of unity, Eq. (74) (orange line); and the QED-critical field strength, Eq. (1) (black line). Here $\varepsilon_{rad} = 1.47 \times 10^{-8}$, which is equivalent to a wavelength of 0.8 μm. Adapted from Bulanov, Esirkepov *et al.*, 2011.

in the Landau-Lifshitz equation are of the order of $\alpha\chi_e$ or $\alpha\chi_e/a_0$, which are subleading with respect to quantum corrections (Di Piazza, 2018). This makes it essential to consider radiation reaction from a quantum perspective. We conclude that the LAD and LL equations are indistinguishable in the parameter space where a classical description of RR is valid.

3. Limits of the classical theory

The failure of the classical theory of radiation reaction is evident in the fact that the characteristic timescale τ_{rad} appearing in the LAD equation is smaller than the Compton time $\lambda\!\!\!^{-}/c$ by a factor of the fine-structure constant α (Burton and Noble, 2014). Thus, insight from quantum electrodynamics plays an essential role in the investigation of the classical theory (Di Piazza *et al.*, 2012). We discuss the QED approach to particle dynamics and radiation in Sec. II.B. We first distinguish between two different possible quantum effects from the classical perspective.

For an ultrarelativistic particle (Lorentz factor $\gamma \gg 1$) in a magnetic field (strength $B < B_{cr}$), there are two types of quantum effects (Baier and Katkov, 1968). The first is associated with the noncommutation of the particle's dynamical variables and is of the order of $\hbar\omega_0/\gamma mc^2 \simeq B/\gamma^2 B_{cr} \ll 1$, where ω_0 is the cyclotron frequency; thus, the particle motion becomes more "classical" as its energy γ increases. The second effect is associated with recoil and is of the order of $\hbar\omega_c/\gamma mc^2 \simeq \gamma B/B_{cr} \gtrsim 1$, where $\omega_c \propto \gamma^3\omega_0$ is the typical frequency of the emitted radiation (Schwinger, 1949). Thus, in many scenarios of interest one need take into account only the commutators of the particle's dynamical variables and the field of the emitted photon (Baier and Katkov, 1968). We may therefore discuss quantum effects principally in terms of their effect on the spectrum of radiation emitted by an accelerating charge.

Consider the electric and magnetic fields arising from a charge in arbitrary motion, with its trajectory defined by a position $\mathbf{r}(t)$ and velocity $\boldsymbol{\beta}(t)$, which were derived by Liénard (1898) and Wiechert (1900). The following Fourier analysis yields the energy radiated per unit photon energy $\hbar\omega$ in the far field (Jackson, 1999):

$$\frac{d\mathcal{E}}{d\hbar\omega} = \frac{\alpha\omega^2}{4\pi^2}\int d\Omega \left| \int dt\, \mathbf{n}\times(\mathbf{n}\times\boldsymbol{\beta}) e^{i\omega(t-\mathbf{n}\cdot\mathbf{r}/c)} \right|^2, \tag{20}$$

where $\mathbf{n}$ is the observation direction and the integral is taken over all times t and solid angles Ω. The energy radiated, as predicted using Eq. (20), is consistent with the energy loss predicted using Eq. (19) (Schlegel and Tikhonchuk, 2012; Thomas *et al.*, 2012; Martins *et al.*, 2016). Simplification is possible if the interference between emission from different parts of the trajectory is negligible (Esarey, Ride, and Sprangle, 1993). The energy spectrum may then be expressed as follows as the integral of the instantaneous spectral emission rate $dW/d\hbar\omega$ over the particle trajectory, assuming that, at high γ, the radiation is emitted predominantly in a direction parallel to the electron's instantaneous velocity (Sokolov and Ternov, 1968; Baier, Katkov, and Strakhovenko, 1998):

$$\frac{d\mathcal{E}}{d\hbar\omega} \simeq \int \hbar\omega \frac{dW}{d\hbar\omega} dt, \tag{21}$$

$$\frac{dW}{d\hbar\omega} = \frac{\alpha}{\sqrt{3}\pi\hbar\gamma^2}\int_\xi^\infty K_{5/3}(y)dy, \qquad \xi = \frac{2\hbar\omega}{3\chi_e\gamma mc^2} = \frac{\omega}{\omega_c}, \tag{22}$$

where K_ν is a modified Bessel function of the order of ν. The ξ parameter is the ratio of ω to a critical frequency ω_c, which we wrote in terms of χ_e to emphasize that it depends on the charge's instantaneous proper acceleration; see Sec. I.A. With $\chi_e = \gamma B/B_{cr}$, we obtain $\omega_c = 3\gamma^3\omega_0/2$, where the cyclotron frequency $\omega_0 = eB/\gamma m$. The radiation spectrum from an ensemble of electrons can be obtained by summing Eq. (21) over the ensemble (Reville and Kirk, 2010; Wallin, Gonoskov, and Marklund, 2015).

Equation (22) predicts that half the power radiated is radiated to frequencies that satisfy $\xi > 1$ (the spectrum peaks at $\xi \simeq 0.29$). However, this means that for $\chi_e \gtrsim 1$ the majority of the radiation is carried by photons with more energy, individually, than the electron itself; see Fig. 6. Preventing this makes quantum corrections, i.e., introducing $\hbar$, essential. First-order quantum effects are manifested by substituting $\omega \to \omega(1 + \hbar\omega/\gamma mc^2)$ into the definition of ξ (Schwinger, 1954), which reduces the total radiated power by the factor $1 - 55\sqrt{3}\chi_e/16$ (Sokolov, Klepikov, and Ternov, 1953; Schwinger, 1954). This is a pure recoil effect: spin effects first appear at second order in $\hbar$. We discuss them in Sec. II.D. To guarantee that the spectrum is cut off at $\hbar\omega = \gamma mc^2$, it suffices to make the heuristic substitution $\xi \to \xi_q$ (Lindhard, 1991),

$$\xi_q = \frac{2f_c}{3\chi_e(1-f_c)}, \qquad f_c = \frac{\hbar\omega}{\gamma mc^2}, \tag{23}$$

where f_c is the fraction of the electron energy transferred to the photon. Equation (22) with Eq. (23) is exactly the radiation spectrum of a spin-zero electron in QED (Baier and Katkov,

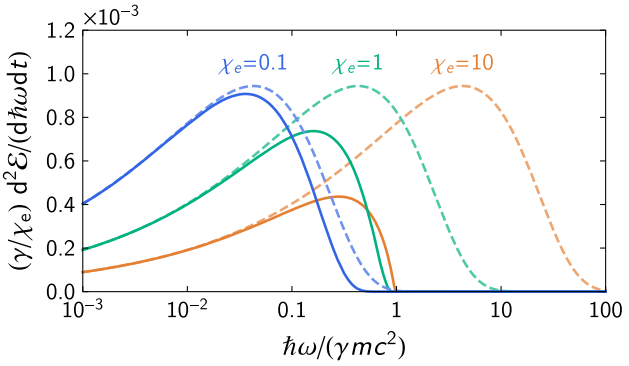

FIG. 6. Radiation at unphysically large frequencies is predicted by classical theory if $\chi_e \gtrsim 1$: classical power spectra (dashed lines) and quantum-corrected power spectra (solid lines) at $\chi_e = 0.1$ (blue lines, left), 1 (green lines, center), and 10 (orange lines, right), using Eqs. (22) and (23), respectively.

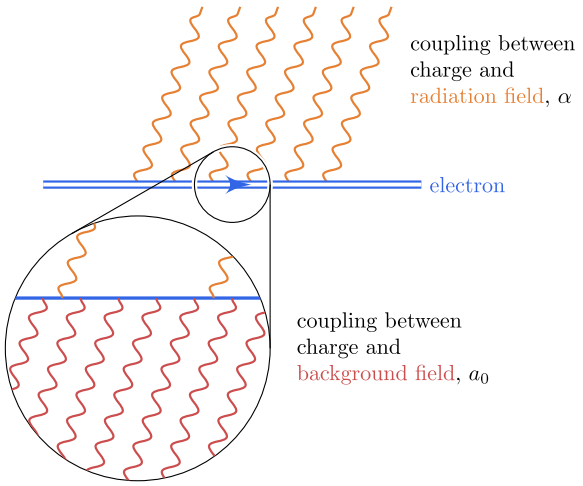

FIG. 7. Nonperturbativity in strong-field quantum electrodynamics arises in two ways: from the coupling between the charge and the background (external) field (lower set of wavy lines, in red) and the coupling between the charge and the radiation (quantized) field (upper set of wavy lines, in orange). For $a_0 > 1$, the former interaction must be taken into account exactly, i.e., to all orders in a_0, as indicated by the double fermion lines in a diagrammatic representation. For fields with a sufficient magnitude or duration, higher-order contributions to the coupling with the radiation field can dominate lower-order terms.

1968). The classical result and Schwinger's correction are reproduced at zeroth and first order in $\hbar$.

Figure 6 shows that introducing this cutoff significantly reduces the radiated power for $\chi_e \gtrsim 1$; momentum conservation requires that the magnitude of the radiation-reaction force is reduced in tandem. As such, if χ_e is not too large, the Landau-Lifshitz equation can be corrected phenomenologically by scaling g^{μ}_{LL} by the same factor by which the radiation power is reduced; see Sec. II.C. However, if the emission of even a single photon can significantly affect the electron dynamics, it is clear that radiation reaction in the quantum regime is fundamentally of a different character than its classical counterpart. Moreover, as the photons emitted by electrons with $\chi_e \gtrsim 1$ can satisfy $\chi_\gamma \gtrsim 1$, consideration must be given to the possibility of electron-positron pair creation (Reiss, 1962; Nikishov and Ritus, 1964), a process without a classical analog. Thus, we must turn to quantum electrodynamics, an inherently many-particle theory.

B. Strong-field quantum electrodynamics

1. Overview

Strong-field quantum electrodynamics has the distinct property that the electromagnetic field, with which charged particles interact, is split into two: a fixed, classical background (an external field) and a fluctuating, quantized component; see Fig. 7. The interaction with the former is treated exactly in the Furry picture of QED (Furry, 1951), which permits the interaction to be arbitrarily strong; the coupling to the quantized, radiation field is treated perturbatively. For an electromagnetic wave, where the coupling to the background field is controlled by the parameter a_0, this means that theoretical calculations are not restricted to the perturbative regime $a_0 \ll 1$. This is essential because the characteristic number of photons n absorbed when an electron emits a single high-energy photon $n \sim a_0^3$ becomes large if $a_0 > 1$; see Sec. I.A. SFQED is therefore nonperturbative in the sense that results are correct to all orders in the expansion parameter a_0. The exact treatment of the background field means that the interaction occurs with the entire electromagnetic field, rather than with individual photons thereof. As such, predictions are sensitive to the spatiotemporal structure of the field, such as pulse shape and duration. This was first studied within SFQED for photon emission by Boca and Florescu (2009), Mackenroth, Di Piazza, and Keitel (2010), and Seipt and Kämpfer (2011), and for pair creation by Heinzl, Ilderton, and Marklund (2010).

The dynamics of free electrons or positrons in QED is described via the Dirac equation, which takes the form of $[\gamma^\mu(p_\mu - eA_\mu) - mc]\psi = 0$ in the presence of an external EM field with the potential A_μ. If this EM field is a plane wave with wave vector κ_μ, where $\kappa^2 = 0$, then the Dirac equation can be solved analytically. We note that the EM field of a plane wave depends on the coordinates only through the phase $\varphi = \kappa x$, so the four-potential is also a function of φ only $[A_\mu = A_\mu(\varphi)]$. The solution of the Dirac equation in such a background is called a *Volkov state* (Wolkow, 1935):

$$\psi_{pr}(x) = \left[1 + \frac{e\not{\kappa}\not{A}(\varphi)}{2(kp)}\right] \exp\left[-\frac{iS(\varphi)}{\hbar}\right] u_{pr},$$
$$S(\varphi) = px + \int_{-\infty}^{\varphi} d\varphi' \frac{2e(pA)(\varphi') - e^2A^2(\varphi')}{2(kp)}, \qquad (24)$$

where u_{pr} is the free spinor, normalized to $\bar{u}_{pr}u_{pr'} = 2m\delta_{rr'}$, and the slashes indicate a contraction with the Dirac matrices γ^μ, i.e., $\not{X} = \gamma^\mu X_\mu$. Note that the argument of the exponent in Eq. (24) coincides with the classical action S for a particle with asymptotic momentum p moving in the EM field of a plane wave multiplied by the imaginary unit. These states have a phase-dependent momentum that corresponds closely to the classical kinetic momentum, as can be seen in Fig. 8, where

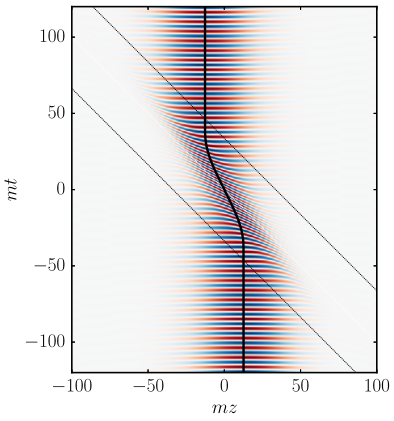

FIG. 8. Evolution of a Volkov wave packet (in a time t and a coordinate z) in a laser pulse with a normalized amplitude $a_0 = 2$ and duration $\Delta\phi = 20$ (color or gray scale density indicates the wave function). The wave packet begins with a Gaussian distribution of light-front momentum (mean mc and standard deviation $0.05mc$) and zero transverse momentum. The centroid closely follows the equivalent classical trajectory, which is indicated as a solid black line. The laser pulse propagates between the two dashed lines. From Seipt, 2017.

the motion of the centroid of a Volkov wave packet is compared to the classical trajectory (Seipt, 2017).

In the Feynman rules of SFQED, Volkov states are used to describe external electrons; see Mitter (1975) and the tutorial by Seipt (2017). This is indicated by double fermion lines in a Feynman diagram; see Fig. 7. The scattering matrix elements for processes of interest are then constructed from the standard diagrammatic representation. In Sec. II.B.2, we illustrate them for the tree-level, i.e., lowest-order, processes shown in Fig. 9: multiphoton Compton scattering and Breit-Wheeler electron-positron pair creation. It is not always guaranteed that the tree-level processes dominate: nonperturbativity can also arise in the coupling to the radiation field if the field is sufficiently strong (such as when $\chi_e > 1$) or long in duration. In these cases, the usual hierarchy, that the probability to emit N photons is larger than the probability to emit $N + 1$, can be reversed. The importance of high-order processes and the link to radiation reaction are discussed in Secs. II.B.6 and II.C, respectively. The Volkov solution assumes that the EM wave propagates in vacuum, but it is possible to account for the presence of a background plasma using similar means (Raicher and Eliezer, 2013; Mackenroth *et al.*, 2019).

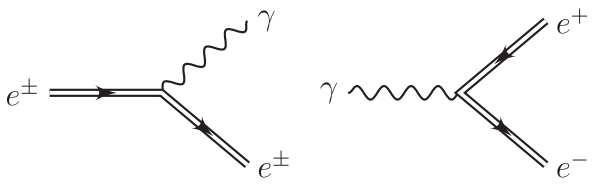

FIG. 9. Feynman diagrams of the Compton ($e \to e\gamma$) and Breit-Wheeler ($\gamma \to ee$) processes. Double fermion lines indicate that the process occurs in an external field.

2. Multiphoton Compton and Breit-Wheeler processes

To calculate the probability of the multiphoton Compton and Breit-Wheeler processes, which are $e(p) \to e(p')\gamma(k')$ and $\gamma(k) \to e(p')e(q')$, respectively (see Fig. 9), Volkov states are used as in-states and out-states for electrons and positrons in the matrix elements. Here p, q, and k are momenta of the initial electron, positron, and photon, respectively, and primed momenta refer to the same particle but in the final state. In what follows we discuss the Compton process, but since the analytical structure of the matrix element for the Breit-Wheeler process is similar, these results can be translated to the Breit-Wheeler process too. The matrix element for the Compton process is

$$M = -ie \int d^4x \bar{\psi}_{p'r'}(x)(\gamma^\mu \epsilon'_\mu) e^{ik'x} \psi_{pr}(x). \tag{25}$$

Having integrated Eq. (25) over light-front variables $x^\perp$ and x^-, we obtain

$$M = -ie(2\pi)^4 \int \frac{ds}{2\pi} \delta^{(4)}(p' + k' - p - sk) \mathcal{M}(s), \tag{26}$$

$$\mathcal{M}(s) = \mathcal{A}_0 \mathcal{I}_{(s)} + \mathcal{A}_+ \mathcal{I}_+(s) + \mathcal{A}_- \mathcal{I}_-(s) + \mathcal{A}_2 \mathcal{I}_2(s), \tag{27}$$

where $\mathcal{A}_{0,\pm,2}$ are Dirac current structures and $\mathcal{I}_{0,\pm,2}$ are integrals over the plane-wave field phase determining the amplitude of the process; see Seipt and Kämpfer (2013) for details. The variable s enters from the four-momentum conservation $p + sk = p' + k'$ and can be defined as the amount of four-momentum absorbed from the background field ($s = pk'/p'k$). Note that this is sometimes referred to as the total number of background-field photons absorbed. However, this is valid only in the case of an infinitely long plane-wave field, when the periodicity of the background field means that s must be integral; thus, discrete Fourier components may be interpreted as "photons" with momentum k_μ. The frequency of the emitted photon can be determined as follows from energy and momentum conservation:

$$\omega' = \frac{s(pk)}{(p + sk)n'}. \tag{28}$$

The differential probability of the Compton process is

$$dP^c = \frac{\alpha\omega' |\mathcal{M}[s(\omega')]|^2}{16\pi^2 (pk)(p'k)} d\omega' d\Omega, \tag{29}$$

where $d\Omega = d\phi d\theta$ is the solid angle element related to the emitted photon energy ω'. The dependence of the Compton

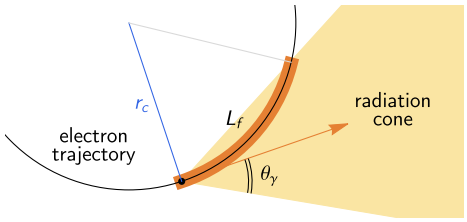

FIG. 10. Classically, the photon formation length L_f can be related to the emission angle θ_γ and the instantaneous radius of curvature r_c of the electron trajectory. From Blackburn, Seipt *et al.*, 2020.

process on the plane-wave field parameters, the amplitude and temporal profile, is encoded in the $\mathcal{V}_{0,\pm,2}$ integrals. These integrals can be evaluated numerically (Mackenroth and Di Piazza, 2011; Seipt and Kämpfer, 2011; Krajewska and Kamiński, 2012) using a saddle point method for highly oscillating phase integrals (Narozhnyi and Fofanov, 1996; Mackenroth, Di Piazza, and Keitel, 2010; Seipt *et al.*, 2015), or analytically (Seipt *et al.*, 2016).

3. Formation length

The radiation formation length or the coherence interval is the spacetime region where the functions that determine the probability of the processes in strong fields are formed (Ritus, 1985). This parameter plays an important role in calculation and analysis of the Compton and Breit-Wheeler processes since the particle interactions over this interval might lead to suppression or enhancement of total intensity or the shape of the spectrum.

There are several approaches to defining the formation length in the classical theory (Baier and Katkov, 2005; Uggerhøj, 2005). First, one can consider it to be the distance L_f traveled before an electron, moving with velocity β, and an emitted photon are separated by $\lambda/2\pi$, where λ is the photon wavelength. For the ultrarelativistic case, this gives

$$L_f = \frac{2\gamma^2 c}{\omega}. \tag{30}$$

Second, the theory of synchrotron emission in the magnetic field can be used. Taking into account the emission cone of $1/\gamma$, the gyromagnetic curvature, and the characteristic synchrotron radiation frequency, one arrives at a similar expression for L_f; see Eq. (15).

Blackburn, Seipt *et al.* (2020) used a more general, geometric approach in which the formation length of a photon emitted at an angle θ to the electron momentum is related to the instantaneous radius of curvature of the electron trajectory r_c by $L_f = 2r_c\theta$; see Fig. 10. The radius of curvature is given by $r_c = \lambda\!\!\!^{-}(\gamma^2-1)[\chi^2-(\mathbf{E}+\mathbf{v}\times\mathbf{B})^2/E_{\rm cr}^2]^{-1/2}$ for a constant, homogeneous field (Seipt and Thomas, 2019). For $\gamma \gg 1$, $r_c \simeq \lambda\!\!\!^{-}\gamma^2/\chi$. We note that for the case of a plane EM wave, where $\chi = 2a_0\gamma(\hbar\omega_0/mc^2)$ and taking $\theta = 1/\gamma$ as a characteristic value, a well-known result can be recovered [$L_f = c/a_0\omega_0$] (Ritus, 1985). This can also be obtained from Eq. (30) by substituting the characteristic frequency of the emitted photon ($\omega \sim \omega_0 a_0\gamma^2$) in synchrotron radiation. By taking into account the angular dependence of the photon emission, one may show that the formation length depends on the photon energy (Blackburn, Seipt *et al.*, 2020):

$$L_f \simeq \frac{c\chi^{1/3}}{a_0\omega_0}\left(\frac{1-f_c}{f_c}\right)^{1/3}. \tag{31}$$

Thus, even for strong fields, photons emitted with sufficiently low energy can have a formation length comparable to the wavelength of the background field; see Fig. 3. This result is consistent with that obtained from a full theoretical analysis from SFQED, which we now outline.

Calculating the probability of photon emission in a pulsed plane wave dP^c in QED involves a double integral over phases ϕ_1 and ϕ_2 because the amplitude M [Eq. (25)] is squared. By redefining this as an integral over the average and interference phases $\phi_{\rm av} = (\phi_1+\phi_2)/2$ and $\phi_{\rm in} = (\phi_1-\phi_2)/2$, respectively, one can identify the range of $\phi_{\rm in}$ that provides the dominant contribution to the "local" rate $dP^c/d\phi_{\rm av} \sim \int\cdots d\phi_{\rm in}$ (Nikishov and Ritus, 1964; Ritus, 1985; Harvey, Ilderton, and King, 2015; Di Piazza *et al.*, 2018; Ilderton, King, and Seipt, 2019). The size of this region, which can be identified as the "formation phase," depends on both a_0 and the light-front momentum fraction of the emitted photon (Di Piazza *et al.*, 2018).

4. The locally constant crossed field approximation

If the characteristic length or duration of a SFQED process is much smaller than the respective spatial and temporal inhomogeneities of the electromagnetic field in which it takes place, the local probability of the process can be calculated in the framework of the locally constant field approximation (LCFA) (Reiss, 1962; Ritus, 1985; Baier, Katkov, and Strakhovenko, 1998). This approximation is based on the fact that the domain of SFQED includes high-energy (ultrarelativistic) particles and high-intensity electromagnetic fields; see Fig. 3. When these fields are transformed into the ultrarelativistic particle's rest frame, they become mutually perpendicular electric and magnetic fields of almost equal amplitude. In most cases these high-intensity fields come from laser pulses and are characterized by a field amplitude $a_0 \gg 1$ and a wavelength λ for which the formation length of the multiphoton Compton and Breit-Wheeler processes are much shorter than the laser wavelength. This leads to an assumption that the probabilities of these processes in an arbitrary field can be obtained as an integral over the time and space of the corresponding probability in a constant crossed field calculated at local value of the field. We note that the same method can be used to calculate the probability of Schwinger pair production in an arbitrary electromagnetic field (Narozhny *et al.*, 2004a), although in this case one need not assume that the field is crossed. This approximation underpins the numerical tools used to simulate laser-matter interactions in the quantum regime, which we discuss in Sec. III. Benchmarking of the LCFA, the limits of its applicability, and the means to go beyond it are discussed in Sec. VII.A.

In what follows we revisit the multiphoton Compton and Breit-Wheeler processes in a constant crossed field

(Ritus, 1985). These processes can be characterized by differential probability rates, i.e., probability per unit time and f, where the latter quantifies the fraction of energy that goes to the created photon ($f = f_c$) or electron or positron ($f = f_b$), respectively. These differential probabilities for both processes can be written in the following form:

$$\frac{dP}{df} = -\frac{\alpha}{\lambda\!\!\!^{-}/c}\frac{1}{l_0}F_{\mp}(\xi,\nu), \tag{32}$$

where the function $F_{\pm}(\xi,\nu)$ is

$$F_{\pm}(\xi,\nu) = \frac{2^{-(1\pm1)/2}}{\sqrt{3}\pi}\left[\int_{\xi}^{\infty} K_{1/3}(z')dz' \pm \nu K_{2/3}(\xi)\right]. \tag{33}$$

For the Compton process, the relevant subscript is a plus sign and $P = P^c$, $f = f_c$, $l_0 = \gamma_e$, $\xi = \xi_c$, and $\nu = \nu_c$, where

$$\xi_c = \frac{2}{3}\frac{f_c}{(1-f_c)\chi_e}, \qquad \nu_c = 1 - f_c + \frac{1}{1-f_c}. \tag{34}$$

For the Breit-Wheeler process, the relevant subscript is a minus sign and $P = P^b$, $f = f_b$, $l_0 = \hbar\omega/mc^2$, $\xi = \xi_b$, and $\nu = \nu_b$, where

$$\xi_b = \frac{2}{3}\frac{1}{f_b(1-f_b)\chi_\gamma}, \qquad \nu_b = \frac{1-f_b}{f_b} + \frac{f_b}{1-f_b}. \tag{35}$$

We can also express the total power radiated by an electron in the Compton process as

$$\mathcal{P}_{\rm rad} = mc^2\gamma\int_0^1 f_c\frac{dP^c}{df_c}df_c. \tag{36}$$

The explicit form of these variables allows us to emphasize the similarities and differences between Compton and Breit-Wheeler processes. For $f_{(c,b)} \to 1$, i.e., when almost all energy of an initial particle is transferred to a photon in a Compton process or to either an electron or positron in a Breit-Wheeler process, ξ_c and ξ_b as well as ν_c and ν_b demonstrate the same behavior $\xi_{(c,b)} \to \infty$ and $\nu_{(c,b)} \to \infty$. In the opposite situation of $f_{(c,b)} \to 0$, one can see that $\xi_c \to 0$ and $\nu_c \to 2$, while $\xi_b \to \infty$ and $\nu_b \to \infty$. Thus, in the first case the differential probabilities of the Compton and Breit-Wheeler processes should be similar. Moreover, we note that the Breit-Wheeler differential probability is symmetric with respect to $f_b \to 1 - f_b$.

One can express the rates using the synchrotron functions as follows (Gonoskov *et al.*, 2015) [see the derivation in the Appendix given by Harvey *et al.* (2016)]:

$$\frac{dP}{df_{c,b}} = \frac{\sqrt{3}\alpha c\chi}{l_0\lambda\!\!\!^{-}} \times \begin{cases} \dfrac{(1-f_c)}{f_c}\left[F_1(\xi_c) + \dfrac{f_c^2}{1-f_c}F_2(\xi_c)\right], \\ (f_b-1)f_bF_1(\xi_b) + F_2(\xi_b), \end{cases} \tag{37}$$

where $F_1(\xi) = \xi\int_\xi^\infty dxK_{5/3}(x)$ and $F_2(\xi) = \xi K_{2/3}(\xi)$ are the first and second synchrotron functions. In Eq. (37), the use of synchrotron functions makes the transition to classical synchrotron emission apparent ($f_{c,b} \to 0$, $\xi_c \to 0$, and $\xi_b \to \infty$), as expressed by the first synchrotron function [Eq. (22)].

a. Differential probabilities $f_{(c,b)} \to 1$

In this case Eq. (32) can be integrated to yield the following result:

$$dP = \frac{2}{3\mp1}\frac{\alpha c}{\pi\lambda\!\!\!^{-}l_0}\frac{\chi^{1/2}}{(1-f)^{1/2}}\exp[-\xi]df, \tag{38}$$

which highlights the similarities between dP^c and dP^b in this limit. Each of these functions has a maximum at

$$f = 1 - \frac{4}{3\chi}, \tag{39}$$

which corresponds to the enhancement of the high-energy electron-positron (photon) production in the $\gamma \to e^-e^+$ ($e \to \gamma e$) process. However, for this maximum to exist the condition $\chi_e > 4/3$ should be satisfied for the Compton process and the condition $\chi_\gamma > 8$ should be satisfied for the Breit-Wheeler process (Bulanov, Schroeder *et al.*, 2013).

b. Differential probabilities $f_{(c,b)} \to 0$

The differential probability scales as $f_c^{-2/3}$ in this case:

$$\frac{dP^c}{df_c} = -\frac{2\alpha c}{3^{1/3}\pi\Gamma(1/3)\lambda\!\!\!^{-}}\frac{1}{\gamma}\left(\frac{\chi_e}{f_c}\right)^{2/3}, \tag{40}$$

where $f_c \ll 1$ and χ_e. However, the total probability of emission remains finite and the intensity of the radiation emission scales as $f_c^{1/3}$ as $f_c \to 0$.

c. Total probability rates

The total probability of the Compton process is

$$P^c(\chi_e) = -\frac{\alpha c}{2\sqrt{3}\pi^2\lambda\!\!\!^{-}}\frac{\chi_e}{\gamma}\int_0^\infty dy\frac{5+7\zeta+5\zeta^2}{(1+\zeta)^3}K_{2/3}(y), \tag{41}$$

where $\zeta = (3/2)\chi_e y$. For $\chi_e \ll 1$ and $\chi_e \gg 1$ the integration can be carried out, and

$$P^c \simeq \begin{cases} 0.92\frac{\alpha}{\lambda\!\!\!^{-}/c}\sqrt{\frac{I}{I_s}}(1-0.92\chi_e+\cdots), & \chi_e \ll 1, \\ 0.93\frac{\alpha}{\lambda\!\!\!^{-}/c}\sqrt{\frac{I}{I_s}}\chi_e^{-1/3}(1-0.58\chi_e^{-2/3}), & \chi_e \gg 1. \end{cases} \tag{42}$$

The probability of the Breit-Wheeler process is

$$P^b = -\frac{\alpha c\chi_\gamma}{32\sqrt{3}\pi^2\lambda\!\!\!^{-}}\frac{m_ec^2}{\hbar\omega}\int_{8/3\chi_\gamma}^\infty\frac{(8\zeta+1)K_{2/3}(y)}{\zeta\sqrt{\zeta(\zeta-1)}}dy, \tag{43}$$

where $\zeta = (3/8)\chi_\gamma y$. For $\chi_\gamma \ll 1$ and $\chi_\gamma \gg 1$ the integration can be carried out and

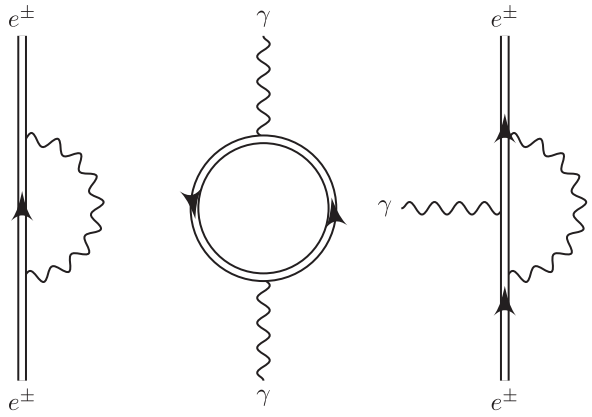

FIG. 11. One-loop mass operator, polarization operator, and vertex correction displayed from left to right.

$$P^b = \begin{cases} 0.073\dfrac{\alpha}{\lambda\!\!\!^{-}/c}\left(\dfrac{I}{I_S}\right)^{1/2}\exp\left(-\dfrac{8}{3\chi_\gamma}\right), & \chi_\gamma \ll 1, \\ 0.67\dfrac{\alpha}{\lambda\!\!\!^{-}/c}\left(\dfrac{I}{I_S}\right)^{1/2}\chi_\gamma^{-1/3}, & \chi_\gamma \gg 1. \end{cases} \tag{44}$$

We note that the probability of the Breit-Wheeler process decreases for both small and large values of parameter χ_γ. This means that there is a value of χ_γ that maximizes the probability of pair production. From Eq. (43) we find that the value is $\chi_\gamma^{\max} \approx 12$ and the maximum probability is $P^b_{R,\max} \simeq (\alpha/5)(c/\lambda\!\!\!^{-})\sqrt{I/I_S}$. It is proportional to the square root of the intensity.

5. Radiative corrections

Most of the analytical studies of strong-field QED phenomena have been carried out at tree level, mainly due to the exploratory nature of these studies and because experimental results did not require calculations at high accuracy. The experiments (Bula *et al.*, 1996; Bamber *et al.*, 1999; Cole *et al.*, 2018; Poder *et al.*, 2018) produced only a limited number of events, mostly establishing the understanding that strong-field effects exist and can have a strong influence on the charged particle dynamics in these fields. However, the future development of theory and experiments would require more accurate calculations. Moreover, there are several theoretical questions that require such calculations to be resolved. The calculations of radiative corrections at one-loop level, mass and polarization operators, and vertex radiative correction (see Fig. 11), as well as at higher orders, were reported on by Ritus (1970, 1972a, 1972b), Narozhny (1979, 1980), and Morozov, Narozhnyi, and Ritus (1981) for crossed EM fields, and in plane waves for mass and polarization operators by Baier, Katkov, and Strakhovenko (1975a, 1975b) and Becker and Mitter (1975). More recent work on the radiative corrections was given by Akhmedov (1983, 2011), Fedotov (2017), Di Piazza and Lopez-Lopez (2020), and Mironov, Meuren, and Fedotov (2020), where the vertex radiative corrections and first-order radiative corrections to the Compton scattering have been calculated. In addition, Edwards and Ilderton (2021) studied the impact of all-orders radiative corrections.

a. Polarization and mass operators

The possibility of the Breit-Wheeler process in the constant electromagnetic field leads to the fact that the external field plays a role of a homogeneous anisotropic medium with dispersion and absorption. The index of refraction of such a medium can be defined in terms of the photon mass $1 - n_{||,\perp} = \mu^2_{||,\perp}/2k_0^2$, where the photon mass is defined as follows through the probability of the Breit-Wheeler process: $P_{||,\perp} = -(n/k_0)\Im(\mu^2_{||,\perp})$. Following Ritus (1985), we obtain the following expression for the polarization operator:

$$\mu^2_{||,\perp}(\chi_\gamma) = \frac{\alpha m^2}{6\pi}\int_1^\infty du\,\frac{8u+1\mp 3}{zu\sqrt{u(u-1)}}f'(z), \tag{45}$$

where $f(z) = i\int_0^\infty dt\,\exp -i(zt + t^3/3)$ and $z = (4u/\chi_\gamma)^{2/3}$. For $\chi_\gamma \ll 1$ and $\chi_\gamma \gg 1$ the asymptotic expressions can be derived from Eq. (45) as follows:

$$\mu^2_{\pm} = -\alpha m_e^2\left[\frac{11\mp 3}{90\pi}\chi_\gamma^2 + i\sqrt{\frac{3}{2}}\frac{3\mp 1}{16}\chi_\gamma e^{-8/3\chi_\gamma}\right] \tag{46}$$

for $\chi_\gamma \ll 1$, and

$$\mu^2_{\pm} = -\alpha m_e^2\left[\frac{10\mp 2}{84\pi^2}\sqrt{3}\Gamma^4(1-i\sqrt{3})(3\chi_\gamma)^{2/3}\right] \tag{47}$$

for $\chi_\gamma \gg 1$. Analogously, the electron mass operator in constant crossed electromagnetic field can be obtained as follows from the probability of the multiphoton Compton process (Ritus, 1985):

$$\Delta m = \frac{\alpha m}{6\pi}\int_1^\infty du\,\frac{5+7u+5u^2}{z(1+u)^3}f'(z), \tag{48}$$

where $z = (4u/\chi_e)^{2/3}$. The asymptotic expressions for $\chi_e \ll 1$ and $\chi_e \gg 1$ read as follows:

$$\Re(\Delta m) = \frac{4\alpha m}{3\pi}\chi_e^2\left(\log\chi_e^{-1} + C + \frac{1}{2}\log 3 - \frac{33}{16}\right) + \cdots, \tag{49}$$

$$\Im(\Delta m) = -\frac{5\alpha m}{4\sqrt{3}}\chi_e\left(1 - \frac{8\sqrt{3}}{15}\chi_e + \frac{7}{2}\chi_e^2\right) + \cdots \tag{50}$$

for $\chi_e \ll 1$, and

$$\Delta m = \frac{7\Gamma(2/3)(1-i\sqrt{3})\alpha m}{27\sqrt{3}}(3\chi_e)^{2/3} \tag{51}$$

for $\chi_e \gg 1$. Note that both $\mu^2_{||,\perp}$ and Δm in the case of $\chi \gg 1$ demonstrate the $\alpha\chi^{2/3}$ behavior, which points to a possible breakdown of the semiclassical perturbation theory at high values of χ.

b. Cherenkov radiation

As previously mentioned, in the presence of a strong electromagnetic field the QED vacuum behaves as a medium with an index of refraction larger than unity (Narozhnyi, 1969; Ritus, 1970; Dittrich and Gies, 2000; Shore, 2007; Gies, Karbstein, and Kohlfürst, 2018), i.e., the phase velocity of the interacting electromagnetic waves is below the speed of light in vacuum. One of the consequences of this fact is a possibility of the Cherenkov radiation of the high-energy electrons traversing the electromagnetic field (Ritus, 1970; Schwinger, Tsai, and Erber, 1976; Becker, 1977; Ginzburg and Tsytovich, 1979; Dremin, 2002; Macleod, Noble, and Jaroszynski, 2019), which is connected to the radiative corrections. The angle and the intensity of the Cherenkov radiation are determined as follows through the real part of the polarization operator (Ritus, 1985):

$$\theta_{\pm} = \left[-\frac{\Re\mu^2_{\parallel,\perp}(\chi_\gamma)}{\omega'^2} - \frac{m^2}{p_0^2} \right]^{1/2}, \tag{52}$$

$$dI_{\pm} = \alpha \left[-\Re\mu^2_{\parallel,\perp} - \frac{m^2\omega'^2}{p_0^2} \right] \frac{d\omega'}{\omega'}. \tag{53}$$

In classical electrodynamics, as described using the Maxwell equations, the electromagnetic wave frequency and wave vector are related to each other by $\omega^2 - \boldsymbol{k}^2c^2 = 0$. In the quantum vacuum, polarization effects result in the dispersion equation

$$\omega^2 - \boldsymbol{k}^2c^2 - \mu^2_{\pm}(\chi_e)c^2\hbar^{-2} = 0. \tag{54}$$

In the limit $\chi_\gamma \ll 1$, the difference between the index of refraction and unity ($\Delta n_{\pm} = n_{\pm} - 1$) is

$$\Delta n_{\pm} = \alpha \frac{11 \mp 3}{45\pi} \left(\frac{E}{E_S} \right)^2. \tag{55}$$

The introduction of the photon mass leads to the energy conservation equation having two solutions: first, the usual Compton one and, second, the one corresponding to the Cherenkov radiation. Thus, kinematic considerations reveal that the emission of a photon by an electron in a strong electromagnetic field is described using a synergic Cherenkov-Compton process (Bulanov *et al.*, 2019). The estimates show that for a 10 PW laser pulse electrons with an energy more than 10 GeV are needed to observe Cherenkov photons.

c. Fully nonperturbative QED

In most of the previously considered cases, as well as in the cited literature, the radiative corrections either are negligible or make a contribution much smaller than that of the tree-level diagrams. However, in extremely strong electromagnetic fields characterized by $\chi \gg 1$, this hierarchy is no longer valid. According to the Ritus-Narozhny conjecture (Narozhny, 1980; Ritus, 1985), the parameter of the SFQED dressed loop expansion is $\alpha\chi^{2/3}$; see Fig. 12. This means that at $\alpha\chi^{2/3} > 1$ each order of the radiative corrections can no longer be considered small compared to the previous one. Thus, the dressed loop expansion fails, and the existing theoretical framework can no longer be used in this case. Moreover, these results question the applicability of the semiclassical methodology used in QED–particle-in-cell (PIC) simulations (see section III) since they are based upon a separation of timescales. The formation time for quantum processes should be short compared to classical propagation time between incoherent quantum events. However, calculations (for constant crossed fields) show that in extremely strong fields ($\chi \gg 1$) the mean free paths for electrons and photons are on the order of the Compton wavelength $\lambda\!\!\!^{-}_C \sim 1/m$ for $\alpha\chi^{2/3} \sim 1$. The concept of a classical particle and thus classical motion has no meaning on the Compton scale, thereby seriously challenging the applicability of QED PIC at extreme field strengths (Fedotov, 2017). Experimental configurations that have been proposed to reach such extreme conditions include collisions of dense lepton bunches (Yakimenko *et al.*, 2019b), electron beams and high-intensity lasers (Baumann *et al.*, 2019; Blackburn *et al.*, 2019), and electron beams and aligned crystals (Di Piazza *et al.*, 2020).

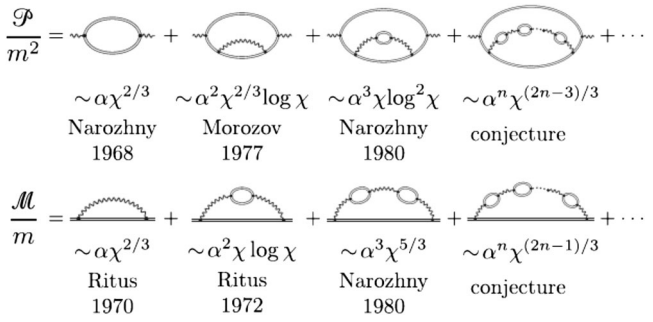

FIG. 12. Dressed loop expansion of the polarization operator P (top row) and mass operator M (bottom row). According to the Ritus-Narozhny conjecture, these diagrams represent the dominant contribution at n loops, and $\alpha\chi^{2/3}$ is the true expansion parameter of SFQED in the regime $\chi \gg 1$. From Yakimenko *et al.*, 2019b.

The previously mentioned calculations were performed in the constant crossed field, which is widely used in QED-PIC simulations, when the separation of scales is assumed to be valid. Ritus (1972a, 1985) noted that, in the case of an alternating field, a logarithmic behavior more typical for QED processes should take place. More detailed considerations of this problem were carried out by Ilderton (2019) and Podszus and Di Piazza (2019), who provided detailed studies of the behavior of Compton and Breit-Wheeler processes in pulsed EM fields in the limit of $\chi \to \infty$. However, the limit $\chi \to \infty$ is the combination of particle energy and field strength, whereas the probability of the process is a function of energy and field strength separately. That is why one needs to distinguish the cases when $\chi \to \infty$ because of $\gamma \to \infty$ from those when $a \to \infty$:

$$P^c \sim \frac{\alpha\chi^{2/3}}{\gamma\omega - kp}, \qquad a_0 \to \infty, \tag{56}$$

$$P^c \sim \frac{\alpha a_0^3}{\chi_e} \log \chi_e, \qquad \gamma \to \infty. \tag{57}$$

Thus, the probability of the Compton process increases with χ_e at high field strength, whereas at high particle energy it decreases with χ_e. Since this probability also determines the magnitude of loop corrections, it means that in one case they can exceed the tree-level contribution, whereas in the other case this is not so. These results indicate that there is no universal high-χ_e behavior. We note that $\alpha\chi^{2/3} > 1$ corresponds to $\chi > 1600$, which is well beyond the reach of current state-of-the-art laser facilities and conventional accelerators.

6. Higher-order processes

The elementary processes shown in Fig. 9 may be combined to form more complex QED interactions. Each additional vertex reduces the total probability, relative to a tree-level process, by a factor of $\alpha \ll 1$. However, this does not necessarily mean that higher-order processes are less probable overall, because of additional volume factors which appear in the cascade contribution (soon to be defined); thus, a two-vertex process, scaling quadratically with pulse duration, can potentially dominate over a single-vertex process, which scales only linearly. Theoretical calculations of these processes, which involve integrating over the momenta of the intermediate (i.e., unobserved) particles, are much more complicated in SFQED than in vacuum QED due to the nontrivial spacetime dependence of the background-field and basis states. The most general case amenable to study is a pulsed plane EM wave, with results also available for constant crossed fields.

Of the two-vertex processes shown in Fig. 13, trident pair creation, the emission of a photon that creates an electron-positron pair, and double nonlinear Compton scattering, the emission of two photons, have attracted the most attention. The former, in particular, represents the first step in the production of an avalanche of secondary particles; see Sec. IV.F. The presence of the background field means that it is possible for the intermediate particle to be real, i.e., on the mass shell, leading to resonances in the probability (Oleinik, 1967). This raises the possibility that a multivertex process can be factorized into a sequence of first-order processes, which occur in real particles. The physical basis for this separation is that the intermediate particle can propagate a macroscopic distance if it is on shell; otherwise, its range is limited by the uncertainty principle to a single formation length. The validity of this factorization, called the "cascade approximation," is essential to numerical simulations of QED processes (Blackburn, 2020).

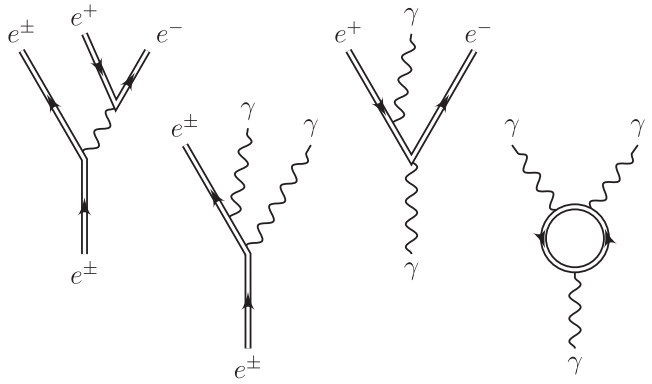

FIG. 13. Examples of higher-order SFQED processes. Trident pair creation, double nonlinear Compton scattering, photoTrident pair creation, and photon splitting are displayed from left to right.

A two-vertex process can in principle be separated into "two-step" and "one-step" components. The one-step component encompasses all contributions to the probability that are not accounted for by the cascade, which includes terms where the intermediary is purely virtual, as well as interference and exchange terms (Ilderton, 2011). Theoretical calculations of two-vertex processes focus on not only their phenomenology but also the relative magnitudes of these two contributions. For double nonlinear Compton scattering this includes monochromatic (Lötstedt and Jentschura, 2009) and pulsed plane waves (Seipt and Kämpfer, 2012; Mackenroth and Di Piazza, 2013), as well as constant crossed fields (King, 2015). Trident pair creation has been studied for pulsed plane-wave backgrounds, to reconsider experimental results (Hu, Müller, and Keitel, 2010; Ilderton, 2011) (see Sec. V) and the cascade and LCFA approximations (Dinu and Torgrimsson, 2018; Mackenroth and Di Piazza, 2018), and for constant crossed field backgrounds (King and Ruhl, 2013; King and Fedotov, 2018). Here the name "trident" encompasses all contributions to the probability; it sometimes refers exclusively to the one-step process (Burke *et al.*, 1997), with the two-step process treated separately as nonlinear Compton scattering followed by nonlinear Breit-Wheeler pair creation.

The two-step contribution is the product of *polarized* subprocesses (King and Ruhl, 2013; King, 2015; Dinu and Torgrimsson, 2020). Numerical implementations of SFQED processes in simulation codes have generally employed polarization-averaged rates. Calculations of the trident pair-creation and double Compton probabilities in a constant crossed field, which compare the uses of polarization-averaged and polarization-resolved rates, indicate that this is accurate to within a few percent (King, Elkina, and Ruhl, 2013; King, 2015). However, the spin and polarization of intermediate particles may evolve under the action of the external field due to factors such as vacuum polarization (King and Elkina, 2016) and spin precession, thus enhancing this difference. We discuss the importance of these dynamics in Sec. II.D and their possible applications in Sec. VI.C.

The dominance of the two-step contribution itself, assuming polarization-resolved subprocesses, is assessed for the trident process in a constant crossed field (King and Ruhl, 2013) and in a pulsed plane wave (Dinu and Torgrimsson, 2018; Mackenroth and Di Piazza, 2018). The error in taking only this contribution is one part in a thousand for $a_0 = 50$ and an electron energy of 5 GeV and becomes substantial for $a_0 < 10$ only if the electron energy exceeds 100 GeV (Mackenroth and Di Piazza, 2018). However, the two-step contribution can be dominant even if $a_0 \simeq 1$ provided that the field duration is sufficiently long (Dinu and Torgrimsson, 2020). Note that in this case the subprocesses must be described with rates that go beyond the LCFA (see Sec. II.B.4), and the treatment of the polarization of the

intermediate particle is more complicated (Dinu and Torgrimsson, 2020).

An approximation to the one-step trident rate, calculated using the Weizsäcker-Williams (WW) approximation (Erber, 1966), has been applied to allow the one- and two-step yields to be compared (Bamber *et al.*, 1999; Bell and Kirk, 2008; Kirk, Bell, and Arka, 2009; Blackburn *et al.*, 2014). While this is a reasonable approximation to the purely virtual component, once exchange and interference contributions are included the total one-step rate is negative for $\chi_e \lesssim 20$ (King and Ruhl, 2013; Dinu and Torgrimsson, 2018; King and Fedotov, 2018). In the high-energy limit (at a fixed a_0), the one-step part gives the dominant contribution and the WW approximation is accurate (Torgrimsson, 2020).

Further higher-order processes include phototrident pair creation (Morozov and Narozhnyi, 1977; Torgrimsson, 2020), photon splitting (Adler, 1971; Akhmadaliev *et al.*, 2002; Di Piazza, Milstein, and Keitel, 2007); Delbrück scattering, the scattering of a photon through a vacuum fluctuation (Milstein and Schumacher, 1994; Di Piazza and Milstein, 2008; Koga and Hayakawa, 2017); and, in part, triple and quadruple nonlinear Compton scattering (Dinu and Torgrimsson, 2019). The interaction where a single electron emits an arbitrarily large number of photons is particularly interesting because it represents the analog of radiation reaction in QED (Di Piazza, Hatsagortsyan, and Keitel, 2010); see Sec. II.C. (Note that QED is a multiparticle theory, and therefore there is no guarantee that only a single electron emerges from the interaction; however, pair creation is negligible for $\chi_e \ll 1$.)

C. Quantum radiation reaction

Radiation reaction appears to be more straightforward, at least conceptually, in QED. The conservation of momentum is applied at the level of the scattering amplitude (see Sec. II.B.2); therefore, when an electron emits a photon in Compton scattering, the self-consistent recoil is automatically accounted for. However, that recoil is proportional to $\hbar$, and it vanishes in the classical limit. The resolution to this problem was proposed by Di Piazza, Hatsagortsyan, and Keitel (2010). A complete calculation of the interaction between an electron and a prescribed strong electromagnetic field in QED means solving for the scattering amplitude, and the final state, for an initial state containing only a single electron (Di Piazza *et al.*, 2012). In the perturbative approach to this problem, cascade processes, which include quantum radiation reaction, manifest themselves as high-order contributions to the S matrix. However, as discussed in Sec. II.B.6, if $a_0 \gg 1$, the small size of the formation length (Ritus, 1985) means that high-order terms are dominated by *incoherent* contributions, where each elementary QED process occurs in a distinct region of space (Di Piazza *et al.*, 2012). Thus, we may identify quantum radiation reaction as the recoil arising from the sequential, incoherent emission of many photons (Di Piazza, Hatsagortsyan, and Keitel, 2010). While the recoil from an individual emission is proportional to $\hbar$, the number of photons emitted $N_\gamma \propto \alpha \propto \hbar^{-1}$, leading to a total momentum change $\Delta p \propto \hbar^0$ that is nonzero in the classical limit.

Provided that $a_0 \gg 1$ and $\chi \lesssim 1$, such that photon emission may be treated as occurring instantaneously and pair creation is negligible, quantum radiation reaction can be included as a supplement to the classical dynamics. The listed conditions indicate that the local constant field approximation is valid and the probability of photon emission is described using the expressions from Sec. II.B.4. The evolution of the electron distribution function $\phi_e(t, \mathbf{r}, \mathbf{p})$, including quantum radiation-reaction effects, is governed by the following kinetic equation (Shen and White, 1972; Sokolov *et al.*, 2010; Elkina *et al.*, 2011; Bulanov, Schroeder *et al.*, 2013; Neitz and Di Piazza, 2013; Ridgers *et al.*, 2014):

$$\frac{\partial \phi_e}{\partial t} + \frac{\mathbf{p}}{\gamma m}\cdot\frac{\partial \phi_e}{\partial \mathbf{r}} - e\left(\mathbf{E} + \frac{\mathbf{p}\times\mathbf{B}}{\gamma m}\right)\cdot\frac{\partial \phi_e}{\partial \mathbf{p}} = -\phi_e \int w_{e\to e\gamma}(\mathbf{p}, \mathbf{q}) d^3\mathbf{q} + \int \phi'_e w_{e\to e\gamma}(\mathbf{p}', \mathbf{p}' - \mathbf{p}) d^3\mathbf{p}', \tag{58}$$

where we take $\phi_e = \phi_e(t, \mathbf{r}, \mathbf{p})$ and $\phi'_e = \phi_e(t, \mathbf{r}, \mathbf{p}')$ for brevity. The right-hand side of Eq. (58) is a collision operator that accounts for the dynamical effect of photon emission, i.e., radiation reaction. Quantum effects are manifest in the dependence on $w_{e\to e\gamma}(\mathbf{p}, \mathbf{q}) d^3\mathbf{q}$, the probability rate that an electron with momentum $\mathbf{p}$ emits a photon with momentum $\mathbf{q} = \hbar\mathbf{k}$. If the pair creation is not negligible, it couples the electron and positron distribution functions to the photon distribution function ϕ_γ, and three coupled kinetic equations can be used to describe the interaction of electrons, positrons, and photons with strong EM fields, which is discussed in Sec. III.

The evolution of the distribution function, including photon emission, at an arbitrary χ_e is generally obtained using a numerical solution of Eq. (58). The relevant methods are discussed in Sec. III. However, it is possible to obtain analytical insights when considering specific field configurations or if χ_e is not too large. In the former case, one can apply the Markov chain formalism to assess the long-term evolution of the distribution function (Bashinov, Kim, and Sergeev, 2015). In the latter case, Eq. (58) can be reduced to a Fokker-Planck equation (Neitz and Di Piazza, 2013). This corresponds to taking the first two terms in a Kramers-Moyal expansion of the collision operator (Niel *et al.*, 2018). When one follows Vranic, Grismayer *et al.* (2016),

$$\frac{d\phi_e}{dt} = \frac{\partial}{\partial p_i}\left[A_i \phi_e + \frac{1}{2}\frac{\partial}{\partial p_j}(B_{ij}\phi_e)\right], \tag{59}$$

where the drift and diffusion coefficients A and B are, respectively,

$$A_i = \int q_i w(\mathbf{p}, \mathbf{q}) d^3\mathbf{q}, \qquad B_{ij} = \int q_i q_j w(\mathbf{p}, \mathbf{q}) d^3\mathbf{q} \tag{60}$$

and the indices i, j denote components of the momentum. An equivalent expression is obtained in terms of the light-front momentum p^- given by Neitz and Di Piazza (2013). The validity of the Fokker-Planck approach is limited by the importance of higher orders in the Kramers-Moyal expansion: the third term is larger than 10% of the diffusion term if

$\chi_e \gtrsim 0.25$, and as χ_e approaches unity the expansion breaks down (Niel *et al.*, 2018). Physically, this means that the momentum change caused by emitting a single photon becomes as important as the cumulative momentum change from emitting many (Bell and Kirk, 2008).

Further analytical insights can be obtained by considering moments of the distribution function. Results obtained for specific field geometries include the evolution of the mean energy of electrons in a rotating electric field, assuming that $\chi_e \ll 1$ (Elkina *et al.*, 2011), and the mean and standard deviations of the light-front momentum (or energy) of an electron beam in a plane-wave laser pulse, assuming that $\chi_e \ll 1$ (Neitz and Di Piazza, 2013; Yoffe *et al.*, 2015; Vranic, Grismayer *et al.*, 2016), and extended to arbitrary χ_e (Ridgers *et al.*, 2017). The evolution of the mean Lorentz factor μ_γ for an arbitrary field configuration with electric component $\mathbf{E}$ is given by (Niel *et al.*, 2018)

$$\frac{d\mu_\gamma}{dt} = -\frac{e\langle \mathbf{u}\cdot\mathbf{E}\rangle}{mc} - \frac{2\alpha c}{3\lambda\!\!\!^{-}}\langle \chi_e^2 G(\chi_e)\rangle, \tag{61}$$

where $\langle\cdots\rangle$ denotes the population average. If the effect of the external field may be neglected, such as in a magnetic field or a plane wave with an amplitude $a_0 \ll \gamma$, the evolution of the nth-order central moment $\langle(\gamma-\mu_\gamma)^n\rangle$ may be given analytically (Niel *et al.*, 2018).

An important auxiliary function appears in Eq. (61), providing the link to the single-particle emissivity. The factor $G(\chi_e)$ gives the ratio between the instantaneous radiation powers predicted by QED and the classical theory (Erber, 1966; Sokolov and Ternov, 1968); this is sometimes referred to as the "Gaunt factor," as it is a multiplicative (quantum) correction to a classical result that is first derived in the context of absorption (Gaunt, 1930). Using the expression for total emitted power, we have $G(\chi_e) = (\lim_{\chi_e\to 0}\int \hbar\omega\, dI)^{-1}(\int \hbar\omega\, dI)$. Expressed as a single integral (Sokolov and Ternov, 1968; Ritus, 1985; Baier, Katkov, and Strakhovenko, 1998),

$$G(\chi) = \frac{3\sqrt{3}}{\pi}\int_0^\infty \frac{8u + 15\chi u^2 + 18\chi^2 u^3}{(2+3\chi u)^4} K_{2/3}(u)\,du \tag{62}$$

$$\simeq \begin{cases} 1 - \dfrac{55\sqrt{3}}{16}\chi + 48\chi^2, & \chi \ll 1, \\ \dfrac{16\Gamma(2/3)}{3^{1/3}27}\chi^{-4/3}, & \chi \gg 1, \end{cases} \tag{63}$$

where K is a modified Bessel function of the second kind and Γ is the gamma function. These are plotted in Fig. 14, which shows that the reduction becomes significant even at $\chi_e \simeq 0.1$. The asymptotic expressions given in Eq. (63) are within 5% of the true value for $\chi < 0.05$ and $\chi > 200$, respectively (Blackburn, 2020). Analytical approximations to Eq. (62) include $G(\chi) \simeq [1 + 4.8(1+\chi)\ln(1+1.7\chi) + 2.44\chi^2]^{-2/3}$, which has a fractional error smaller than 2% across the full range of χ (Baier, Katkov, and Strakhovenko, 1998), and $G(\chi) = (1 + 12\chi + 31\chi^2 + 3.7\chi^3)^{-4/9}$, which is accurate to within 2% for $\chi < 5$ and $\chi > 1000$ (Thomas *et al.*, 2012).

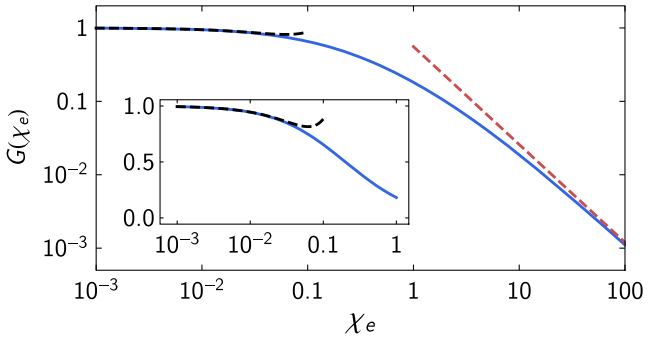

FIG. 14. $G(\chi_e)$ is the factor by which quantum effects reduce the radiation power from its classically predicted value: the full expression (blue solid line) and limiting values at small and large χ_e (black dashed line on the left and red dashed line on the right, respectively) from Eqs. (62) and (63), respectively.

The classical limit of Eq. (59) allows us to recover a deterministic radiation-reaction force, as discussed in Sec. II.A. Assuming that photons are emitted parallel to the electron momentum, i.e., that $\gamma \gg 1$, the drift and diffusion coefficients are $A = 2\alpha mc^2\chi_e^2/3\lambda\!\!\!^{-}$ and $B = 55\alpha m^2c^3\chi_e^3\gamma/24\sqrt{3}\lambda\!\!\!^{-}$ to lowest order in χ_e (Neitz and Di Piazza, 2013; Vranic, Grismayer *et al.*, 2016). Only A is nonzero in the classical limit $\hbar \to 0$, in which case the characteristics of Eq. (59) satisfy $dp_i/dt = -A_i$ (Vranic, Grismayer *et al.*, 2016), i.e., the Landau-Lifshitz equation in the ultrarelativistic limit. This is also obtained by setting $G(\chi_e) = 1$ in Eq. (61).

Taking its classical limit of QED is also a means of distinguishing between the different classical theories of radiation reaction discussed in Sec. II.A. The evolution of the expectation value of the momentum (Krivitski and Tsytovich, 1991; Ilderton and Torgrimsson, 2013b) and the position (Ilderton and Torgrimsson, 2013a) of a charge interacting with an external EM field have been shown to obey classical equations of motion in the limit in which $\hbar \to 0$. In particular, it has been shown that, at first order in α, only the LAD, Landau-Lifshitz, and Eliezer-Ford-O'Connell theories are consistent with QED (Ilderton and Torgrimsson, 2013a). (Recall that the Landau-Lifshitz equation is itself the result of a perturbative expansion of the LAD equation, in the small parameter $\tau_{\rm rad} \propto \alpha$; see Sec. II.A.2.) These three equations could be distinguished at second order in α, although the much larger number of contributing diagrams at this order significantly increases the difficulty of the calculation (Ilderton and Torgrimsson, 2013a). The use of resummation techniques allowed Torgrimsson (2021) to recover the LL equation from QED to all orders in α.

The Landau-Lifshitz equation, being consistent with QED as previously discussed, forms the basis for a "semiclassical" (also called "modified classical") theory of radiation reaction. One may appeal to momentum conservation to argue that, because quantum effects reduce the radiation power by a factor $G(\chi_e)$, the radiation-reaction force must also be reduced by the same factor (Erber, 1966). Thus, the equation of motion becomes

$$\frac{dp^\mu}{d\tau} = -\frac{eF^{\mu\nu}p_\nu}{mc} + G(\chi_e)g^\mu_{\rm LL}, \tag{64}$$

where g_{LL} is the Landau-Lifshitz force given in Eq. (19). Its use has also been justified on the grounds that the Fokker-Planck formulation [Eq. (59)] is equivalent to a stochastic differential equation for the single-particle momentum (Neitz and Di Piazza, 2013; Niel *et al.*, 2018) in which the deterministic components are as given by Eq. (64). Therefore the modified classical model neglects the stochastic effects of quantum radiation reaction, which are discussed in Sec. IV.C.

An alternative radiation-reaction force that accounts for quantum corrections to the radiation power was proposed by Sokolov (2009). A key aspect is that collinearity between the charge's four-momentum and four-velocity is abandoned in order to renormalize the LAD equation. However, it has been shown that the momentum evolution predicted by this model is not consistent with the classical limit of QED, unlike the Landau-Lifshitz, Ford-O'Connell, and LAD equations (Ilderton and Torgrimsson, 2013a). It has been suggested that it is the definition of momentum in QED that should be reassessed in light of these results (Capdessus *et al.*, 2016), as the Sokolov model does produce the correct velocity and trajectory (Ilderton and Torgrimsson, 2013a). Nevertheless, questions arise as to the model's validity even without our appealing to QED, as it is capable of causality violation for sufficiently large fields or particle energies (Burton and Noble, 2014): the four-velocity u^μ satisfies $u^2 = c^2[1 - (2\alpha\chi_e/3)^2]$ rather than $u^2 = c^2$. As a practical matter, the differences between the various formulations of classical radiation reaction, including the Sokolov model, are small in most scenarios of interest (Vranic, Martins *et al.*, 2016).

D. Spin light and spin dynamics

Electrons are spin-1/2 fermions with an intrinsic magnetic moment $\boldsymbol{\mu}_e = -(1/2)g_s\mu_B\hat{\mathbf{s}}$ antiparallel to the spin axis $\hat{\mathbf{s}}$, where $g_s \simeq 2$ is the spin g factor and $\mu_B = e\hbar/2mc$ is the Bohr magneton. This magnetic moment is a dynamical degree of freedom that couples to the radiation field, affecting the emission spectrum, and to external electromagnetic fields, leading to spin precession (Thomas, 1926; Bargmann, Michel, and Telegdi, 1959) and additional forces on the particle (Gerlach and Stern, 1922; Jackson, 1999). In this section we review the role of spin in terms of these couplings, which are illustrated in Fig. 15.

In classical electromagnetism, the power radiated by a magnetic moment $\boldsymbol{\mu}$ that is accelerated by a static magnetic field $\mathbf{B}$ is given by $\mathcal{P}_\mu = (\alpha/6)(mc^3/\lambda\!\!\!^{-})(\mu_\perp^2/\mu_B^2)\chi_e^4$, where $\mu_\perp$ is the component of the magnetic moment perpendicular to $\mathbf{B}$ and $\chi_e = \gamma B/B_{\mathrm{cr}}$ (Bordovitsyn, Ternov, and Bagrov, 1995; Jackson, 1999). [For a neutral particle, $\mathcal{P}_\mu$ would be the only contribution to radiation emission; this has been explored theoretically for neutrinos in particular (Morley and Buettner, 2015; Formanek *et al.*, 2018).] As the spin magnetic moment is a purely quantum effect, so too is its contribution to radiation emission ($\mathcal{P}_\mu \propto \hbar^2$). For an electron, $\mathcal{P}_\mu$ is smaller than the charge contribution by a factor of $\sim\chi_e^2$ in the classical regime $\chi_e \ll 1$. It is more significant in the quantum regime $\chi_e \gtrsim 1$, as radiation associated with changes of the electron spin (spin flips) dominates the high-energy part of the spectrum (Sørensen, 1996).

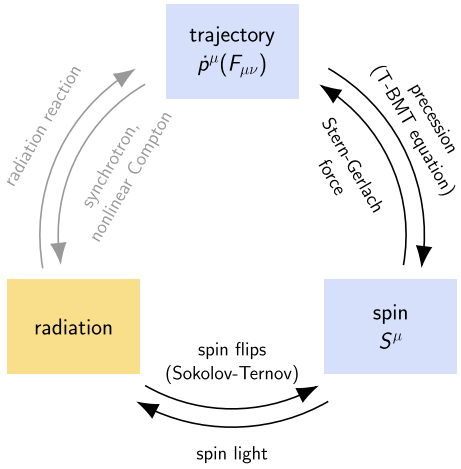

FIG. 15. Overview of the ways that spin influences, and is influenced by, particle degrees of freedom (top and right blue panels) and radiation (left yellow panel). Individual couplings are denoted by arrows, with those introduced in Sec. II.D given in black. Adapted from Thomas *et al.*, 2020.

The importance of the spin to radiation emission, in the quantum regime, may be understood using the following argument (Kirsebom *et al.*, 2001): in the electron instantaneous rest frame, there is an energy difference of $\Delta\mathcal{E} = 2\mu_B|\mathbf{B}_{\mathrm{rf}}|$ between states where the electron spin is aligned parallel and antiparallel to the rest-frame magnetic field $\mathbf{B}_{\mathrm{rf}}$. A photon emitted in a spin-flip transition therefore has a typical energy (in the laboratory frame) of $\hbar\omega = \gamma\Delta\mathcal{E} = \gamma mc^2\chi_e$. For $\chi_e \gtrsim 1$, kinematic pileup means that these photons are concentrated in the tail of the emission spectrum. This may be seen explicitly as follows by taking the difference between the emission rate of a spin-1/2 electron and that for a spinless electron, i.e., Eq. (22) with the recoil correction [Eq. (23)] (Sørensen, 1996):

$$\Delta\frac{dW}{d\hbar\omega} = \frac{\alpha}{\sqrt{3}\pi\hbar\gamma^2}\frac{f^2}{1-f}K_{2/3}(\xi_q). \tag{65}$$

Equation (65) gives the "spin light" contribution to the emission spectrum. It peaks at $f \simeq \chi_e/(1+\chi_e)$, which bears out the previously stated argument for the typical energy once it has been corrected for recoil. Note that Eq. (65) is calculated for constant crossed fields. The role of spin is further elucidated by exact QED calculations that compare the scattering and creation of Klein-Gordon (spin-0) and Dirac (spin-1/2) electrons in a pulsed plane-wave background (Panek, Kamiński, and Ehlotzky, 2002; Boca, Dinu, and Florescu, 2012; Krajewska and Kamiński, 2013; Jansen *et al.*, 2016).

The spin contribution to radiation depends on the orientation of the spin with respect to the external electromagnetic field. This is captured by emission rates that are resolved in the initial and final spin states of the participating particles (Sokolov and Ternov, 1968; Seipt *et al.*, 2018), whereas Eq. (65), like the results in Sec. II.B.4, is calculated for

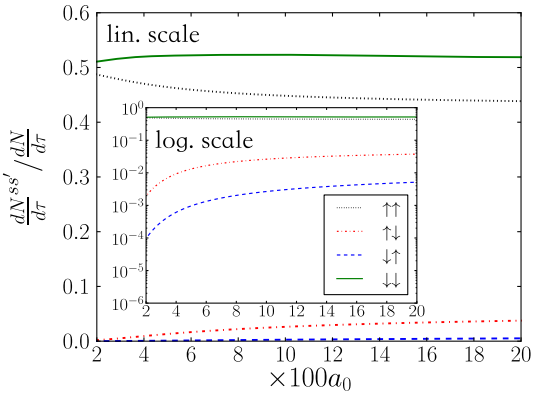

FIG. 16. Spin-resolved photon-emission rates $dN^{s,s'}/d\tau$, normalized to the spin-averaged rate $dN/d\tau$, for electrons orbiting in a rotating electric field of normalized amplitude a_0. Here s and s' are the projections of the electron initial and final spin on the axis of rotation. From Del Sorbo *et al.*, 2017.

unpolarized electrons. A dramatic consequence of spin dependence is the Sokolov-Ternov effect, where lepton beams, orbiting in a magnetic field, self-polarize due to the asymmetric emission probabilities for spin-up and spin-down states (Ternov, Loskutov, and Korovina, 1962; Sokolov and Ternov, 1968; Jackson, 1976).

This is also predicted to occur at the magnetic node of the EM standing wave formed by two counterpropagating lasers, but over much shorter timescales: the asymmetric probability of emission for electrons in a rotating electric field, shown in Fig. 16, leads to near-total polarization of the electron population within a few femtoseconds at intensities of 10^{23} W cm^{-2} (Del Sorbo *et al.*, 2017; Del Sorbo, Seipt *et al.*, 2018). The prospect of using intense lasers to polarize particles (or to induce their creation) has led to considerable activity in recent years, largely focused on laser collisions with ultrarelativistic electron beams; this is discussed in Sec. VI.C.

Spin polarization must be defined with respect to a particular basis. (Recall that only one component of the spin can be defined at any one time.) A fixed choice of quantization axis means that polarization is defined in only one dimension; recently a method was proposed that can simulate the evolution of all three components of the polarization vector (Li, Chen *et al.*, 2020). For a plane EM wave, an appropriate nonprecessing quantization axis is given by $\zeta^\mu = \beta^\mu - (p\cdot\beta/\kappa\cdot p)\kappa^\mu$, where p is the electron four-momentum, κ is the wave vector, and $\beta = (0,\boldsymbol{\beta})$, where $\boldsymbol{\beta}$ is a unit vector directed along the wave's magnetic field (as seen in the laboratory frame) (King, 2015). In a static magnetic field, $\boldsymbol{\zeta}$ is directed parallel to the field (Sokolov and Ternov, 1968); in a rotating electric field, it is directed along the electric field's axis of rotation (Del Sorbo *et al.*, 2017). The occupancies of the spin-up and spin-down states, as defined with respect to this axis, do not change except by interaction with the radiation field. This can occur even without emission (Meuren and Di Piazza, 2011); see Sec. II.B.5.

In general, studies of laser–electron-beam or laser-plasma interactions must also take into account the interaction of the spin with the external electromagnetic field. Two such effects are shown in Fig. 15: spin precession and spin forces. The former can be modeled classically using the Thomas-Bargmann-Michel-Telegdi (TBMT) equation (Thomas, 1926; Bargmann, Michel, and Telegdi, 1959). For an electron with spin four-vector S^μ and a normalized momentum $u^\mu = p^\mu/mc$ in an electromagnetic field $F_{\mu\nu}$ this reads

$$\frac{dS_\mu}{d\tau} = -\frac{e}{m}\left[\frac{g_s}{2}F_{\mu\nu}S^\nu + \frac{g_s-2}{2}(S^\nu F_{\nu\rho}u^\rho)u_\mu\right], \qquad (66)$$

where $S^2 = -1$. According to Eq. (66), a plane EM wave causes the spin of an electron with $g_s = 2$ to precess but does not change its asymptotic value. (The precession of the spin vector inside the wave is necessary to maintain the relation $S_\mu p^\mu = 0$ because the electron momentum is time dependent.) The same result is recovered from the quantum description by taking expectation values of bilinears of Volkov states (Seipt *et al.*, 2018). The TBMT equation has been used in particle-in-cell codes to study spin evolution in laser-driven wakefields (Vieira *et al.*, 2011; An *et al.*, 2019; Wen, Tamburini, and Keitel, 2019).

The spin modifies the particle momentum indirectly by affecting the radiation power (Del Sorbo *et al.*, 2017), and thereby the strength of radiation reaction. Signatures of spin-dependent radiative deflection in tightly focused lasers were studied by Geng *et al.* (2020). However, if the external electromagnetic field is nonhomogeneous, its interaction with the spin also leads directly to a force on the particle; this contribution to the equation of motion is often referred to as the "Stern-Gerlach force," after the seminal experiment that demonstrated the intrinsic quantum nature of the electron magnetic moment (Gerlach and Stern, 1922).

This force is proportional to the gradient of the electromagnetic field, which means that it is much weaker than the Lorentz force (Vieira *et al.*, 2011) and radiation reaction (Tamburini *et al.*, 2010) in interactions with intense optical lasers; see also Thomas *et al.* (2020). On the other hand, it plays a more significant role in fields with high-frequency components, as found astrophysically (Mahajan, Asenjo, and Hazeltine, 2015), in wave-breaking plasmas (Flood and Burton, 2015), or in collisions with intense x rays (Wen, Bauke, and Keitel, 2016). While spin-dependent dynamics are captured without approximation using the Dirac equation (Dirac, 1938), it is useful to consider classical formulations of the same dynamics in scenarios where a solution of the Dirac equation is numerically unfeasible. The first classical covariant formulation of the Stern-Gerlach force was proposed by Frenkel (1926); it has been compared to the "Foldy-Wouthuysen" model, which is based on the classical limit of the given representation of the Dirac equation (Foldy and Wouthuysen, 1950; Silenko, 2008). The two could be distinguished by measuring the ponderomotive deflection of a spin-polarized electron beam by a tightly focused, ultraintense laser (Wen, Bauke, and Keitel, 2016; Wen, Keitel, and Bauke, 2017).

Finally, we note that the QED emission rates depend on the polarization of the photon as well as the spin of the participating leptons. This is of particular importance in

higher-order QED processes, including cascades, and is discussed in Sec. IV.F. The application of spin- or polarization-dependent emission to the production of polarized particle beams is discussed in Sec. VI.C.

III. NUMERICAL METHODS

Owing to the highly nonlinear and geometrically complex nature of the effects caused by RR and SFQED, theoretical investigations are tightly connected to the development of numerical methods. As these are a key facilitator of this field, we outline the main numerical approaches and some important methodological aspects of their use.

A. Classical radiation emission and reaction

Computing the radiation of moving charges is an important numerical problem, even in the absence of significant radiation-reaction effects. If this is the case, one can just track or calculate one (or several) representative trajectories using any suitable numerical approach. The radiation produced can then be obtained using the numerical integration of the emission integral [Eq. (20)] over the trajectories (Martins *et al.*, 2009). If information about the trajectory is available only at a sequence of time steps, this implies a limit on the highest frequency that can be resolved using the Nyquist-Shannon sampling theorem; this can be overcome by the use of high-order interpolations (Thomas, 2010). The emission integral accounts fully for the interference between radiation emitted from different elements of the trajectory. Considerable speedup is possible if this interference can be neglected and contributions summed according to local synchrotron rates (Martins *et al.*, 2009; Reville and Kirk, 2010; Wallin, Gonoskov, and Marklund, 2015; Martins *et al.*, 2016). In many studies of laser-driven environments, doing this is reasonable because the formation length L_f is much smaller than the laser wavelength; see Figs. 3 and 4.

The interference between the emission of different particles is routinely accounted for in PIC codes via the charge current weighted at the spatial grid nodes. At high intensity, when radiation emission and RR are the strongest, the characteristic frequency ω_c of synchrotron radiation is far from resolved on the grid ($\omega_c \gg \omega_{\mathrm{grid}} = 2\pi c/\Delta$ for grid spacing Δ), and thus it is accounted for separately. This does mean double counting of particles' emission, because the expressions for synchrotron emission account for all frequencies, including those that are resolved. In laser-matter interactions the double counting is negligible because of a vast separation of scales. The characteristic frequency grows with the particle energy (scaling as γ^3), and when RR effects are notable this frequency is much higher than the plasma frequency; see Fig. 17 and Gonoskov *et al.* (2015) for more details.

Within the classical domain, radiation reaction can be accounted for with the incorporation of an additional force on the particle that depends on the instantaneous momentum and the local values of the electromagnetic fields (Tamburini *et al.*, 2010; Sokolov, Naumova, and Nees, 2011; Capdessus, d'Humières, and Tikhonchuk, 2012; Kravets, Noble, and Jaroszynski, 2013; Vranic *et al.*, 2014; Green and Harvey, 2015). Most implementations have focused on the

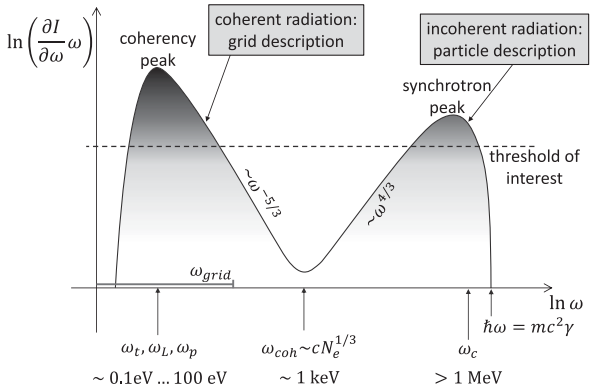

FIG. 17. Schematic representation of the energy spectrum of the electromagnetic field in a high-intensity laser-matter interaction. The frequencies shown (from left to right) are characteristic of the target ($\omega_t = c/L$, with target size L), the laser (ω_L), the plasma density (ω_p), the upper limit of coherent emission processes (ω_{coh}), and incoherent synchrotron emission (ω_c). From Gonoskov *et al.*, 2015.

Landau-Lifshitz equation, which eliminates the pathological solutions of the LAD equation; see Sec. II.A.2. [A numerical solution of the LAD equation via backward integration in time was discussed by Koga (2004).] The dominant term in the LL equation is proportional to γ^2 and corresponds to the synchrotron energy loss rate; other terms involving field derivatives are smaller and, in any case, subleading with respect to spin forces (see Sec. II.D) and quantum corrections (Tamburini *et al.*, 2010). Note that in a PIC simulation, where macroparticles represent many individual particles, the "real" charge and mass must be used to compute the magnitude of the RR force (Vranic, Martins *et al.*, 2016). Contrast this with the Lorentz force, which depends only on the charge-to-mass ratio and therefore may be computed using the macroparticle charge and mass.

The radiation and radiation reaction can be calculated together, self-consistently, in the synchrotron regime: one can determine the total energy emitted in synchrotron radiation within a single time step and deducts this amount from the particle's momentum. This corresponds to the leading term of the LL force and thus gives, to first order, a self-consistent model, which one can implement as an extension of the PIC method; see Kostyukov, Kiselev, and Pukhov (2003) and Rousse *et al.* (2004). It is also possible to extend these calculations to sample the energy and/or angular distribution of local synchrotron radiation with one or several delta-function-like contributions to the resulting distribution (Sun and Wu, 2011; M. Chen *et al.*, 2013; Wallin, Gonoskov, and Marklund, 2015). Note that the use of the Monte Carlo method not only facilitates the computations but also gives one a natural way to account for the probabilistic or stochastic nature of recoils in the quantum domain that we now discuss.

B. QED PIC

When the particle energy and field strength are sufficient such that the quantum parameter $\chi \sim 1$, a classical treatment is insufficient. As discussed in Sec. II.A.3, the total energy loss

is overestimated since a significant part of the emission spectrum exceeds the particle kinetic energy. Correcting the magnitude of the RR force by the Gaunt factor $G_e(\chi_e)$ [Eq. (62)] provides a way to account for this overestimation (Kirk, Bell, and Arka, 2009; Thomas *et al.*, 2012; Blackburn *et al.*, 2014; Yoffe *et al.*, 2015; Zhang, Ridgers, and Thomas, 2015). However, if the typical energy of an emitted photon, whether from the classical or the quantum-corrected spectrum, becomes comparable to the particle kinetic energy, an individual particle can lose a significant part of its energy in a single transition. Since, in many cases of interest, the formation length L_f is much smaller than the laser wavelength (the typical minimal spatial scale of the interaction processes; see Fig. 3), the radiation losses can be viewed as a sequence of instantaneous events that occur with a certain probability.

This concept provides the basis for an extended PIC model that is commonly referred to as QED PIC (Duclous, Kirk, and Bell, 2011; Elkina *et al.*, 2011; Nerush *et al.*, 2011; Ridgers *et al.*, 2014; Arber *et al.*, 2015; Gonoskov *et al.*, 2015; Lobet *et al.*, 2016). The model splits the electromagnetic field into two parts: a coherent classical field sampled at points on a mesh and a population of high-frequency photons that originate from the incoherently summed synchrotron emission of the particles. This is motivated by the separation of energy scales and the consequent negligible role of double counting of the particles' emission (Gonoskov *et al.*, 2015). In the case of significant radiation losses, the energy of incoherent photons ($\hbar\omega \gg 1$ keV) is much larger than that of photons in coherent field-plasma interactions; see Fig. 17. In much the same way that charged particles are treated in ordinary PIC codes, the distribution of high-frequency photons is sampled with an ensemble of so-called macrophotons, which propagate ballistically at the speed of light. A key element for the QED-PIC method is the so-called event generator, which is an algorithm that controls the emission of photons and the creation of electron-positron pairs, according to the locally computed probabilities and characteristics of the QED processes in question. This methodology can be used to account for many SFQED processes, but in many cases a sufficient extension of the PIC model is provided by the inclusion of nonlinear Compton scattering (photon emission) and Breit-Wheeler pair production.

In the simplest case, the event generators for nonlinear Compton scattering and Breit-Wheeler pair production are based on spin- and polarization-averaged rates (as given in Sec. II.B.4) and the assumption that, at high energy, daughter particles are collinear with their parent particles. Radiation reaction is accounted for by subtracting the momentum of the photon from the emitting electron (positron), whereas in pair production the photon is replaced by an electron and a positron.

The event generators decide pseudorandomly when these events occur and how the momentum should be partitioned. Unless using a method that can cope with multiple events in a single time step (see Sec. III.C.1), one has to choose a sufficiently short time step ($\Delta t \ll L_q, L_p$ for all particles and photons), such that the probability of multiple events occurring within a single time step is negligible, i.e., $\Delta t \int_0^1 P'_f(\chi, f')df' \ll 1$, where $P'_f = \partial P/\partial f$ is the differential rate (per unit time) of the relevant process. The maximum time step Δt_{QED} that satisfies this condition is set by the nonlinear Compton rate (Ridgers *et al.*, 2014). It may be compared to the maximum time step permitted by the Courant-Friedrichs-Lewy condition for finite-difference-time-domain methods Δt_{CFL} and the need to resolve the Debye length Δt_{D} as follows (Ridgers *et al.*, 2014):

$$\frac{\Delta t_{\mathrm{QED}}}{\Delta t_{\mathrm{CFL}}} \simeq \frac{10N}{a_0}, \qquad \frac{\Delta t_{\mathrm{QED}}}{\Delta t_{\mathrm{D}}} \simeq \frac{100}{a_0}\sqrt{\frac{n_e mc^2}{n_{\mathrm{cr}} k_B T}}, \tag{67}$$

where N is the number of grid cells used to resolve the laser wavelength, n_e is the electron number density, n_{cr} is the critical density, and T is the plasma temperature.

The generation of photons or particles can be handled in various ways. A method based on cumulative path computation and inverse transform sampling was developed by Duclous, Kirk, and Bell (2011) and Ridgers *et al.* (2014). For a given particle or photon and the corresponding rate $P(t) = \int_0^1 P'_f[\chi(t), f']df'$, the probability of no event happening over the time interval $[t, t+\Delta t]$ decreases as $P(\Delta t) = \exp\left[-\int_t^{t+\Delta t} P(\tau)d\tau\right]$. Using a pseudorandom value from the unit interval $r_1 \in [0,1)$, we can sample an effective path interval between subsequent events $l_e = -\ln(r_1)$ and use it to determine the instant of the next event by requiring that the cumulative integral $\int_t^{t+\Delta t} P(\tau)d\tau \geq l_e$ (one can handle several events within one time step). The momentum fraction f is determined by solving $r_2 = C(f,\chi) = \int_0^f P'_f(\chi, f')df'$, where r_2 is another pseudorandom value from $r_2 \in [0,1]$ and C is the cumulative distribution function. The inverse (quantile) function $C^{-1}(f,\chi)$ can be precalculated and tabulated. For nonlinear Compton scattering, the differential rate $W'_f \to \infty$ as $f \to 0$ as $f^{-2/3}$, which is integrable. A low f cutoff is commonly applied to exclude this region: a cutoff equivalent to $2mc^2$ is sufficiently small to not affect subsequent pair production and does not affect the magnitude of radiation emission too much if γ is sufficiently large. The need for a cutoff can be avoided by augmenting the tabulated values of $C(f,\chi)$ (or its inverse) with the asymptotic analytical expressions (Wallin, Gonoskov, and Marklund, 2015).

One may instead use rejection sampling (Elkina *et al.*, 2011; Nerush *et al.*, 2011), which bypasses the need to calculate the cumulative distribution function. One uniformly distributed random value $r_1 \in [0,1]$ defines the candidate value of f, and another $r_2 \in [0,1]$ defines whether this event happens; the event is accepted if $r_2 < N'_f = \Delta t P'_f(\chi, r_1)$. This procedure requires that $N'_f < 1$ for all values of $f \in [0,1]$ and for all possible values of χ. Choosing a sufficiently short time step can ensure this for the Breit-Wheeler process. However, the infrared divergence for nonlinear Compton scattering means that this will be violated for some vicinity of $f = 0$. This sets an effective cutoff and, moreover, imposes an additional time step restriction. Both problems can be eliminated [following Gonoskov *et al.* (2015)]. For the former, the candidate f can be generated as $f = r_1^3$ (i.e., with small values) more often, such that the corresponding acceptance probability $3r_1^2 P'_f(\chi, r_1^3)$ becomes bounded from above. With

this modification, the restriction on the time step can be estimated and used to subdivide the time step; see Sec. III.C.1.

More advanced treatment of nonlinear Compton scattering can include the angular dependence of the emission spectrum (Sun and Wu, 2011; Blackburn, Seipt *et al.*, 2020), as well as the spin and polarization properties; see Sec. II.D.

C. Advanced components

1. Subcycling

The growth of the nonlinear Compton rate at high intensity means that it becomes the most important limiting factor on the time step. Subcycling, i.e., dividing the global time step into smaller fractions and testing for emission at each stage, is an efficient means of scaling simulations of photon emission (Volokitin *et al.*, 2020). This assumes that the EM field is approximately constant over a single time step, which is a generic requirement for a simulation to be appropriately resolved. Note that subcycling permits a single particle or photon to cause the cascaded generation of many new particles (if χ is large) in the course of a single global time step. Subcycling can also ensure an accurate prediction of particle trajectories in strong fields (Arefiev *et al.*, 2015; Tangtartharakul, Chen, and Arefiev, 2021).

2. Resampling

In QED-PIC codes particle and photon distributions are sampled using an ensemble of so-called macroparticles, each having a weight that quantifies the number of real particles or photons that it represents. In general, macroparticles created by QED processes inherit the weight of their parent macroparticle. (The distinction between macroparticles and macrophotons is not important here, and therefore we use the former term only.) The prolific generation of new particles in, for example, an electromagnetic cascade (see Sec. IV.F) can significantly increase the computational demands of running a simulation. Managing this growing demand requires a procedure that repeatedly decreases the number of macroparticles while increasing the weight of individual macroparticles accordingly. This is referred to as ensemble *resampling* or *downsampling*. Two main approaches are used: *merging* (coalescing), in which closely placed macroparticles are collapsed, and *thinning*, in which some macroparticles are deleted while others have their weight increased.

Preserving conserved quantities (energy, momentum, and charge) and macroparticles' contributions to grid quantities (weighted charge and current density) is recognized as an important issue in the development of resampling algorithms, as small errors can accumulate over the growth of a cascade. The thinning procedure can be realized by removing randomly selected macroparticles and redistributing their weight uniformly among others of the same kind (Timokhin, 2010); one can redistribute their energy as well (Nerush *et al.*, 2011). A method of coalescing two macroparticles while preserving their contributions to the charge density at grid nodes was proposed by Lapenta and Brackbill (1994). Preservation of the energy and momentum of a merged subset of macroparticles can be accomplished by replacing the subset with a pair of macroparticles with appropriately chosen momenta

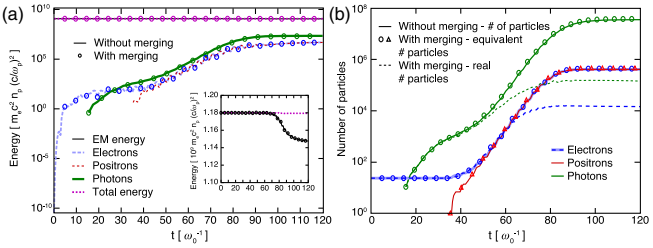

FIG. 18. Particle merging in a simulation of a laser-driven QED cascade indicating energy conservation and growth in the number of particles over the course of the simulation. Adapted from Vranic *et al.*, 2015.

(Rjasanow and Wagner, 1996; Rjasanow, Schreiber, and Wagner, 1998; Vranic *et al.*, 2015). The application of the latter to simulations of a QED cascade is shown in Fig. 18, where good agreement is found for the evolution of the energy and the number of particles between the merging and no-merging simulations. The approach of replacing local subsets with smaller subsets with improved uniformity and conservation properties was developed by Lapenta and Brackbill (1995), Assous, Pougeard Dulimbert, and Segré (2003), Welch *et al.* (2007), Pfeiffer *et al.* (2015), and Faghihi *et al.* (2020).

Even if the procedure is not completely conservative, errors can be reduced by applying the merging procedure only to subsets of macroparticles that are close in coordinate and momentum space (Rjasanow and Wagner, 1996; Rjasanow, Schreiber, and Wagner, 1998). These clusters can be obtained by octree binning (Martin and Cambier, 2016), with a Voronoi algorithm (Luu, Tückmantel, and Pukhov, 2016), or by identifying highly populated cells in coordinate-momentum space (Vranic *et al.*, 2015; Chang *et al.*, 2017). Choosing the size of cells or clusters in coordinate-momentum space to be merged involves a trade-off: small sizes mean a high-density threshold to trigger merging, whereas large sizes may flatten out small-scale features (abrupt changes, peaks, etc.) that could be of importance. In the latter case, the problem is caused by adding new macroparticles and assuming a uniform (or smoothed-out) distribution of real particles across the cell or cluster.

One can avoid this by probabilistically choosing one of the several possible weight modifications such that the weight of each macroparticle remains unchanged on average (while accounting for probabilities of the modifications); in each modification one or more macroparticles are assigned with zero weight and are therefore removed (Muraviev, Bashinov, Efimenko, Volokitin *et al.*, 2021; Gonoskov, 2022). This thinning approach, referred to as *agnostic* resampling, preserves all the distribution functions (coordinate, momentum, angular, etc.) of particles on average, and thus does not require any prior knowledge about the scales of features in these distributions. In addition, an agnostic resampling algorithm that provides a way to preserve conservation laws, contributions to grid values, and central moments of particle distribution across the cellor cluster was proposed by Gonoskov (2022). The efficiency of agnostic resampling was demonstrated by Muraviev, Bashinov, Efimenko, Volokitin *et al.* (2021), where several algorithms for agnostic resampling have

been compared to two merging algorithms. The study showed that reducing the variance of weight values across the ensemble (provided by some versions of agnostic resampling) can further increase performance (as characterized by the smallness of numerical errors for a given number of macroparticles used).

IV. CHARGED PARTICLE DYNAMICS

While the effect of RR on particle dynamics has been studied theoretically for decades, the development of large-scale numerical simulations has revealed complex new dynamics that arise in strong-field environments from the competition between acceleration (by the action of the external EM field) and deceleration (by RR). In this section we classify and review different types of RR-dominated motion that include dissipation (Sec. IV.B), nondeterminism (Sec. IV.C), trapping (Sec. IV.D), chaos (Sec. IV.E), cascades (Sec. IV.F), and depletion (Sec. IV.G). How these effects could be leveraged upon the creation of new radiation and particles sources is discussed in Sec. VI. We begin with an overview of the interaction geometries that characterize laser-matter interactions.

A. Interaction geometries

We now consider the interaction of a single electron with a plane electromagnetic wave in terms of the parameter χ_e in order to demonstrate the importance of the interaction geometry. The first general question for many applications involves the energy coupling, i.e., the conversion of the electromagnetic energy of the laser pulse into the kinetic energy of particles. Although the collective effects are central to this question, it is instructive to start by considering the acceleration and deceleration of an individual electron in plane waves.

Two principal interaction schemes can be used to categorize charged particle behavior in strong EM waves. The particle motion is dominated by either transverse or longitudinal motion (defined with respect to the laser propagation axis), with the characteristic Lorentz factors $\gamma \sim a_0$ or $\gamma \gg a_0$, respectively; see Figs. 19(a) and 19(b). In both cases, the electron's radiation losses manifest themselves as a strong decelerating force. While this loss completely dominates the particle motion in the longitudinal case, in the transverse case the particle is continuously reaccelerated such that it can reach a kind of equilibrium. Thus, in the longitudinal case the field serves as a target only, whereas in the transverse case it is not only a target but also an accelerator.

We now characterize these two schemes from the point of view of the parameter χ_e. For an electron propagating at an angle θ_κ to a plane EM wave with a wave vector κ,

$$\chi_e = \gamma \frac{E_0}{E_{\rm cr}}(1 - \beta \cos\theta_\kappa), \tag{68}$$

where $E_0/E_{\rm cr} \simeq 2.1 \times 10^{-4} I_0^{1/2} [10^{22}\ \mathrm{W\,cm^{-2}}]$ for peak intensity I_0, assuming circular polarization (CP). Thus, the parameter χ_e is maximized for $\theta_k = \pi$, i.e., when an electron collides

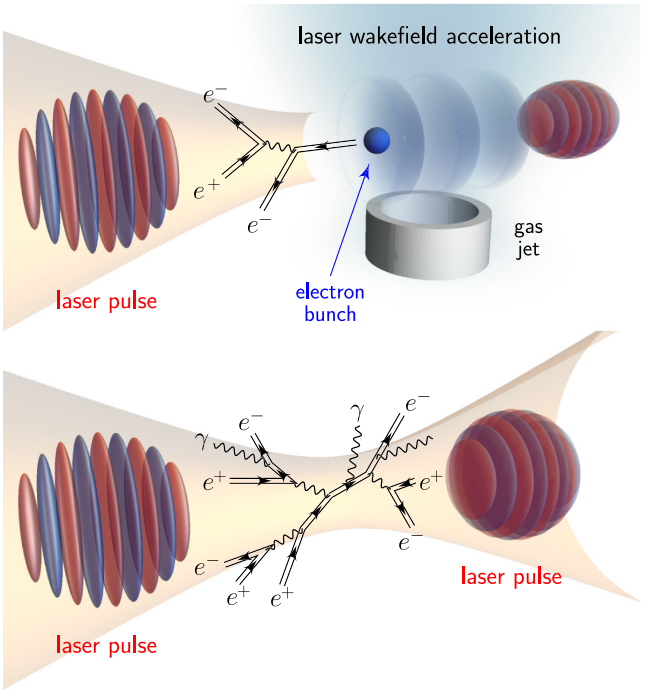

FIG. 19. Principal experimental schemes aimed at the study of nonlinear QED. Upper panel: laser–electron-beam interactions (all-optical setup). Lower panel: colliding laser pulses. Adapted from Bulanov *et al.*, 2012.

head on with the EM wave.[4] For an electron propagating in a pure electric field $E_0\mathbf{e}$ at an angle θ_e to the field vector $\mathbf{e}$,

$$\chi_e = \gamma \frac{E_0}{E_{\rm cr}} \sqrt{1 - \beta^2 \cos^2\theta_e}. \tag{69}$$

The parameter χ_e is maximized when the electron momentum is perpendicular to the electric field. This can be realized at the magnetic nodes of a standing wave formed by counterpropagating pulses with parallel linear polarization.

We now discuss the threshold intensities when electron motion is dominated by classical radiation-reaction or quantum effects for these two schemes of interaction. To do so, it is useful to introduce the dimensionless parameter

$$\varepsilon_{\rm rad} = \frac{4\pi r_e}{3\lambda} = \frac{2\alpha}{3}\frac{\hbar\omega_0}{mc^2}, \tag{70}$$

which appears when one compares the magnitude of the Lorentz and RR forces (Bulanov *et al.*, 2004).

Laser-electron beam.—The electron-laser collision geometry is characterized by the electron maintaining the longitudinal type of motion over the entire course of interaction (despite the radiation losses). Such a motion permits analytical calculations in both quantum [see Eq. (75)] and classical

[4]We note that $\chi_\gamma = (\hbar\omega/mc^2)(E_0/E_{\rm cr})(1 - \cos\theta_\kappa)$ is also maximized at $\theta_\kappa = \pi$. In the case of copropagation, $\theta_\kappa = 0$, $\chi_e \sim 1/\gamma$, and $\chi_\gamma = 0$. The last result is due to the vanishing of the terms corresponding to photon-photon scattering in the EM-field Lagrangian.

cases. The related experimental scheme is shown for a head-on collision as the green lines in Fig. 3.

We may define the threshold for the radiation-reaction effects to be significant as follows by requiring that the electron lose half of its energy after the interaction (Bulanov *et al.*, 2012)[5]:

$$a_0 > a_0^{\mathrm{crr}} = (\varepsilon_{\mathrm{rad}}\omega_0\tau_L\gamma_0)^{-1/2} \simeq 24\lambda^{1/2}[\mu\mathrm{m}]/N^{1/2}, \quad (71)$$

where γ_0 is the initial Lorentz factor, $\tau_L = N\lambda/c$ is the laser pulse duration, N is the equivalent number of cycles, and λ is the wavelength. For a 10-GeV electron beam colliding with a 10-cycle laser pulse ($\lambda = 0.8$ μm), the radiation-reaction limit is $a_0^{\mathrm{crr}} \approx 7$ and the corresponding peak intensity is $I_{\mathrm{crr}} \approx 2 \times 10^{20}$ W/cm^2.

The threshold for quantum effects is reached when a single photon of the emitted radiation has energy comparable to that of the electron. The characteristic photon energy in the case of laser-electron collision is $\hbar\omega_m \approx \hbar\omega a_0\gamma_e^2$, which corresponds to the condition $\chi_e \sim 1$. Thus, the threshold for quantum effects is reached when (Bulanov *et al.*, 2012)

$$a_0 > a_0^{\mathrm{qrr}} = \frac{2\alpha}{3\varepsilon_{\mathrm{rad}}\gamma_0} \simeq 21\lambda[\mu\mathrm{m}]. \quad (72)$$

For a 10-GeV electron beam colliding with a 0.8 μm laser pulse, the quantum limit is $a_0^{\mathrm{qrr}} = 17$ and the corresponding intensity is $I_{\mathrm{qrr}} = 8 \times 10^{20}$ W/cm^2. Note that the hierarchy $a_0^{\mathrm{qrr}} > a_0^{\mathrm{crr}}$ is reversed if $\lambda < 0.16$ μm.

Colliding lasers.—Here two counterpropagating laser beams are used to form an electromagnetic standing wave. Several types of standing waves are possible depending on the polarization of beams (see Sec. IV.D), and the setup can be extended to more than two beams, as well as to include a target or self-generated cascade (see Sec. V.E.3). Nevertheless, characteristic thresholds can be obtained from considering the case of two counterpropagating CP beams that form a standing wave with electric- and magnetic-field vectors that rotate in the transverse plane. This case permits analytical calculations under both classical and quantum treatment of radiation reaction. At the electric-field antinode the electron orbits with a large Lorentz factor as in the single-pulse case, but without the longitudinal drift. A qualitatively similar scenario is expected in the interaction of a single laser pulse with an overdense plasma due to reflection of the laser from the critical surface (Bell and Kirk, 2008); see Kostyukov and Nerush (2016).

The threshold for the dynamics to be dominated by radiation reaction is given by the a_0 quantity at which the energy loss to radiation is balanced by the energy gain from the electric field. The energy loss is given by $d\mathcal{E}/dt|_{\mathrm{rad}} = \varepsilon_{\mathrm{rad}}\omega_0\gamma^2 p_\perp^2/m$. The rate of energy gain from the external field is $d\mathcal{E}/dt|_{\mathrm{ext}} \simeq \omega_0 mc^2 a_0$ when RR effects are neglected. Equating the two and setting $\gamma \simeq p_\perp/mc = a_0$, we find that the classical radiation-dominated regime is reached for (Bulanov *et al.*, 2011)

$$a_0 > a_0^{\mathrm{crr}} = \varepsilon_{\mathrm{rad}}^{-1/3} \simeq 4.4 \times 10^2\lambda^{-1/3}[\mu\mathrm{m}]. \quad (73)$$

The threshold for quantum effects is when a single photon of the emitted radiation has energy comparable to the electron, i.e., $\chi_e \simeq 1$. For optical wavelengths, the radiation-dominated regime is reached before the quantum regime (see Fig. 4) at an amplitude of (Bulanov *et al.*, 2011)

$$a_0 > a_0^{\mathrm{qrr}} = \frac{4\alpha^2}{9\varepsilon_{\mathrm{rad}}} \simeq 2.0 \times 10^3\lambda[\mu\mathrm{m}]. \quad (74)$$

The hierarchy of $a_0^{\mathrm{qrr}} > a_0^{\mathrm{crr}}$ is reversed if $\lambda \lesssim 0.3$ μm. Shorter wavelengths therefore provide an opportunity to enter the quantum regime before large-scale radiation losses are expected; see Fig. 4. For an electron moving in the focus of two 0.8-μm laser pulses, a_0^{crr} corresponds to an intensity of 3.5×10^{23} W cm^{-2}, and a_0^{qrr} corresponds to an intensity of 5.5×10^{24} W cm^{-2}. Above the latter intensity, it is important to note that the QED radiation power scales as $\chi_e^{2/3}$ rather than χ_e^2.

B. Energy exchange

From the theoretical considerations discussed in Secs. II.A and II.C, one might expect RR to manifest itself primarily as dissipation, i.e., energy loss. However, the strength of RR effects depends on the strength and orientation of the external, accelerating electric and magnetic fields. The interplay between the Lorentz and RR forces can lead to either deceleration or acceleration of the charged particles, depending on the field geometry.

Consider the interaction of an electron with a pulsed plane EM wave. In this scenario the LL equation (19) may be solved analytically (Di Piazza, 2008). Let the electric-field components in the x and y directions be $E_0 f_1'(\phi)$ and $E_0 f_2'(\phi)$, respectively, where $E_0 = a_0 mc\omega_0/e$ and $f_{1,2}(\phi)$ are arbitrary functions of phase ϕ and the primes denote differentiation with respect to phase. The light-front momentum of the electron $p^- = \gamma mc - p_z$ (assuming that the laser propagates toward positive z) as a function of phase is (Di Piazza, 2008; Harvey *et al.*, 2011)

$$p^-(\phi) = \frac{p_0^-}{1 + \varepsilon_{\mathrm{rad}} a_0^2 p_0^- I(\phi)/mc},$$
$$I(\phi) = \int_{-\infty}^{\phi} [f_1'(\psi)^2 + f_2'(\psi)^2]d\psi. \quad (75)$$

The light-front momentum always decreases under RR (it would be constant under the Lorentz force alone). Whether the energy decreases or increases, however, depends on its initial value. If γ is initially large, then $p^- \simeq 2\gamma mc$ and RR manifests itself as an energy loss: measuring this energy loss, whether in the classical or quantum regimes, is an object of experimental investigation; see Sec. V. If the charge is initially at rest, however, then it is accelerated to an asymptotic Lorentz factor

[5]We note that there are other definitions of this threshold in the literature. For example, Thomas *et al.* (2012) defined it as a loss of 10% of the electron energy per laser wavelength.

of $\gamma' \simeq 1 + \varepsilon_{\rm rad} a_0^2 I(\phi)$. In fact, there is a net energy transfer from the wave of (Di Piazza, 2018)

$$\Delta\mathcal{E} = \frac{mc^2 \varepsilon_{\rm rad} a_0^4}{2} \times \int_{-\infty}^{\infty} [f_1'(\phi)^2 + f_2'(\phi)^2] \left[f_1(\phi)^2 + f_2(\phi)^2 + \frac{2}{a_0^2} \right] d\phi. \tag{76}$$

In the absence of RR, this would be zero, in accordance with the Lawson-Woodward theorem (Palmer, 1995).

One can qualitatively understand the origin of this energy gain in the following way (Zel'Dovich, 1975): in the interaction with the laser, the electron absorbs photons that carry energy $\hbar\omega$ and momentum $\hbar\omega/c$ along the direction of the pulse propagation (ω is the frequency of one of the photons). This means that the electron receives the maximum possible longitudinal momentum $\Delta\mathcal{E}/c$ per unit of absorbed energy $\Delta\mathcal{E}$. However, an electron cannot absorb photons without emission by energy-momentum conservation. If the electron were to emit photons only along the longitudinal direction, there would be no accumulation of momentum. However, the emission is not restricted to this direction; thus, the energy loss is $\Delta\mathcal{E}$ but the loss of longitudinal momentum is $\Delta\mathcal{E}/c \cos\theta < \Delta\mathcal{E}/c$ (where θ is the emission angle). As a consequence, the electron will have nonzero longitudinal momentum after it is overtaken by the pulse.

Thus, RR plays a significant role in altering the energy coupling between fields and particles. This has dramatic consequences in field configurations in which more work can be done, such as standing waves. To gain insight into energy coupling in the laser-laser geometry, we consider two indicative cases theoretically: the rotating and oscillating electric fields.

We start with the rotating electric field. Under the classical treatment of RR, one finds that the electron performs circular orbits, with the constant Lorentz factor γ given by the root of the following equation (Zel'Dovich, 1975; Bulanov, Esirkepov *et al.*, 2011):

$$a_0^2 = (\gamma^2 - 1)(1 + \varepsilon_{\rm rad}\gamma^6). \tag{77}$$

Thus, the Lorentz and RR forces are in balance and the energy transferred from field to particle is seamlessly lost as radiation.[6] Equation (77) has limits $\gamma \simeq a_0$ if $a_0 \ll a_0^{\rm crr}$ and $\gamma \simeq (a_0/\varepsilon_{\rm rad})^{1/4}$ if $a_0 \gg a_0^{\rm crr}$, where $a_0^{\rm crr}$ is given by Eq. (73). The weakened scaling at high intensity is caused by radiation losses, which decrease the angle between the instantaneous momentum and the electric-field vector:

$$\tan\varphi = \frac{1}{\varepsilon_{\rm rad}\gamma^3}. \tag{78}$$

The quantum parameter χ_e goes from $a_0^2/a_{\rm cr}$ at $a_0 \ll a_0^{\rm crr}$ to $(3/2\alpha)^{1/2} a_0^{1/2} a_{\rm cr}^{-1/2}$ at $a_0 \gg a_0^{\rm crr}$; see Bulanov *et al.* (2011), Bulanov, Esirkepov *et al.* (2011), Chang *et al.* (2015), Kostyukov and Nerush (2016), and Bashinov, Kumar, and Kim (2017). Thus, classical radiation losses delay the onset of the quantum regime (Popruzhenko, Liseykina, and Macchi, 2019). A consequence of Eq. (78) is that, at large a_0, the electron motion is parallel to the electric field, and therefore optimized to absorb incident radiation (Zhang, Ridgers, and Thomas, 2015). Note that orbits at the magnetic node are unstable: charged particles will tend to migrate toward the electric nodes, where the magnetic field is strongest (Bashinov, Kumar, and Kim, 2017); see Sec. IV.D. In the limit of $\chi \gg 1$, quantum corrections alter the scaling of radiation losses from $\sim\chi^2$ to $\sim\chi^{2/3}$, which changes the trends to $\gamma \approx 84 a_{\rm cr}^{-1/4} a_0^{3/4}$, $\chi_e \approx 7.1 \times 10^3 a_{\rm cr}^{-3/2} a_0^{3/2}$, and $\varphi \approx 84 a_{\rm cr}^{-1/4} a_0^{-1/4}$; see Chang *et al.* (2015), Kostyukov and Nerush (2016), and Bashinov, Kumar, and Kim (2017).

The second indicative case is the linearly polarized (LP) standing wave. This wave has the property that the electric field at the magnetic node oscillates in magnitude, but not direction. As the electron is driven parallel to $\mathbf{E}$, radiation losses are suppressed and the energy can reach the characteristic quiver value of $\gamma = a_0$. Reduced production of high-energy photons and the consequent suppression of cascade development (see Sec. IV.F) means that this configuration has been proposed as a means to generate critically strong electromagnetic fields (Bulanov, Esirkepov *et al.*, 2010). The dynamics are, however, more complicated due to migration around this node. While it might be expected to be unstable, as in the CP case, there is the surprising result that, in the radiation-dominated regime (Bulanov *et al.*, 2004), electrons can become trapped here (Gonoskov *et al.*, 2014). We discuss this "anomalous" trapping in Sec. IV.D.

From the two previous cases, we see that energy exchange has different scalings for CP ($\gamma \sim a_0^{3/4}$) and LP ($\gamma \sim a_0$) standing waves. To understand this observation, we turn to the discussion of the RR's generic influence on the dynamics of charges. Consider that, for ultrarelativistic particles, the magnitude of radiation losses is determined by the magnitude of the transverse acceleration. In a general electromagnetic field with electric and magnetic components $\mathbf{E}$ and $\mathbf{B}$, there is always one unit direction for which the transverse acceleration vanishes (Gonoskov and Marklund, 2018),

$$\mathbf{n}_{\rm RFD}^{\pm} = \frac{\sqrt{u(1-u)}(\mathbf{E}\times\mathbf{B}) \pm [(1-u)B\mathbf{E} + u(\mathbf{E}\cdot\mathbf{B})\hat{\mathbf{B}}]}{[E^2B^2 - u(\mathbf{E}\times\mathbf{B})^2]^{1/2}}, \tag{79}$$

where

$$u = \frac{2c^2B^2}{E^2 + c^2B^2} \frac{1 - \sqrt{1-w}}{w}, \qquad w = \frac{4(\mathbf{E}\times c\mathbf{B})^2}{(E^2 + c^2B^2)^2}. \tag{80}$$

In Eqs. (79) and (80) superscripts denote the sign of the charge. This vector is called the *radiation-free direction* (RFD) since radiation is suppressed when the particle has momentum parallel to $\mathbf{n}_{\rm RFD}$. If this is not the case, momentum in any other direction is rapidly exhausted by radiation emission; reacceleration by the external field then brings

[6] Analytical solutions are also available for the case of a rotating electric field, which has a static magnetic field superimposed along its axis of rotation (Nakamura, 2020).

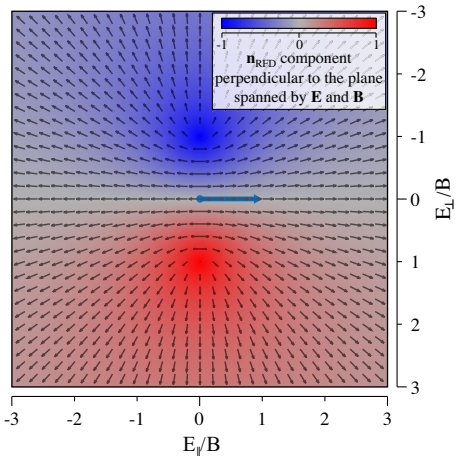

FIG. 20. Radiation-free direction $\mathbf{n}^{+}_{\mathrm{RFD}}$, as a function of the end point of the electric-field vector $\mathbf{E}$, given a fixed magnetic-field vector $\mathbf{B}$ (blue arrow). Arrows denote the projection of $\mathbf{n}^{+}_{\mathrm{RFD}}$ onto the plane spanned by $\mathbf{E}$ and $\mathbf{B}$, and the color scale shows the projection on $\mathbf{B}\times\mathbf{E}$: values are negative (positive) in the upper (lower) half. From Gonoskov and Marklund, 2018.

the particle momentum toward the RFD, which is the only stable point (Gonoskov and Marklund, 2018). Figure 20 shows that $\mathbf{E}$ has a nonzero projection on the RFD, making it the only stable attractive point, in all cases except $\mathbf{E}\cdot\mathbf{B}=0$ and $E<cB$. Samsonov, Nerush, and Kostyukov (2018) analyzed particle dynamics in the strong-radiation-damping regime and found that the velocity is indeed determined by the local and instant EM field. This causes trajectories to be periodic in a wide variety of oscillating EM fields. It was also shown that the angle between the RFD and the Poynting vector is always less than $\pi/2$, leading to particles being attracted to regions of EM-field absorption (Samsonov, Nerush, and Kostyukov, 2018). The tendency of charges to align the motion along the local RFD has been demonstrated in exact analytical solutions for longitudinal and transverse waves (Ekman, Heinzl, and Ilderton, 2021a): both cases are special in the context of the previously given arguments.

The tendency to the RFD makes it clear that the rotating and oscillating electric fields represent limiting cases. In the former, the particles are constantly chasing the RFD, which points along the electric-field vector (see Fig. 20), while the deviation angle [Eq. (78)] remains relatively large. This facilitates energy loss to radiation and leads to a weaker energy scaling $\gamma\sim a_0^{3/4}$ (at $\chi\gg 1$). In the latter, the RFD flips direction twice per wave period so that charges can quickly adjust their motion to move predominantly along the RFD. This minimizes energy loss, so the energy scaling is stronger ($\gamma\sim a_0$). As these represent the worst- and best-case scenarios, we may conclude that the energy coupling for various types of particle dynamics in the laser-laser geometry is likely to be found between these two limiting cases. This is highlighted by the shaded red region in Fig. 3.

In both the classical and quantum regimes, the magnitude of radiation reaction is controlled by the transverse acceleration. While the dynamics are therefore qualitatively similar, the stochastic, discrete nature of losses in the latter leads to unique dynamics that we describe in Sec. IV.C.

C. Stochasticity, straggling, and quenching

In the quantum regime ($\chi\gtrsim 1$), the typical energy of the emitted photons is comparable to the kinetic energy of the emitting electrons and positrons. As the photon formation length is much shorter than the characteristic timescale of the particles dynamics (see Fig. 3) for $a_0\gg 1$, RR in the quantum regime can be viewed as a sequence of discrete, instantaneous recoils that occur along the particle trajectory at probabilistically determined intervals. This has effects on particle motion not captured by a classical treatment, in which RR manifests itself as a continuous force.

As discussed in Sec. II.C, the probabilistic change of momentum can be described as a stochastic force that can be treated with the Fokker-Planck equation: the drift term describes the rate of radiation losses, whereas the diffusion term describes the discreetness and probabilistic nature of the losses. The energy loss rate increases with the energy of particles and therefore, on average, the most energetic particles lose energy more quickly than others. This causes contraction of the particle phase space (Tamburini *et al.*, 2011; Yoffe *et al.*, 2015, 2016) and, in particular, to a shrinking of the energy distribution when an electron beam passes through an intense laser pulse. However, the diffusion term, which governs stochastic broadening, can dominate for sufficiently high values of χ. This dominance has been analyzed and numerically demonstrated for the case of a beam of a 1-GeV electron passing through a 10-cycle laser pulse of peak intensity 2×10^{22} W/cm^2 (yielding $\chi=0.8$) (Neitz and Di Piazza, 2013). The change of the energy variance can already be used as a direct measure of the quantum stochasticity of RR at intensities of 10^{21} W/cm^2 (Ridgers *et al.*, 2017). If the electrons continue losing energy for a sufficiently long time, their reduced energies start to yield lower values of χ and the broadening term no longer dominates. The maximum energy width can be calculated for the given initial beam parameters (Vranic, Grismayer *et al.*, 2016). The analysis of this transition and of the applicability of the Fokker-Plank approach, the classical RR treatment, and the discrete, stochastic treatment was carried out by Niel *et al.* (2018). In other field geometries, such as linearly polarized standing waves, the Markov chain formalism can be applied to analyze when and how the classical contraction of phase-space volume breaks down due to the onset of quantum stochasticity (Bashinov, Kim, and Sergeev, 2015).

Another notable consequence of the probabilistic nature of RR is the following possibility, for an electron entering a strong-field region that ramps up over a finite duration (or length). Instead of losing its kinetic energy continuously, as would classically occur, there is a chance that electrons will penetrate the strong-field region without having radiated. The quantum parameter of such electrons is therefore larger than expected, and subsequently there is a greater probability of emitting high-energy photons. This effect, referred to as *straggling* (Shen and White, 1972), causes a significant enhancement of the emission of sub-GeV photons by GeV electrons interacting with a laser pulse having an intensity of $\sim 10^{22}$ W/cm^2 (Blackburn *et al.*, 2014). In addition, straggling particles, which have higher energy, are less susceptible

to deflection by gradients in the laser fields. This can result in the narrowing of the emission angle (Harvey *et al.*, 2016).

In more general terms, the straggling effect implies the appearance of electrons in regions of phase space that are not accessible for trajectories governed by continuous RR forces (in either classical LL or quantum-corrected form). This can be used to enhance the production of pairs in various field configurations (Duclous, Kirk, and Bell, 2011), or to distinguish classical from quantum RR (Geng *et al.*, 2019).

In extremis, an energetic electron can pass through a strong-field region without having radiated even a single photon. This effect, referred to as quantum *quenching* of radiation losses, can be observable at intensities $\sim 10^{22}$ W/cm^2 with 10-cycle pulses (a small percentage penetrate) and becomes crucial with sub-2-cycle pulses ($> 30\%$ penetrate) (Harvey *et al.*, 2017). This suggests that highly compressed laser radiation can deflect energetic particles without synchrotron radiation emission, an otherwise inevitable loss mechanism.

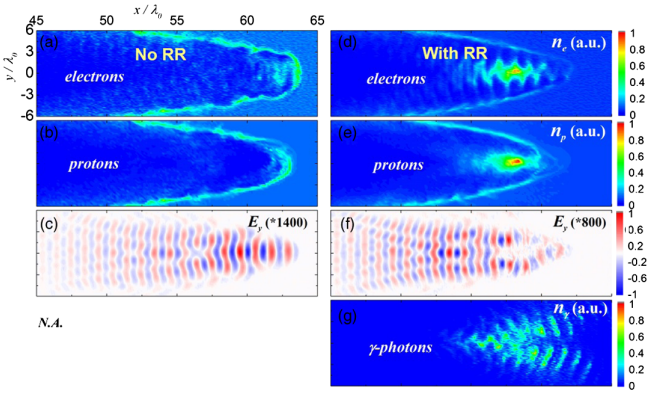

FIG. 21. Radiation-reaction trapping in simulations of laser-wakefield acceleration. Shown are the densities of (a),(d) the electrons, (b),(e) the protons, and (g) the γ photons, as well as (c),(f) the transverse component of the electric field obtained using 3D PIC simulations with (right column) and without (left column) radiation reaction. From Ji *et al.*, 2014.

D. Particle trapping

Unlike frictional losses due to viscosity, the energy dissipation caused by RR is critically dependent on the local orientation of the electric and magnetic fields. The strong directional dependence of RR can manifest itself in particle trapping, which we discuss in terms of two main electromagnetic field configurations: traveling and standing waves.

Even in the absence of RR, relativistic effects can cause particles to be "trapped" within traveling electromagnetic waves. Consider the dynamics of an electron that starts at rest. If the wave has an amplitude $a_0 \gtrsim 1$, the electric field causes relativistic motion of an electron in the transverse direction, while the magnetic field converts this oscillation into a secular longitudinal drift. The particle is generally carried in the direction of the wave propagation. The higher the amplitude of the pulse, the closer the longitudinal velocity gets to the speed of light and the longer that the electron copropagates with the pulse.

This can be enhanced by the effect of RR. *RR-induced trapping* is observed in the simulations of laser-wakefield acceleration (LWFA) (Ji *et al.*, 2014). In the considered "bubble" regime of LWFA, an intense laser pulse propagates through a low-density plasma, displacing the plasma electrons and creating a region of uncompensated positive charge: the charge-separation electric field within this bubble then accelerates a trailing population of electrons (Esarey, Schroeder, and Leemans, 2009). The displacement of plasma electrons is caused by the ponderomotive force of the laser (Gaponov and Miller, 1958; Quesnel and Mora, 1998), which itself arises from the transverse gradient in intensity of the focused laser pulse. By comparing simulations with and without radiation losses, as shown in Fig. 21, one observes a distinct difference: in the former case, a population of electrons is trapped inside the laser pulse and copropagates with it over a long distance. Simulations show that for a laser pulse with peak intensity of 4×10^{24} W cm^{-2}, a population with a charge greater than 1 nC can be carried over a few hundred micrometers (Wallin *et al.*, 2017).

To explain these observations, we note that the RR force is directed antiparallel to the electron's motion in the ultrarelativistic regime. It does not therefore deflect the electron directly; it does, however, reduce the electron γ such that the deflection by the laser fields, i.e., the Lorentz force, is enhanced. One may view such a situation as a manifestation of the electron's tendency to align itself with the local RFD, which points along the laser propagation axis in this case; see Eq. (79).

It is natural to ask whether a trapped electron can gain energy while comoving with the laser pulse. In the absence of RR, the oscillatory nature of the fields in an EM wave means that periods of acceleration and deceleration follow each other in sequence, almost compensating for each other (up to a longitudinal drift). While this would normally preclude a net gain of energy, it can be overcome in particular field configurations. One possible idea is to deflect the electron out of the strong-field region during the deceleration phase and then return it in time for the next acceleration phase. This can be realized by laser propagation in a dense plasma channel, where a self-generated, azimuthal magnetic field provides suitable deflection. In this case RR is essential in facilitating the coalescence of electrons around the laser propagation axis and their optimal phasing, leading to enhanced, directed radiation emission and an acceleration of electrons (Zhu *et al.*, 2015, 2016; Stark, Toncian, and Arefiev, 2016; Vranic, Fonseca, and Silva, 2018; Gong *et al.*, 2019).

A standing EM wave can be realized in a variety of ways, from the collision of two counterpropagating laser pulses to the creation of a dipole wave (Gonoskov *et al.*, 2012). We begin with the case of a standing wave formed by two linearly polarized lasers that have parallel electric-field vectors. The electron dynamics depend crucially on the field amplitude a_0. Consider the evolution of the density distribution of a population of electrons that are initially uniformly distributed along the collision axis. After a transient phase that lasts for several laser periods, the distribution stabilizes (for a certain phase). The final configuration is shown as a function of a_0 in Fig. 22.

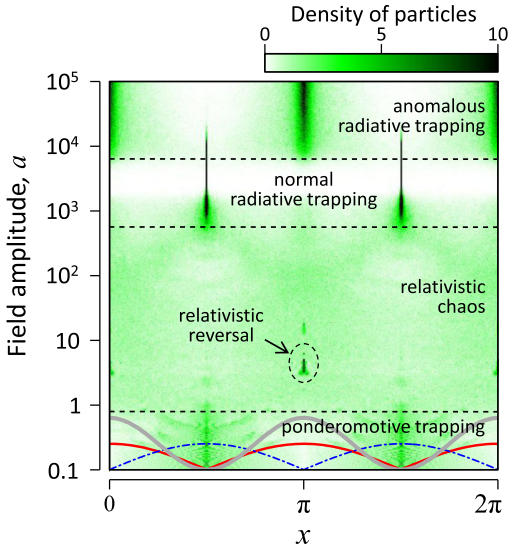

FIG. 22. Electron number density as a function of the wave amplitude (here called $a = a_0$) in a linearly polarized, standing electromagnetic wave. As a increases, the ponderomotive, normal, and anomalous radiative trapping regimes are accessed. The curves in the lower region indicate the ponderomotive potential (thick gray line), as well as the electric (thin red line) and magnetic (dot-dashed blue line) field amplitudes, in arbitrary units. From Gonoskov *et al.*, 2014.

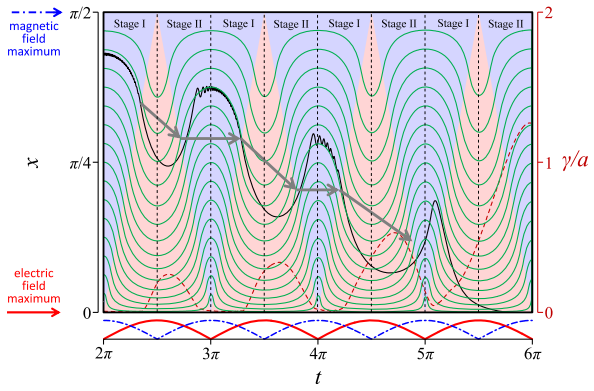

FIG. 23. Explanation of ART through the net migration of electrons toward electric-field maxima. The particle trajectory (black curve, axis to the left), its gamma factor (red dashed curve, axis to the right), and asymptotic trajectories (thin green curves) are shown together with the regions of electric-field (red) and magnetic-field (blue) dominance (see details in the text). From Gonoskov *et al.*, 2014.

For nonrelativistic amplitudes ($a_0 < 1$), the electrons are trapped around minima in the laser's ponderomotive potential, which are located at the electric-field nodes (Gaponov and Miller, 1958). In the range $1 < a \lesssim 500$, where radiation losses are not sufficiently large to affect particle dynamics significantly, the dynamics are stochastic (Bauer, Mulser, and Steeb, 1995; Lehmann and Spatschek, 2012) and, with the exception of relativistic reversal (Kaplan and Pokrovsky, 2005; Dodin and Fisch, 2008), trapping effects are not evident.

Once $a_0 \gtrsim 500$, RR induces two kinds of trapping phenomena. The first manifests itself as the localization of electrons in the vicinity of electric-field nodes (Kirk, Bell, and Arka, 2009), as would be expected in ponderomotive trapping; see Fig. 22. This is therefore referred to as *normal radiative trapping*. The cause is that radiation losses quickly drain the energy of electrons and make them gyrate without any significant drift. Since both the radiation losses and the gyration are enhanced by a magnetic field, this happens in a more prominent form near the electric-field nodes where the magnetic field is maximized.

At even higher field strengths ($a_0 \gtrsim 5000$), Fig. 22 shows that the trapping takes a completely different form. Electrons are instead confined at electric-field antinodes, where the ponderomotive potential is maximized. This counterintuitive phenomenon is called *anomalous radiative trapping* (ART) (Gonoskov *et al.*, 2014).

The explanation of the ART phenomenon involves several logical steps, which we outline here; see Gonoskov *et al.* (2014) for details. Note first that in strong fields RR starts to act as a strong viscosity, suppressing particles' inertia such that they oscillate predominantly along, and in phase with, the oscillating electric field. The motion along the x axis (or the collision axis, i.e., perpendicular to both $\mathbf{E}$ and $\mathbf{B}$) is characterized by two limiting cases (in which the particle is ultrarelativistic): gyration with drift velocity $\mathbf{E} \times \mathbf{B}/B^2$ if $cB > E$ (the blue regions in Fig. 23) or the motion along the RFD with projected velocity $c\mathbf{E} \times \mathbf{B}/E^2$ if $cB < E$ (the red regions in Fig. 23). As E and cB oscillate, the particle motion switches between these cases. From stitching these phases together (which is shown by the green lines in Fig. 23), one might expect the particle to experience no net migration. The key is that the particle only approaches these limiting cases and the approach is asymmetric: the particles have higher energy (during stage II, as labeled in Fig. 23) after the electric-field peaks than after the magnetic-field peaks, when radiation losses are maximized. Thus, during stage II they are less affected by the magnetic field, which deflects them away from the electric-field antinode. This causes a net migration of particles toward those electric-field antinodes; see the black curve in Fig. 23.

Even though RR is discrete in nature at the relevant amplitudes, the basic idea still holds. Furthermore, the threshold to achieve ART is significantly lowered (from 60 to 8 PW) by the onset of cascades, which are triggered at the center of an electric-dipole wave (Gonoskov *et al.*, 2017). This provides an exact 3D standing-wave-like structure, with the antinode at the center; see Sec. V.E.3 for details.

Trapping along the transverse direction (along $\mathbf{E}$ and perpendicular to the x axis) was analyzed by Esirkepov and Bulanov (2017). They considered a dissipative dynamical system $\ddot{x} + k(F)\dot{x} = F$ driven by a periodic force F and a strong nonlinear friction $k(F)\dot{x}$. Sufficiently strong friction makes the system drift antiparallel to the spatial gradient of the driving force, causing apparently paradoxical stabilization near local maxima of F.

In a circularly polarized standing wave, by contrast, ART does not occur. Normal radiative trapping does: numerical simulations show that the radiation losses cause particles to migrate toward field nodes for all $a_0 \gtrsim 70$ (Bashinov, Kumar, and Kim, 2017).

The tendency of particles to align themselves along the local radiation-free direction may also be viewed from the perspective of how energy is transferred from the external field (Samsonov, Nerush, and Kostyukov, 2018). As the RFD points predominantly in the direction of the local Poynting vector, regions of EM energy absorption cause asymmetry and eventually attract particles: as such, it is called *absorption-induced trapping* (Samsonov, Nerush, and Kostyukov, 2018).

It is instructive to compare the trapping cases that we discussed, where particles begin inside the strong-field region, to the case in which they begin outside it. In this case, one would expect ponderomotive expulsion of charged particles from the region of highest intensity. However, in the RR-dominated regime this expulsion can be suppressed, as shown by Fedotov *et al.* (2014), who studied the following field geometry: the electric field rotates around an axis, remaining perpendicular to it; the magnetic field oscillates along the axis; and the amplitude of fields decreases with an increasing transverse distance.

We conclude by observing that trapping phenomena are generally robust against discrete, probabilistic effects that are a feature of RR in the quantum regime. This is because, at the typical wavelength of high-intensity lasers ($\lambda \simeq 1$ μm), laser-accelerated electrons enter the radiation-dominated regime before quantum effects become essential. Nevertheless, for longer wavelengths the radiation-dominated regime can be reached when discreteness does not play an important role; see Fig. 4. In this case, the continuous RR force enables a variety of trappinglike phenomena, including large longitudinal oscillations in CP standing waves [called NRT$^+$ by Bashinov, Kumar, and Kim (2017)] and attractors in LP standing waves (Esirkepov *et al.*, 2015; Bulanov *et al.*, 2017; Esirkepov and Bulanov, 2017), which we discuss in Sec. IV.E.

E. Chaos

The fact that there is only an oscillating electric field and no magnetic-field component at the nodes of a standing wave provides a great simplification from the theoretical point of view. However, charged particles originating at other phases of the standing wave experience much more complicated field configurations. Since both the radiation-reaction and Lorentz forces depend on the particle's momentum, the strength of the EM field acting on a particle and their mutual orientation, nontrivial particle dynamics arise even in the simplest case of two counterpropagating plane waves (Mendonça, 1983; Bauer, Mulser, and Steeb, 1995; Sheng *et al.*, 2002), thereby demonstrating stochastic heating. The inclusion of the radiation reaction makes the particle dynamics even richer for high field intensities, including random walk trajectories, Lévy flights, limit circles, attractors, and regular patterns (Gonoskov *et al.*, 2014; Bashinov, Kim, and Sergeev, 2015; Esirkepov *et al.*, 2015; Jirka *et al.*, 2016; Kirk, 2016; Bulanov *et al.*, 2017; Esirkepov and Bulanov, 2017).

Lehmann and Spatschek (2012) first noted that as the strength of the EM field increases, stochastic heating is reduced and attractors begin to appear. This effect was attributed mainly to phase-space contraction (Tamburini *et al.*, 2011). This transition from chaos to regular dynamics can be illustrated by Poincaré sections, which show the particle coordinates in position and momentum space (x, p_x) at intervals of time equal to the period of the driving field. Figure 24 shows such sections for three different values of a_0. Analysis of the charged particle motion in terms of Lyapunov exponents reveals the existence of attractors, including strange attractors, in the phase space (Bashinov, Kim, and Sergeev, 2015; Esirkepov *et al.*, 2015). This is corroborated by the positivity of the maximum Lyapunov exponent,

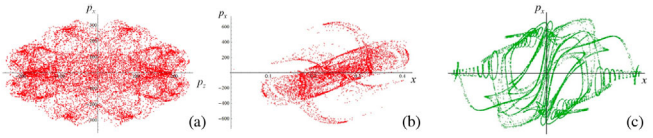

FIG. 24. Poincaré sections showing particle coordinates in the space of position x and momentum p_x at time intervals equal to the period of the driving field. (a) $a_0 = 617$, $\varepsilon_{\rm rad} = 1.2 \times 10^{-8}$. (b) $a_0 = 778$, $\varepsilon_{\rm rad} = 6 \times 10^{-9}$. (c) $a_0 = 1996$, $\varepsilon_{\rm rad} = 1.2 \times 10^{-9}$ From Bulanov *et al.*, 2017.

$$\Lambda = \lim_{t\to\infty} \lim_{|\delta x_0|\to\infty} \frac{1}{t} \ln \frac{|\delta x(t)|}{|\delta x_0|}, \tag{81}$$

where δx_0 is the initial distance between two particle trajectories (Eckmann and Ruelle, 1985).

Particle trajectories in two colliding EM waves have been studied mainly in the framework of classical physics using the Landau-Lifshitz equation (19). One might expect that quantum effects would prevent the formation of regular structures in the particle phase space. However, Jirka *et al.* (2016) showed that particle trajectories still demonstrate strange attractors at electric-field nodes and loops at antinodes; see Figs. 25 and 26. The stochastic nature of photon emission means that trajectories are no longer smooth but fluctuate around the trajectories predicted by classical equations of motion. Nevertheless, important questions concerning the connection between radiative trapping, Lévy flights, limit circles, and attractors remain to be addressed.

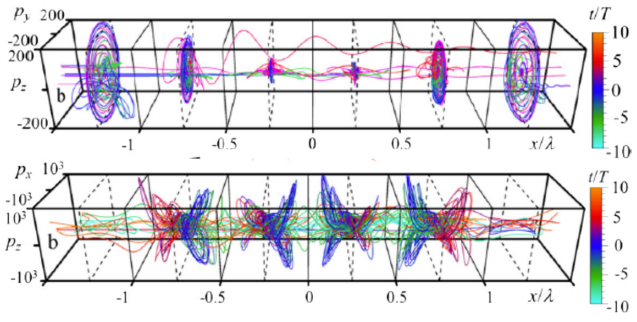

FIG. 25. Electron trajectories in the standing wave formed by two colliding circularly (upper frame) and linearly (lower frame) polarized laser pulses propagating along the x axis with $I = 1.37 \times 10^{24}$ W/cm^2, $\lambda = 1$ μm, duration 33 fs, and focal spot 3 μm. Modeled with semiclassical radiation reaction [Eq. (64)]. From Esirkepov *et al.*, 2015.

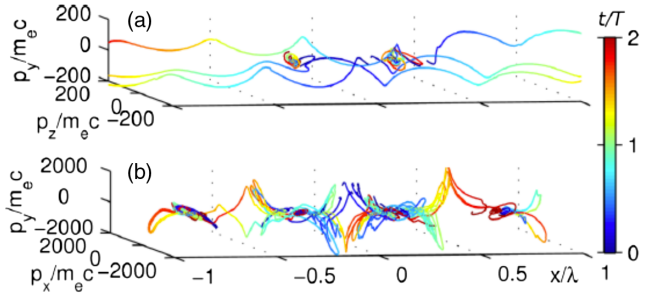

FIG. 26. Electron trajectories in the standing wave formed by two colliding circularly (upper frame) and linearly (lower frame) polarized laser pulses propagating along the x axis with $I = 1.11 \times 10^{24}$ W/cm^2, $\lambda = 1$ μm, duration 30 fs, and focal spot 3 μm. Modeled with quantum stochastic radiation reaction. From Jirka *et al.*, 2016.

F. Pair cascades

When high-energy electrons, positrons, or photons interact with a strong EM field, their energy is converted into secondary particles in a process commonly referred to as a cascade. While the cascade can take different forms depending on the initial conditions and field configurations, there are two basic cases: the *shower* and the *avalanche*. In a shower-type cascade, it is the initial energy of particles (or photons) entering the strong-field region that drives the production of new particles; i.e., the energy, summed over all particles, remains roughly constant as the cascade develops. In the avalanche-type cascade, by contrast, the energy of the participating particles is continuously replenished through their repeated acceleration by the EM field. In this case, the total particle energy grows over time.

The avalanche-type cascade was first identified by Bell and Kirk (2008), where it was realized that, although a single-laser pulse cannot be both accelerator and target for electrons and positrons, two colliding laser pulses can. Electrons accelerated by the rotating electric field at an antinode emit high-energy photons via multiphoton nonlinear Compton scattering; see Sec. II.B.2. This energy loss is compensated for by reacceleration, such that a steady-state energy is maintained (Zel'Dovich, 1975; Bell and Kirk, 2008; Bulanov, Esirkepov *et al.*, 2011). The high-energy photons, which are embedded in a strong background EM field, can subsequently decay into electron-positron pairs via the multiphoton nonlinear Breit-Wheeler process. These pairs are similarly accelerated by the EM field and, as a result, generate additional photons and pairs. As the avalanche cascade develops, the laser energy is transformed into the energy of electrons, positrons, and photons.

Prolific production of secondary particles raises the question of energy balance. Bell and Kirk (2008) noted that creating and accelerating a certain number of electron-positron pairs per joule of laser energy would itself lead to the complete depletion of the laser. This question was further investigated by Fedotov *et al.* (2010), who argued that this depletion prevents the critical field with focused laser pulses to be reached. As a consequence, the observation of the Schwinger effect (pair creation from the vacuum) would require the concentration of stray particles in the experimental chamber to be extremely low so as not to seed a cascade: as low as 10^5 cm^{-3} in the case of dipole-wave focusing geometry (Gonoskov *et al.*, 2013). Bulanov, Esirkepov *et al.* (2010) identified a strong effect of radiation polarization on the development of cascade. In particular, the initial stage of cascade development was found to be suppressed in the case of two linearly polarized, colliding laser pulses due to the field geometry, which might lead to a significant number of Schwinger pairs to be born before the laser is depleted by the cascade. We should also note that depletion of the laser energy is caused not only by pair creation *per se* but also by collective plasma effects when the density of pairs becomes sufficiently large. Heating of the generated electron-positron plasma also leads to rapid laser absorption (Nerush *et al.*, 2011; Grismayer *et al.*, 2016).

The basic features of the avalanche-type cascade in a rotating electric field can be described using the following simple model (Bashmakov *et al.*, 2014; Grismayer *et al.*, 2016,2017). If the probability of the Breit-Wheeler process is P^b, then the pair density grows as $n_\pm = n_\gamma[1 - \exp(-P^b t)]$, where n_γ is the photon density. If the photons are generated by the same pairs and assuming that their energy is the same, we have $n_\pm = \int_0^t dt' P^c\{1 - \exp[-P^c(t - t')]\}$ and

$$\frac{dn_\pm}{dt} = \int_0^t n_\pm(t') P^c P^b \exp[-P^b(t - t')], \tag{82}$$

where P^c is the photon-emission probability. The solution of Eq. (82) has the form $n_\pm \sim \exp[\Gamma t]$, where $\Gamma \sim P^b$ for the most relevant case of $\chi \sim 1$ (Fedotov *et al.*, 2010; Bashmakov *et al.*, 2014; Grismayer *et al.*, 2016, 2017). As pair creation is exponentially suppressed for $\chi < 1$, the onset of the avalanche-type cascade is intrinsically connected with the dominance of the quantum effects (Bulanov, Esirkepov *et al.*, 2010; Fedotov *et al.*, 2010; Bulanov *et al.*, 2011). Recall that $\chi = 1$ corresponds to the intensity of $\sim 5 \times 10^{24}$ W/cm^2 for a 1-μm laser, as detailed in Sec. IV.A; see Eq. (74).

However, numerical studies of avalanche-type cascades using multidimensional QED-PIC codes show that the onset of the cascades is observed at lower intensities $I \sim 7 \times 10^{23}$ W/cm^2 (Bashmakov *et al.*, 2014; Grismayer *et al.*, 2016,2017). This is due partially to the fact that the classical prediction for the radiated power, which is used in deriving Eq. (74), is an overestimate; thus, the electron energy is damped more strongly than it should be, according to QED calculations. The threshold is also lowered by stochastic effects because it is possible for electrons to radiate less than expected and therefore to have higher energy (Duclous, Kirk, and Bell, 2011).

The question of how to initiate an avalanche has received a great deal of attention. The use of seed high-energy electron or photon beams has been studied (King, Elkina, and Ruhl, 2013; Tang *et al.*, 2014), as has the role of the detailed spatiotemporal structure of the laser fields (Tamburini, Di Piazza, and Keitel, 2017; Sampath and Tamburini, 2018). The role of spin and polarization of the electrons, positrons, and photons in multiphoton Compton and Breit-Wheeler processes in relation

to the avalanche development was studied by Seipt *et al.* (2021). The study of dual-beam cascades has been extended to the case of multiple colliding laser pulses (MCLPs)[7] (Gelfer *et al.*, 2015; Gonoskov *et al.*, 2017; Vranic *et al.*, 2017; Magnusson *et al.*, 2019), and to investigations of single-particle and collective dynamics (Jirka *et al.*, 2016; Bashinov, Kumar, and Kim, 2017; Gong *et al.*, 2017; Efimenko *et al.*, 2018; Luo *et al.*, 2018).

In parallel, a comprehensive study of QED effects on laser interactions with solid-density and near-critical density targets has been conducted using simulations. Initially, this effort was justified for considering how they would affect laser-driven ion acceleration (Tamburini *et al.*, 2010),[8] but it was soon realized that such interactions could serve as an efficient source of high-energy photons and electron-positron pairs. The reflection of laser radiation from a plasma surface, and therefore the standing-wave-like structure generated nearby, means that the dynamics bear a close resemblance to the avalanche-type cascade (Ridgers *et al.*, 2012, 2013; Chang *et al.*, 2015; Luo *et al.*, 2015, 2018; Zhang, Ridgers, and Thomas, 2015; Zhu *et al.*, 2015, 2016; Liu *et al.*, 2016; Wang *et al.*, 2017; Slade-Lowther, Del Sorbo, and Ridgers, 2019).

The shower-type cascade is characterized by the fact that the EM field serves only as a target and does not affect particle trajectories to a significant extent. In this case the particle motion is completely determined by QED processes, and the dynamics can be formulated as follows in terms of a system of kinetic equations for electrons, positrons, and photons (Baier and Katkov, 1999; Sokolov *et al.*, 2010; Duclous, Kirk, and Bell, 2011; Bulanov, Schroeder *et al.*, 2013):

$$\frac{d\phi_\pm}{dt} = -\phi_\pm P^c + \int_0^1 \left[\phi_\pm \frac{dP^c}{d\epsilon'} + \phi_\gamma \frac{dP^b}{d\epsilon'}\right] d\epsilon, \tag{83}$$

$$\frac{d\phi_\gamma}{dt} = -\phi_\gamma P^b + \int_0^1 [\phi_+ + \phi_-] \frac{dP^c}{d\epsilon'} d\epsilon. \tag{84}$$

All variables in Eqs. (83) and (84) are as defined in Eq. (58), in which electron-positron pair creation is neglected.

The results of numerical studies of shower-type cascades are in good agreement with the results of the simple analysis of 1D kinetic equations. They demonstrate fast depletion of electron-beam energy and the development of a spectrum with exponentially decaying shape, as well as the generation of electron-positron pairs (Sokolov *et al.*, 2010; Bulanov, Schroeder *et al.*, 2013; Blackburn *et al.*, 2014; Mironov, Narozhny, and Fedotov, 2014; Tang *et al.*, 2014; Wang, Yan, and Zepf, 2015). However, we note that the significant loss of electron-beam energy eventually invalidates the 1D approximation usually employed when one analyzes shower-type cascades. If the transverse momentum of particles is no longer much smaller than the longitudinal momentum, this should be taken into account. Transverse motion of charged particles in EM fields might lead to the development of an avalanche-type cascade in specific EM-field configurations, such as electron-beam interactions with two colliding laser pulses (Mironov, Narozhny, and Fedotov, 2014) and electron-beam interactions with multiple colliding laser pulses (Magnusson *et al.*, 2019; Magnusson, Gonoskov *et al.*, 2019).

G. Electromagnetic field depletion

At extremely high intensities, cascades can be accompanied by the depletion of the EM field itself (Meuren, Keitel, and Di Piazza, 2016; Seipt *et al.*, 2017). Over the course of the multiphoton Compton and Breit-Wheeler processes, which are responsible for transforming the initial electron-beam energy into photons and electron-positron pairs, a significant number of photons are absorbed from the EM field. The interaction of an electron beam of sufficiently high charge with an intense EM field can therefore lead to the depletion of the field energy.

Seipt *et al.* (2017) showed that the multiphoton Compton process in strong EM fields can lead to an energy loss of the laser sufficiently large to invalidate the background-field approximation. This happens when the number of photons absorbed during the process is of the order of the number of photons in the laser pulse. As a result this leads to the following condition on the field strength, number of electrons per laser wavelength cubed, and their energy: $N_e\gamma_e^{-0.92}a_0^{1.08} \gtrsim 6.8\times 10^{11}$, which for $a_0 \sim 10^3$ and $\gamma_e \sim a_0$ gives $N_T \approx 10^{11\text{–}12}$. The number of laser photons absorbed during the Compton process is obtained as follows: in a monochromatic plane-wave laser field, taken to be circularly polarized for simplicity, the kinematics of the photon emission is governed by four-momentum conservation $q + sk = q' + k'$, where s is the number of laser photons. Analyzing how dP^c/ds depends on s shows that the most probable number of photons absorbed is

$$s(\chi_\gamma) = \frac{a_0^3}{\chi_e}\frac{\chi_\gamma}{\chi_e - \chi_\gamma}. \tag{85}$$

Equation (85) is valid for $a_0 \gg 1$ and reproduces the leading order of the related result [Eq. (18)] achieved by Narozhnyi, Nikishov, and Ritus (1965). Thus, when a Compton photon with a given value of χ_γ is emitted, the number of laser photons drawn from the laser field can safely be estimated using Eq. (85) within the model of one-photon incoherent emission.[9] We note that $s(\chi_\gamma) = (\omega_0 L_f)^{-3}$, which means that the shorter the formation length L_f, the greater the number of photons that must be absorbed from the laser to make the emission possible.

Meuren, Keitel, and Di Piazza (2016) discussed electron-positron pair production via the multiphoton Breit-Wheeler process and divided the energy absorbed from the laser in the

[7]We discuss the properties of multiple colliding laser pulses in Sec. V.E.3.

[8]We discuss the effect of the roles of RR and QED in ion acceleration in Sec. VI.D.

[9]A formula completely analogous to Eq. (85) holds for the Breit-Wheeler process $\gamma + s\gamma_L \to e^+e^-$, which becomes possible in a monochromatic wave above a threshold in photon number $s \geq s_0 = 2a_0(1 + a_0^2)/\chi_\gamma$.

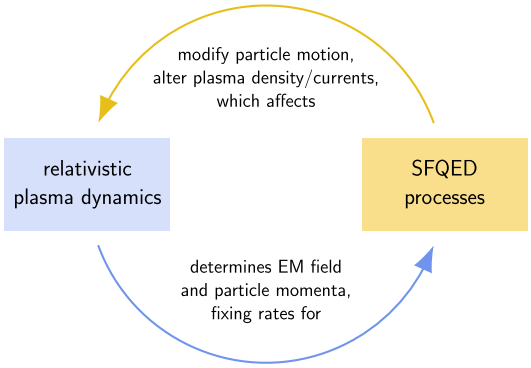

FIG. 27. Feedback between SFQED processes and classical relativistic plasma dynamics in a QED plasma.

interaction into two parts: classical (absorbed in accelerating the electron and positron out of the laser pulse) and quantum (absorbed over the formation length). They showed that these two parts scale differently with a_0: the classical part scales as a_0^3/χ_γ, whereas the quantum part scales as a_0/χ_γ. As such, the classical component dominates at high intensity. The same applies to the multiphoton Compton process (Blackburn *et al.*, 2018).

H. QED plasmas

In Sec. IV.F we reviewed how the development of a shower- or avalanche-type cascade led to the prolific production of photons and electron-positron pairs. When this occurs in a plasma environment or the density of the produced particles is high enough that a plasma environment is created, it is necessary to consider the coupling between SFQED processes and classical plasma dynamics, as illustrated in Fig. 27. This includes the modification of particle trajectories (due to radiative energy losses) and of the plasma density (due to pair production), with the consequence that basic plasma properties are continuously changed. As these properties control the rates for SFQED processes, the interconnection between SFQED effects and plasma behavior gives rise to a unique dynamical system, which is usually referred to as *QED plasma* (Zhang *et al.*, 2020) and is of particular interest for astrophysics; see Sec. I.B.1.

The behavior of the QED plasma is expected to differ dramatically from that of the well-studied classical plasma. These dynamics are primarily studied with numerical simulations (see Sec. III), but one-dimensional analytical models that include classical radiation reaction are available for a thin foil (Bulanov, Esirkepov, Kando, Bulanov *et al.*, 2013) or a surface pair plasma formed during hole boring of a thick target (Kirk, Bell, and Ridgers, 2013). Prolific electron-positron pair production, whether by means of the Schwinger mechanism (Bulanov, Fedotov, and Pegoraro, 2005) or an avalanche-type cascade of photon emission and nonlinear Breit-Wheeler pair creation (Nerush *et al.*, 2011; Grismayer *et al.*, 2016), leads to the backreaction on the incident laser pulse and its fast depletion (and possible change of polarization). Radiation-reaction effects are expected to dominate in laser-driven ion (Tamburini *et al.*, 2010; Del Sorbo *et al.*, 2018) and electron (Stark, Toncian, and Arefiev, 2016; Vranic, Fonseca, and Silva, 2018) acceleration by reducing the available electron energy. However, the combination of RR, laser, and plasma fields can lead to a net energy gain by electrons (see Sec. IV.B), as discussed in the case of a magnetized plasma channel by Gong *et al.* (2019). Energy dissipation affects more than the particles: simulations show that, in hole boring of a thick target with a CP laser, RR leads to the absorption of angular momentum and then to the generation of a quasistatic, axial magnetic field of gigagauss strength (Liseykina, Popruzhenko, and Macchi, 2016).

The feedback between classical plasma, i.e., collective, dynamics, and SFQED processes may be viewed from a global or local perspective. Consider the effect of *relativistically self-induced transparency*, when light of sufficient intensity is transmitted through a plasma that has an electron density above the classical critical density and is therefore expected to be opaque. In a global approach, this can be explained by the fact that sufficiently intense light drives electron oscillations at relativistic velocity, which increases their effective mass and thereby reduces the plasma frequency from $\omega_p = \sqrt{n_e e^2/\epsilon_0 m}$ to $\omega_p/\langle\gamma\rangle$, where $\langle\gamma\rangle \sim a_0$ is the average Lorentz factor of the electron population (Kaw and Dawson, 1970). A reduction of $\langle\gamma\rangle$ because of radiative energy losses would therefore counter the relativistic transparency of a QED plasma (Zhang, Ridgers, and Thomas, 2015). Similarly, exponentially rapid electron-position pair production (see Sec. IV.F), which increases the current density, would increase ω_p and cause the plasma to become highly reflective. Once critically dense, the self-generated plasma would then shield the interior from the incident radiation (Bulanov, Esirkepov *et al.*, 2010; Fedotov *et al.*, 2010).

While a global perspective allows for a general appreciation of SFQED effects, it is not sufficient to explain the complex dynamics that occur in the presence of strong dissipation and pair production. One of the central questions is how this affects the pair cascade itself, which has been studied for laser-plasma (Brady *et al.*, 2014; Slade-Lowther, Del Sorbo, and Ridgers, 2019) and laser-laser (Grismayer *et al.*, 2016) interactions, as well as multiple colliding laser pulses (Gonoskov *et al.*, 2017) and propagating laser-plasma interfaces (Samsonov, Nerush, and Kostyukov, 2019). Numerical studies demonstrate the formation of nonlinear, highly structured plasma as the self-generated current feeds back on the incident light, including the formation of transverse (Muraviev, Bashinov, Efimenko, Gonoskov *et al.*, 2021) and radial current sheets (Efimenko *et al.*, 2018) in dual- and multiple-laser interactions, respectively, as well as plasma pinching around the axis of laser-generated dipole waves (Efimenko *et al.*, 2019); see Sec. V.E.3.

V. EXPERIMENTS

In this section we discuss recent and upcoming experimental campaigns in the regime where radiation-reaction and strong-field QED effects become important. Thus far those experiments have employed electron beams that have been accelerated to ultrarelativistic energies before they encounter an electromagnetic field. This allows $\chi_e \gtrsim 1$ with fields that are subcritical in the laboratory frame. We focus here on

experiments that use a high-intensity laser as the target electromagnetic field. A comprehensive review of crystal-based experiments was given by Uggerhøj (2005), with results since then discussed in Sec. I.B.4.

To identify the interaction regime, we model the interaction as that of a high-energy electron beam and a single, traveling plane EM wave. The threshold for the energy loss to radiation to exceed the work done by the external field is given by $\gamma_0(\gamma_0^2 - a_0^2/4) > (4\varepsilon_{\rm rad})^{-1}$ or $\gamma_0 > 2.8 \times 10^2 \lambda^{1/3}[\mu\text{m}]$ assuming that $\gamma_0 \gg a_0$. However, because the instantaneous work done by a traveling EM wave $\propto a_0^2/\gamma_0$ is small, this condition's being satisfied does not necessarily mean that radiation losses are large in an absolute sense. A better way to quantify the latter is to compare the energy lost over a single cycle of the wave to the electron's initial energy. Thus, radiation-reaction effects are dominant when

$$\frac{4\pi}{3}\alpha a_0 \chi_e > 1 \Leftrightarrow a_0 \gtrsim 59 \frac{\lambda^{1/2}[\mu\text{m}]}{\mathcal{E}_0^{1/2}[\text{GeV}]}, \tag{86}$$

where λ is the laser wavelength and $\mathcal{E}_0$ is the electron's initial energy. This is equivalent to the condition $L_i < \lambda$, where the depletion length L_i is defined in Eq. (13). Quantum effects are dominant when

$$\chi_e > 1 \Leftrightarrow a_0 \gtrsim 105 \frac{\lambda[\mu\text{m}]}{\mathcal{E}_0[\text{GeV}]}. \tag{87}$$

The intensities equivalent to Eqs. (86) and (87) are 2.9×10^{21} and 3.8×10^{21} W cm^{-2}, respectively, for a 2-GeV electron beam and a laser wavelength of 0.8 μm. Note that RR can be substantial if the fractional energy loss is 10% per wavelength (Thomas *et al.*, 2012), as even a 30-fs pulse is approximately 11 cycles long, and similarly that quantum effects, via the suppression of the radiated power, can be evident at $\chi_e \gtrsim 0.1$; see Sec. II.C and Eqs. (86) and (87).

A. Using conventional accelerators

The first experimental campaign to demonstrate nonlinear quantum effects took place at SLAC (Bula *et al.*, 1996; Burke *et al.*, 1997; Bamber *et al.*, 1999), using its conventional radio-frequency accelerator to produce a 46.6-GeV electron beam that collided with a laser pulse having a peak nominal intensity of 1.3×10^{18} W cm^{-2}, a duration of 1.4 ps, and a wavelength of 1054 nm (or 527 nm after frequency doubling). The classical and quantum nonlinearity parameters $a_0 \simeq 0.4$ and $\chi_e \simeq 0.3$ were sufficient for observation of multiphoton Compton scattering (Bula *et al.*, 1996) and multiphoton Breit-Wheeler pair creation (Burke *et al.*, 1997). Measuring the energy spectrum of the scattered electrons over a range of laser intensities (achieved by varying the pulse energy) and comparing the results to simulations showed that up to four laser photons could be absorbed in a single Compton event (Bula *et al.*, 1996).

The emitted photons also drove the creation of electron-positron pairs via the multiphoton Breit-Wheeler process (Burke *et al.*, 1997). In total, 106 ± 14 positrons were detected over a sequence of 22 000 collisions with the frequency-doubled laser, with a yield per collision N_+ that scaled with a_0 as $N_+ \propto a_0^{2n}$, where $n \simeq 5.1 \pm 0.2(\text{stat})^{+0.5}_{-0.8}(\text{syst})$. This scaling is justified on the grounds that, in the weakly nonlinear regime $a_0 \ll 1$, the rate is expected to scale as a_0^{2n}, where n, the number of participating photons, must satisfy $n \geq 5$ to overcome the mass threshold (Burke *et al.*, 1997). Since the time of this experiment, the development of theoretical frameworks that treat photon emission and pair creation as two steps of a unified trident process, and therefore include contributions where the intermediate photon is off shell, has offered new insight into its results (Hu, Müller, and Keitel, 2010; Ilderton, 2011); see Sec. II.B.6 for details.

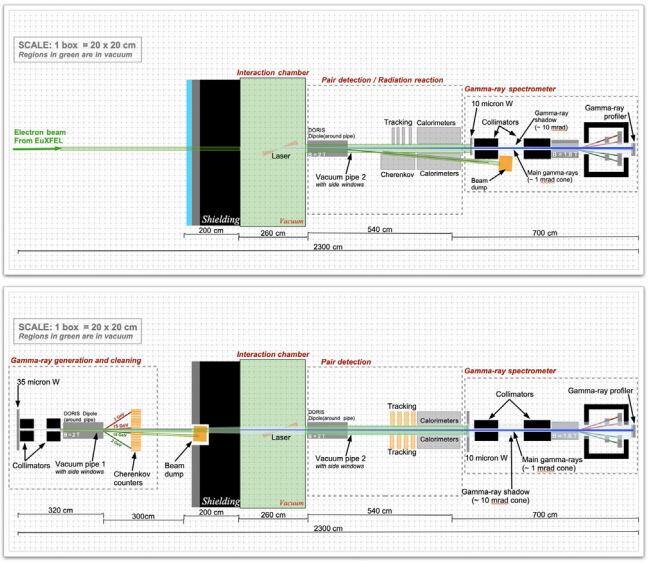

FIG. 28. Experimental configurations envisaged for (top panel) laser-electron and (bottom panel) laser-γ collisions at LUXE. From Abramowicz *et al.*, 2019.

It is now likely that this experiment will be revisited, more than 20 years later, with a higher intensity laser. At SLAC (Yakimenko *et al.*, 2019a), the E320 Collaboration proposes colliding the 13-GeV FACET-II electron beam with a 10-TW class laser, reaching a_0 up to 7 and $\chi_e \sim 1$, and thereby exploring the "quantum tunneling regime" in high-order nonlinear Compton scattering and electron-driven pair creation (Meuren, 2019). The Light Und XFEL Experiment (LUXE) Collaboration has proposed a dedicated experiment at the European XFEL (Abramowicz *et al.*, 2019, 2021) in which one bunch per bunch train of the 17.5-GeV electron beam is extracted into a dedicated beamline and interaction chamber, where it either collides with a 30-TW laser or is used to create high-energy bremsstrahlung photons that themselves collide with the laser; see Fig. 28. (There are plans to upgrade the laser up to 300 TW at a later stage.) With nonlinearity parameters of $a_0 \simeq 2$ and $\chi_e \simeq 0.4$ expected, scientific goals include exploration of nonlinear Compton scattering and γ-driven pair creation in the transition from the multiphoton to the tunneling regime (Abramowicz *et al.*, 2019, 2021).

B. All-optical setups

The experiments described in Sec. V.A crucially depend upon the colocation of a high-power laser system and a

conventional linear accelerator, which usually comes with a unique set of challenges. However, advances in laser-driven wakefield acceleration have made it possible to accelerate electrons to multi-GeV energies in centimeter-scale gas targets (Kneip *et al.*, 2009; Wang *et al.*, 2013; Leemans *et al.*, 2014; Gonsalves *et al.*, 2019), and thereby to realize all-optical collision experiments (Bulanov *et al.*, 2011). Besides the compactness of a laser facility compared to a kilometer-scale conventional accelerator, this exploits the high charge (hundreds of picocoulombs), short duration (tens of femtoseconds), and small size [several micrometers; see Schnell *et al.* (2012)] of wakefield-accelerated electron beams, which maximize the signal from a collision with a laser pulse focused to a comparable spot size. Collision timing is also aided by the inherent synchronization between the driving laser pulse and the electron beam, and between the two laser pulses, provided that they emerge from the same oscillator (Blackburn, 2020); compare this to the natural alignment afforded by a single-pulse retroreflection geometry (Ta Phuoc *et al.*, 2012). However, laser-plasma accelerators suffer from shot-to-shot fluctuations (Samarin, Zepf, and Sarri, 2018), which limited the number of observed events reported by Cole *et al.* (2018) and Poder *et al.* (2018) (see the discussion in this section). These fluctuations can be mitigated by advances in laser technology (Maier *et al.*, 2020). We discuss here all-optical laser–electron-beam collisions as a means of studying nonlinear effects, radiation reaction, and QED. Their role as a source of high-energy radiation is discussed in Sec. VI.A.

Since the first demonstration of Thomson scattering in an all-optical laser-electron collision (Schwoerer *et al.*, 2006), increases in the accessible laser intensity have made it possible to study two classical nonlinear effects[10]: if $a_0 \gtrsim 1$, the electron's anharmonic, relativistic motion causes the Thomson edges to be redshifted by a factor of $1/(1+a_0^2)$, as if the mass had increased, and the emission of higher-order harmonics (Brown and Kibble, 1964; Goldman, 1964; Sarachik and Schappert, 1970; Esarey, Ride, and Sprangle, 1993). The nonlinear relativistic Thomson scattering was first identified using a spectrally resolved measurement of high-energy (up to 18 MeV) and ultrahigh-brilliance photon beams from all-optical collisions at $\gamma \simeq 1100$ and $a_0 \simeq 2$ by Sarri *et al.* (2014). The onset of the nonlinear regime was studied by Khrennikov *et al.* (2015), who tuned the energy of the electron beam in the range $20 < \gamma < 100$ and measured the spectral peak of the x rays emitted when the beam collides with a laser that has $a_0 \simeq 0.9$. More recently Yan *et al.* (2017) reported the measurement of photons with harmonic order > 500 in collisions of electrons with $\gamma = 708 \pm 114$ and a laser pulse with $a_0 \simeq 12$. Further evidence of the transition from the linear to the nonlinear regime is obtained in the asymmetric angular profile of the emitted radiation, as well as in the scaling of the total energy of the radiation with a_0 (Yan *et al.*, 2017).

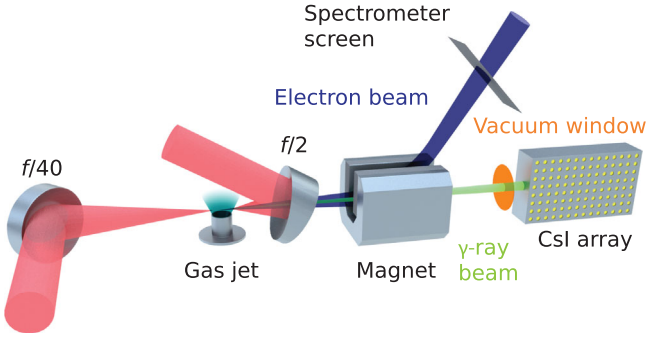

FIG. 29. All-optical realization of a laser–electron-beam collision experiment. One laser pulse is focused using a short-focal-length optic with a hole in it to allow for counterpropagation of an electron beam that is accelerated by a laser wakefield in a gas jet. Electrons, and the radiation they emit, are transmitted through this hole before being diagnosed. The collision is timed so that it occurs close to the edge of the gas jet, where the electron beam is smallest, to maximize overlap with the laser pulse. From Cole *et al.*, 2018.

All-optical laser-electron collisions have now reached a regime where neither radiation-reaction nor quantum effects are negligible, as the intensities available with tight focusing of petawatt-class lasers are comparable to the thresholds given by Eqs. (86) and (87). The first experimental campaigns to find evidence of radiation reaction (Cole *et al.*, 2018), as well as quantum effects on the same (Poder *et al.*, 2018), have now been reported. Both were performed at the Rutherford Appleton Laboratory using the Gemini laser system (Hooker *et al.*, 2006), which delivers two synchronized pulses with energy ~10 J, wavelength 800 nm, and duration 45 fs. The design, which is essentially common to both, is sketched in Fig. 29. To produce a high-energy electron beam using wakefield acceleration, one laser pulse was focused with a long-focal-length optic ($f/40$) onto the leading edge of a 15-mm supersonic helium gas jet by Cole *et al.* (2018) and the entrance of a helium-filled gas cell by Poder *et al.* (2018). The second laser pulse is focused tightly (peak $a_0 \simeq 20$ in both experiments) with a short-focal-length, off-axis parabola ($f/2$) that has an $f/7$ aperture in its center. This allows for counterpropagation of a second, high-intensity laser and an electron beam, which maximizes χ_e because the first laser, the electron beam, and any γ rays produced in the collision can pass through the aperture and be blocked or diagnosed.

The advantage of a gas cell over a gas jet is the improved stability and higher energy of the electron beam (Poder *et al.*, 2018). On the other hand, to avoid the second, higher intensity laser damaging the gas cell itself, the point where it is focused, and where the collision takes place, must be 1 cm downstream, where the electron beam has expanded to a transverse size comparable to that of the laser pulse. This means that the electrons effectively sample a range of collision a_0, which weakens the relevant signals and complicates the theoretical analysis. Cole *et al.* (2018) focused the second laser at the rear edge of the gas jet, close to where the electron beam leaves the plasma, therefore making it much smaller. A systematic

[10]For completeness, note that the same effects have been observed in other laser-based geometries, including collisions with a 60-MeV electron beam from a linear accelerator, using the angular structure of the second and third harmonics at laser amplitudes of $a_0 = 0.3$ and 0.6 (Babzien *et al.*, 2006; Sakai *et al.*, 2015), as well as in a laser-driven gas, using the laser-intensity and electron-density dependence of the second-harmonic light (Chen, Maksimchuk, and Umstadter, 1998).

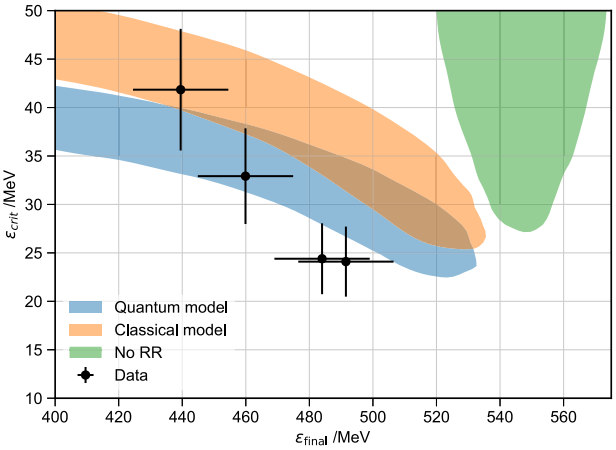

FIG. 30. Experimental evidence of radiation reaction in the correlation between the energy of the electron beam after the collision and the critical energy of the γ-ray spectrum as measured in four successful collisions (points), which are compared to simulations of the interaction that include various models of radiation reaction and fluctuations in the electron energy and laser intensity. Colored (shaded) regions from left to right: classical RR (blue), stochastic RR (orange), and no RR (green). From Cole *et al.*, 2018.

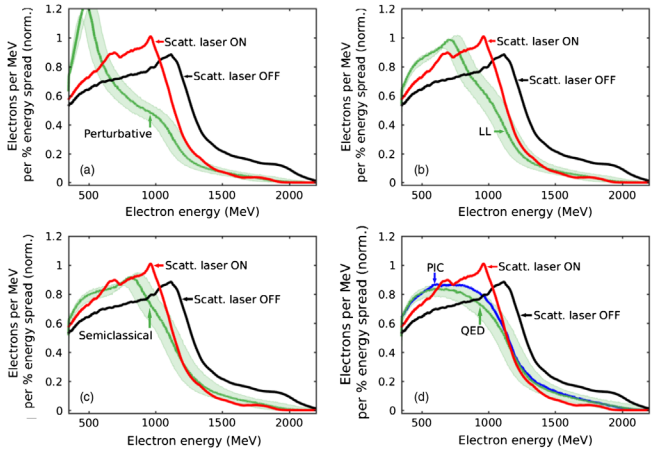

FIG. 31. Experimental evidence of radiation reaction and quantum corrections: electron energy spectra as measured at best overlap, without the scattering laser (black line) and with it (red line), and from simulations without (a) radiation reaction, (b) classical (Landau-Lifshitz) radiation reaction, (c) a quantum-corrected Landau-Lifshitz model, and (d) stochastic radiation reaction (PIC and single-particle codes in green and blue, respectively), all including experimental uncertainties in the initial electron spectrum, the magnetic spectrometer, and the laser intensity. Adapted from Poder *et al.*, 2018.

timing offset in both experiments means that the a_0 at the collision point is $a_0 \simeq 10$, rather than $a_0 \simeq 20$.

Since fluctuations and drifts in the collision timing and pointing cause the overlap between the electron beam and the laser pulse, and therefore the strength of any signals of radiation reaction, to vary, access to both electron and γ-ray data on a shot-by-shot basis is essential for identification of successful collisions (Blackburn, 2020). In both experiments, the total γ-ray yield deposited in a stack of CsI crystals is used as a criterion to distinguish such collisions [the spectrometer was discussed in detail by Behm *et al.* (2018)].

The results of Cole *et al.* (2018) are shown in Fig. 30. Over a sequence of eight shots with the second laser on and ten shots with it off, four are measured to have a γ-ray signal significantly above background. The same four have electron-beam energies (as diagnosed using a sharp feature in the measured spectrum) below 500 MeV, as compared to 550 ± 20 MeV for the beam-off shots. Figure 30 shows that this electron energy is negatively correlated with the critical energy of the γ rays, a parameter that characterizes the hardness of the photon energy spectrum and is extracted from measurements of the depth-resolved deposition in the scintillator stack (Behm *et al.*, 2018). The probability of this correlation and of the electron energies to be below 500 MeV on the same four successful shots to occur by chance is 0.03%, and therefore evidence of radiation reaction is obtained at the 3σ level (Cole *et al.*, 2018). Simulations of the interaction, including fluctuations in the initial electron energy and collision a_0, show that the measured energies are inconsistent with the absence of radiation reaction; both classical and quantum radiation reaction are consistent at the 2σ level.

Poder *et al.* (2018) used the total signal in the scintillator, shown to be positively correlated with the energy loss of the electron beam (as compared to a reference beam-off shot), to identify collisions with good and poor overlap. Energy losses of up to 30% are measured for the highest energy electrons in the case of best overlap, which is consistent with, but smaller than, that predicted by the classical Landau-Lifshitz equation [Eq. (19)], assuming an initial $\gamma_e \simeq 4000$ and $a_0 = 10$ (Poder *et al.*, 2018). The best-overlap results are compared in detail against 3D simulations, which use the experimentally measured electron energy spectra and divergence and model the laser transverse profile by means of a two-component Gaussian fit to the measured focal spot. These comparisons, with different models of radiation reaction, are shown in Fig. 31. Classical radiation reaction is shown to overestimate the energy loss, with a coefficient of determination $R^2 = 0.87$. The semiclassical model, where the strength of the radiation-reaction force is scaled by the quantum-correcting factor $G(\chi_e)$ [Eq. (62)], gives better agreement ($R^2 = 0.96$) than both the fully stochastic ($R^2 = 0.92$) and classical models. Poder *et al.* (2018) attributed the discrepancy in the former case to failure of the LCFA or to incomplete knowledge of the structure of the laser pulse. Nevertheless, the failure of the classical model provides strong evidence of quantum corrections to radiation reaction.

C. With high-energy photons

Probing regions having a strong electromagnetic field with high-energy photons, rather than electrons as described previously, has certain advantages. As they are uncharged, photons do not undergo ponderomotive scattering (Gaponov and Miller, 1958; Kibble, 1966; Quesnel and Mora, 1998; Narozhny and Fofanov, 2000), which can prevent electrons from penetrating to the point of highest intensity (Fedotov *et al.*, 2014; Blackburn, 2020), or radiation reaction, which

reduces the energy and thus the quantum parameter (Baumann and Pukhov, 2019; Blackburn *et al.*, 2019; Yakimenko *et al.*, 2019b). Moreover, signals of Breit-Wheeler pair production can be highly sensitive to the laser pulse shape and duration in the nonlinear regime (Titov *et al.*, 2012, 2013; Krajewska and Kamiński, 2014; Titov and Kämpfer, 2020). Simulations show that it is easier to initiate a pair cascade in two counterpropagating lasers by seeding with a photon than an electron of the same energy (Tang *et al.*, 2014).

Photons with the desired GeV-scale energies can be obtained from multi-GeV electrons in several ways (Albert and Thomas, 2016). One attractive method is bremsstrahlung of an electron beam in a high-Z target because photons with energies comparable to the electron itself may be generated. (Alternative laser-based concepts have been proposed as well; see Sec. VI.A.) Denoting the fractional photon energy $f = \hbar\omega'/\gamma mc^2$, where γ is the Lorentz factor of the incident electron, and expressing the thickness X of the target as a fraction x of the radiation length X_0, the photon energy spectrum per incident electron is, for thin targets $x \ll 1$ (Tsai, 1974),

$$\frac{dN_\gamma}{df} = \frac{x}{f}\left(\frac{4}{3} - \frac{4f}{3} + f^2\right), \tag{88}$$

and for moderately thick targets ($0.5 \lesssim x \lesssim 2$) is

$$\frac{dN_\gamma}{df} = \frac{(1-f)^{4x/3} - e^{-7x/9}}{f[7/9 + (4/3)\ln(1-f)]}. \tag{89}$$

Experiments where bremsstrahlung photons collide with a high-intensity laser, envisaged decades ago (Reiss, 1971), now form part of planned experimental programs. Such experiments would explore electron-positron pair creation and cascade formation in the nonlinear regime (Blackburn and Marklund, 2018; Hartin, Ringwald, and Tapia, 2019). The electron beam itself could be sourced from a conventional (Abramowicz *et al.*, 2019, 2021) or laser-wakefield accelerator (Sarri *et al.*, 2013; Turcu *et al.*, 2016). Photon-photon physics platforms can also investigate the linear Breit-Wheeler process (Breit and Wheeler, 1934) or real photon-photon scattering by colliding bremsstrahlung photons with keV x-ray photons from a laser-heated target (Pike *et al.*, 2014; Kettle *et al.*, 2021).

D. Characterization of strong fields

Precise characterization of the experimental conditions is essential in any experiment that aims for precise comparisons with theory. In a laser–electron-beam collision, this encompasses factors such as the electron-beam energy, the energy spread, the size, the collision timing, and the degree of overlap (Samarin, Zepf, and Sarri, 2018). While these differ between conventional and laser-wakefield accelerators, there is a common need to determine the peak intensity of the laser, and the spatiotemporal structure of its focus. The peak intensity is usually calculated using $I_0 = C_s\mathcal{E}_L/\tau A$, where the total energy of the pulse $\mathcal{E}_L$ may be measured at full amplification, the pulse duration τ may be obtained by intensity autocorrelation (assuming a particular temporal shape) or by frequency-resolved optical gating at low power (Trebino *et al.*, 1997), and the area A is obtained from imaging of the focal spot at attenuated power (C_s is a shape constant that accounts for the chosen form of spatial and temporal profile, such as Gaussian). This provides a useful upper bound, although direct measurements show that the full structure of the focus is more complicated (Kiriyama *et al.*, 2018; Jeandet *et al.*, 2019) and is affected by factors that are not evident when measured at low power, such as spatiotemporal couplings (Pariente *et al.*, 2016).

The need to determine the peak intensity at full power, particularly for next-generation lasers where $I_0 \gtrsim 10^{22}\,\mathrm{W\,cm^{-2}}$, has inspired a great deal of recent research. This is of great importance for dedicated SFQED experiments, which rely on accurate measurements of laser intensity at the interaction points for the interpretation of experimental results. For example, interactions at intensities lower than expected might be wrongly interpreted as a quantum effect, as the electrons lose less energy than was classically expected (Samarin, Zepf, and Sarri, 2018). The intensity measurements rely on exploiting various intensity-dependent physical processes, which we now summarize.

1. Ionization of heavy atoms

Strong electromagnetic fields can induce atomic ionization in a number of ways: bound electrons can escape by absorbing multiple photons from the field (Mainfray and Manus, 1991) or, in the quasistatic regime, by quantum tunneling through the Coulomb barrier (Popov, 2004). Using the ionization state as an intensity diagnostic is motivated by the fact that the tunneling rate is exponentially sensitive to the external field strength. For a hydrogen atom in its ground state, the ionization rate $\propto (E_a/|\mathbf{E}|)\exp(-2E_a/3|\mathbf{E}|)$, where $|\mathbf{E}|$ is the strength of the external electric field and $E_a = m^2e^5/(4\pi\varepsilon_0)^3\hbar^4$ is a characteristic atomic field strength (Landau and Lifshitz, 1981). As that characteristic atomic field also grows stronger with an increase of Z, the maximal ion charge state observed when the laser focuses in, and ionizes, a low-density gas fill provides a way to measure the field strength (Link *et al.*, 2006; Ciappina *et al.*, 2019).

2. Charged particle scattering

The peak intensity may also be determined by measuring the charged particle scattering, either directly or via the emitted radiation. The laser light scattered from free electrons, produced by field ionization in the focal region, undergoes an intensity-dependent redshift (Sarachik and Schappert, 1970) that can be used to determine the field strength in the relativistic regime $I_0\lambda^2 \sim 10^{19}\ \mathrm{W\,cm^{-2}\,\mu m^2}$ (Chen, Maksimchuk, and Umstadter, 1998; He *et al.*, 2019). However, at higher intensities electrons are likely to be completely expelled from the focal region in advance of the pulse peak, preventing characterization of the highest field strength. This could be overcome by the use of protons rather than electrons due to their higher mass. Vais *et al.* (2020) proposed the distribution of scattered protons, which originate from a low-density hydrogen gas in the region of the laser focus, as an intensity diagnostic in the regime $10^{21} \lesssim I_0[\mathrm{W\,cm^{-2}}] \lesssim 10^{24}$.

Alternatively, the laser pulse could be probed using an energetic electron beam because the particles are more "massive" due to relativistic effects. During its passage through the laser fields, the electron oscillates with the characteristic angle $a(\mathbf{r})/\gamma$, where $a(\mathbf{r})$ is the local value of the normalized amplitude [$\max a(\mathbf{r}) \equiv a_0$] and $\gamma \gg 1$ is its instantaneous Lorentz factor. The radiation, which is strongly beamed around the electron's instantaneous velocity (Ritus, 1985; Blackburn, Seipt *et al.*, 2020), is therefore emitted into an angular range of $|\theta| < a_0/\gamma$. (For a linearly polarized pulse, the resulting angular profile is elliptical and elongated along the laser polarization axis.) Measurement of the radiation angular profile therefore gives access to a_0, and thus the peak intensity (Har-Shemesh and Di Piazza, 2012), as experimentally demonstrated by Yan *et al.* (2017). In conjunction with measurement of the mean initial and final electron energy, this scheme can be modified to be independent of radiation reaction or quantum effects, which reduce γ by an intensity-dependent amount (Blackburn, Gerstmayr *et al.*, 2020).

A qualitatively distinct proposal is to use the lower energy radiation emitted after the electron has lost most of its energy, when the trajectory is more sensitive to transverse acceleration, as a diagnostic of peak intensity, duration, and polarization (Harvey, 2018). The electrons themselves also carry information about the peak intensity and duration of the pulse because they are deflected down gradients in the spatial intensity profile as they traverse the focal region. Mackenroth, Holkundkar, and Schlenvoigt (2019) showed that the maximal scattering angle is controlled by the ratio of the laser amplitude and initial electron energy.

Besides the peak intensity, the laser duration (at full amplification) could be determined by measuring the radiation emitted by a chirped electron beam colliding at right angles to the laser propagation direction (Mackenroth and Holkundkar, 2019). In principle, the radiation pattern is also sensitive to the carrier envelope phase (CEP) of the laser pulse, which can be inferred for a few-cycle pulse by measuring the radiation's angular aperture (Mackenroth, Di Piazza, and Keitel, 2010), or in a pulse that is up to 10 cycles long by identification of two asymmetric peaks in the angular distribution of the radiation (Li *et al.*, 2018). The CEP is conventionally measured using f-to-$2f$ spectral inference (Apolonski *et al.*, 2000).

E. Future directions

Future experimental objectives include precision tests of SFQED predictions and studies of radiation-dominated particle and plasma dynamics. Various methods have been proposed to obtain evidence of radiation reaction or QED effects stronger than that discussed in Sec. V.B, either by increasing the signal itself or by increasing sensitivity to the same. For example, the use of comparatively low-energy electrons (40 MeV) in a collision with a high-intensity laser means that radiation detected at an angle greater than 90° to the collision axis would be a sensitive signal to, and positive evidence of, RR effects (Di Piazza, Hatsagortsyan, and Keitel, 2009). The use of ultrashort (few-cycle or subcycle) pulses would dramatically increase the impact of quantum effects by raising the possibility of RR quenching (Harvey *et al.*, 2017). Similarly, quantum and classical RR could be distinguished by means of a laser-electron collision at an angle of 90°, where transmission of electrons through the laser would be forbidden classically (Geng *et al.*, 2019).

In laser–electron-beam collision experiments, the principal challenges are beam stability (for all-optical geometries) and maintaining the spatial alignment and temporal synchronization of the two beams. Alignment and synchronization challenges can be overcome with the use of the retroreflected driver as the strong-field environment (Gu *et al.*, 2018; Ji, Snyder, and Shen, 2019) or using a microchannel target (He *et al.*, 2021). Fluctuations can be overcome by means of increased statistics, particularly by monitoring the variance of the electron final energy spread over many shots (Ridgers *et al.*, 2017; Arran *et al.*, 2019). Alternatively, radiation reaction could be diagnosed in a single shot by allowing the electron beam to diverge before the collision: as only part of the electron beam collides with the laser, both the precollision and postcollision energy spectra could be measured simultaneously (Baird *et al.*, 2019).

Reaching high values of the quantum parameter χ is central to such experiments, and we therefore review the literature devoted to this issue. One option would be to colocate a future laser system with a conventional electron accelerator, which can provide lower divergence and energy spread, as well as higher energies and, therefore, larger values of χ. In this case, optimizing the angle of collision (Blackburn *et al.*, 2019) or the localization of the strong-field region by advanced focusing (Magnusson *et al.*, 2019; Magnusson, Gonoskov *et al.*, 2019) can be used to prevent overwhelming radiation losses for electrons entering the strong-field region.

Another direction is reaching even stronger electromagnetic fields with focused laser radiation. While this is primarily a matter of advances in multipetawatt laser technology [see Fig. 2 and Danson *et al.* (2019)], there are alternative methodologies that have been investigated theoretically.

The increase of field strength by means of advanced focusing is fundamentally restricted by the diffraction limit. Thus, the conversion of laser light into higher frequency radiation is a promising route toward achieving even higher intensity. We note that the use of higher frequency radiation makes a quantum regime of interaction more accessible while also reducing the requirements for radiation power; see Fig. 4 and discussion in Sec. I.C. Two major approaches are discussed in the literature: the *relativistic flying mirror*, which is addressed in Sec. V.E.1, and *high-harmonic focusing*, which is examined in section V.E.2. We discuss another approach, based on the coherent summation of the fields from several laser pulses, in Sec. V.E.3.

1. Relativistic flying mirrors

The first approach is based on reflection of an EM wave from a mirror that moves with relativistic velocity. This was first studied by Einstein (1905) as an example of Lorentz transformations. The frequency of the light reflected by a counterpropagating mirror is up-shifted by a factor of $4\gamma_M^2$, where γ_M is the Lorentz factor of the mirror. This is sometimes referred to as a "double Doppler effect." A mirror of this type could be formed in a plasma by means of relativistically

moving density modulations. In an underdense plasma, the wake generated by a high-power laser pulse forms a density cusp when approaching wave breaking, which can reflect EM radiation (Bulanov, Esirkepov, and Tajima, 2003; Martins *et al.*, 2004), in a manner similar to the effect of caustics in optics. An advantage is that the plasma wake has a parabolic shape (Matlis *et al.*, 2006) and therefore acts as a focusing optic (Jeong *et al.*, 2021). However, as this plasma optic moves with relativistic velocity, the radiation is focused in the moving frame with wavelength $\lambda_0/2\gamma_M$, which leads to only γ_M^2 additional intensification. The resulting factor γ_M^6 needs to be modified by the reflection coefficient of this plasma mirror, which scales as γ_M^{-3} or γ_M^{-4}, depending on how the density cusp is modeled (Bulanov, Esirkepov, Kando, Pirozhkov, and Rosanov, 2013). Several other schemes using underdense plasmas have been proposed, including a spherical plasma wave, which focuses the reflected radiation in the laboratory frame, thus producing an additional γ_M^2 factor due to a focal spot defined by the wavelength $\lambda_0/4\gamma_M^2$ (Bulanov, Maksimchuk *et al.*, 2012). Proof-of-principle experimental results were presented by Kando *et al.* (2007), Pirozhkov *et al.* (2007), Bulanov, Esirkepov, Kando, Pirozhkov, and Rosanov (2013), and Kando *et al.* (2018).

Alternatively, a relativistic flying mirror can be formed in the laser-solid interactions usually considered regarding ion acceleration. Kulagin *et al.* (2007), Habs *et al.* (2008), Meyer-ter-Vehn and Wu (2009), and Bulanov, Maksimchuk *et al.* (2010) assumed the laser pulse to be intense enough to drive all the electrons away from the ions in a form of a single high-density sheet (or a series of sheets), as would be the case in the "Coulomb explosion" regime. In the scheme proposed by Esirkepov *et al.* (2009), two laser pulses are incident onto a thin foil: one laser accelerates a thin sheet of electrons as previously described, and the second laser pulse is reflected from it, increasing its intensity by a factor of $4\gamma_M^2$.

Experimental verification of the relativistic flying mirror concept in a laser-foil interaction has yet to be achieved because of the demanding requirements on laser contrast, power, and intensity. The difficulty in generating dense electron sheets moving with relativistic velocity is that they are susceptible to transverse expansion and instability (Macchi, Borghesi, and Passoni, 2013).

2. Focusing of high harmonics

Another approach is to focus the high-order harmonics of laser light generated by laser-solid interactions. Here the rise and fall of the radiation pressure on the electrons at the surface of a solid target causes an oscillatory motion of the laser-plasma interface; in the phase of the motion when the surface moves backward, toward the incident laser, it functions as a moving mirror and thereby up-shifts the frequency of the laser light (Bulanov, Naumova, and Pegoraro, 1994; Gordienko *et al.*, 2005). The plasma mirror model does not indicate the existence of any preferred interaction conditions, whereas simulations show that under certain conditions plasma electrons can be bunched into a layer that generates attosecond-duration, coherent synchrotron emission (an der Brügge and Pukhov, 2010). These observations can be explained using the relativistic electron spring model (Gonoskov *et al.*, 2011, 2018), which further predicts the existence of an optimal laser incidence angle [from 50° to 62° depending on the preplasma scale length (Blackburn, Gonoskov, and Marklund, 2018)]. The concept of oblique irradiation of a groove-shaped mirror at the optimal angle was considered by Gonoskov *et al.* (2011).

The decrease of laser intensity in the transverse directions (from the center of the focal spot to its edges) can be exploited to induce focusing of the high-harmonic radiation due to the varying magnitude of the interface oscillations (Naumova *et al.*, 2004), the varying displacement of the ions (Vincenti *et al.*, 2014), or the varying depth of radiation penetration into a preplasma (plasma denting) (Dromey *et al.*, 2009). Simulations show that the focused radiation has the form of an electromagnetic burst, the short duration of which inhibits the radiation losses that would prevent one from reaching high χ (Baumann *et al.*, 2019), and furthermore that the mechanism is robust against laser and target imperfections (Vincenti, 2019). A 3-PW laser could be used to reach a focused intensity of 10^{25} W cm^{-2} (Vincenti, 2019). With further developments, it has been argued that an intensity equivalent to the critical field strength 10^{29} W cm^{-2} is a realistic objective (Quéré and Vincenti, 2021).

3. Dipole waves

Ultrahigh intensity can also be achieved using a coherent summation of the fields of several laser pulses, which are focused from different directions to the same spot. Consider a laser system that generates a pulse with a peak power $\mathcal{P}$ that after focusing generates a peak field amplitude of $a_0^{(1)}$. Splitting the laser into two beams of equal power $\mathcal{P}/2$ and focusing them on the same point from opposite directions yields an increased field amplitude of $a_0^{(2)} = \sqrt{2}a_0^{(1)}$, purely due to how the energy is redistributed in space. Extending this concept to four or more lasers arranged in counterpropagating pairs in a common plane with polarization along the plane normal results in an even higher amplitude of $a_0^{(n)} = \sqrt{n}a_0^{(1)}$. Further intensification can be achieved by adding pairs of laser pulse at some angle to this initial plane. This concept of MCLPs was formulated by Bulanov, Mur *et al.* (2010) as a way of lowering the threshold for nonperturbative electron-positron pair production from vacuum. The theoretical limit for such a field configuration is given by a "dipole wave," which provides the strongest possible field strength ($a_0^{(d)} \approx 780(\mathcal{P}[\mathrm{PW}])^{1/2}$) for the fixed total power $\mathcal{P}$ (Bassett, 1986); see also Jeong *et al.* (2020). The configuration is so named because the field structure can be viewed as the time-reversed emission of a dipole antenna. The concept was revisited in the context of upcoming experiments by Gonoskov *et al.* (2012). Furthermore, the possibility of practically realizing a dipole wave with the use of 6 or 12 beams, each with a flattop disk transverse intensity profile, was discussed in the Appendix given by Gonoskov *et al.* (2014); the intensity boost is also shown in the inset of Fig. 2. Note that we relate the increase of electric-field strength here to the increase of effective intensity via quadratic dependency, neglecting all the geometrical factors for simplicity.

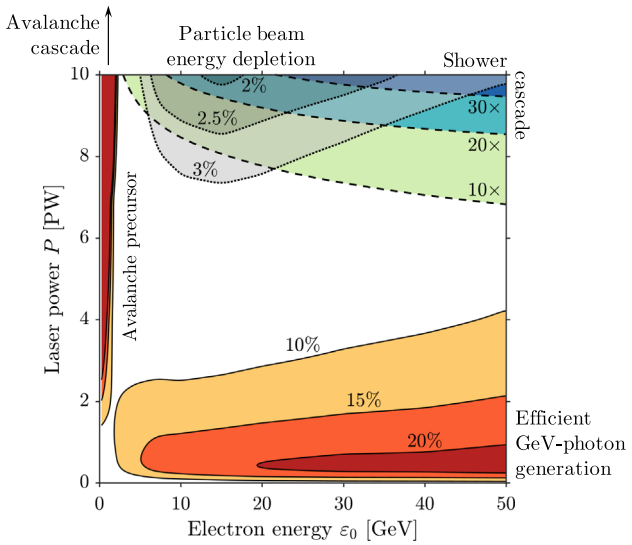

FIG. 32. Interaction regimes in the collision of an electron beam of energy ε_0 with a dipole wave generated by MCLPs with total power P. Number of high-energy ($\hbar\omega > \varepsilon_0/2$) photons per incident electron, red-orange color scale, solid contours; number of electron-positron pairs per incident electron, blue-green color scale, dashed contours; final electron-beam energy, percent of initial value, gray color scale, dotted contours. From Magnusson *et al.*, 2019.

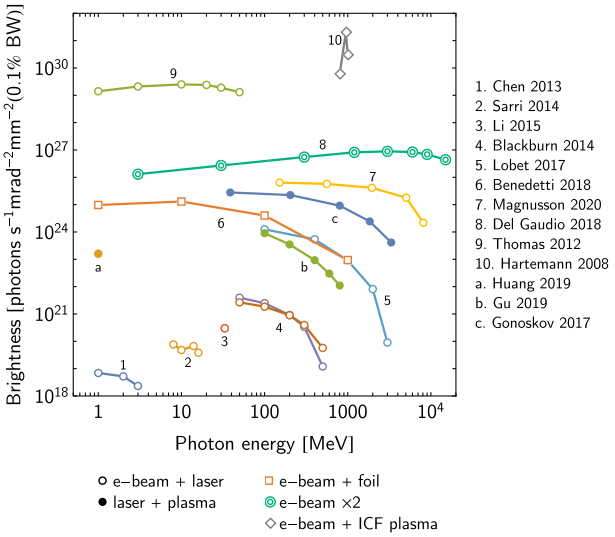

FIG. 33. Brightness of radiation emitted in high-intensity laser interactions with electron beams (empty circles) or plasma targets (filled circles), as well as in nonlaser strong-field environments, as (1 and 2) measured in recent experiments and (3–10) predicted using simulations.

The fact that the dipole wave achieves the greatest possible field strength at fixed power is advantageous for the study of SFQED effects. It could be used to drive nonperturbative pair production from the vacuum (Gonoskov *et al.*, 2013) or to trigger electromagnetic cascades (Gelfer *et al.*, 2015). In addition, the dipole wave naturally provides particle and plasma confinement by means of the ART effect (see Sec. IV.D), which can be further enhanced by pair production cascades in the focus (Gonoskov *et al.*, 2017). QED-PIC simulations show that the development of a self-sustained cascade can be triggered in a dipole wave even at a total power of 8 PW. The high degree of localization of the strong-field region facilitates the creation of highly localized, quasineutral, electron-positron plasma structures, with extreme density (up to $\sim 10^{25}$ cm^{-3}) at powers $8 < \mathcal{P} < 15$ PW (Efimenko *et al.*, 2018). For powers $\mathcal{P} > 20$ PW, simulations indicate that a plasma pinching effect occurs and drives an increase in plasma density up to at least 10^{28} cm^{-3}, and in the electric (magnetic) field strength up to $1/20$ ($1/40$) of $E_{\rm cr}$ (Efimenko *et al.*, 2019). Quasistatic magnetic fields generated during the interaction could be of interest for astrophysical connections (Muraviev *et al.*, 2015).

The dipole wave could also be used in an advanced laser–electron-beam collision geometry (compare to Fig. 19). The advantage is the subwavelength-scale confinement of the strong-field region, which means that electrons can penetrate to the center before their energy is exhausted by radiation emission. This opens up the possibility of studying SFQED phenomena, from single-emission to multistaged processes, including extreme cases of electron-beam energy depletion and shower- and avalanche-type cascades, where there is a significant transformation of the laser or particle-beam energy into secondary particles (Magnusson *et al.*, 2019; Magnusson, Gonoskov *et al.*, 2019) and radiation; see Fig. 33). These different regimes are illustrated in Fig. 32. This shows two distinct regions of relevance for high-energy photon generation: an avalanche precursor for lower electron energies characterized by partial trapping and reacceleration of particles and a shower-type process for higher electron energies and reduced power. Given the advantages that the MCLP concept provides for SFQED studies, one can argue that future laser facility designs should be build around this concept; see Sec. VII.B.

VI. APPLICATIONS

A. Radiation generation

In this section, we discuss the practical consequences of the charged particle dynamics presented in Sec. IV with respect to laser-driven radiation sources. The interest in using high-intensity lasers for this purpose is motivated by the fact that both the total power of the emitted radiation and the characteristic frequency thereof increase with the magnitude of the applied acceleration. This may be characterized by the quantum parameter χ, the transverse acceleration of an EM field in natural units (see Sec. I.A), which increases with γ and a_0, the laser normalized amplitude. The expected scalings for the number of emitted photons, their characteristic frequency, and the total power are a_0^2, γ^2, and $(\gamma a_0)^2$ in the linear regime $a_0 \ll 1$, and a_0, $\gamma^2 a_0$, and $(\gamma a_0)^2$ in the nonlinear regime $a_0 \gg 1$. Beyond the straightforward increase of these qualities with laser intensity, the radiation properties depend on the interaction geometry. In a laser–electron-beam collision, one of the two principal geometries discussed in Sec. IV.A, the radiation properties are largely inherited from those of the electron beam. In a laser-driven plasma, where the laser fields are both accelerator and target, γ depends on a_0 and the

properties of the plasma (such as density and structure), which provides opportunities for optimization. These topics were reviewed by Gu *et al.* (2019) and Vranic *et al.* (2019).

1. Electron-beam-driven radiation sources

Scattering of laser light by a beam of relativistic electrons is a well-known method to generate radiation with desirable properties (Corde *et al.*, 2013; Albert and Thomas, 2016). In the linear regime $a_0 \ll 1$, this is generally referred to as inverse Thomson or Compton scattering (Esarey, Ride, and Sprangle, 1993). While the radiation is characterized by high monochromaticity, polarization purity, and brightness (Hartemann *et al.*, 2005), the small size of the Compton cross section means that high electron densities at the laser interaction point are required for large yields. Furthermore, the photon energy is kinematically limited to $\hbar\omega' \simeq 4\gamma^2\hbar\omega_0$, where ω_0 is the laser frequency, or $\hbar\omega'[\mathrm{MeV}] \simeq 20\mathcal{E}_0^2[\mathrm{GeV}]\lambda^{-1}[\mu\mathrm{m}]$. The multi-MeV range, which is of interest for nuclear physics applications, requires electron-beam energies in the range of several hundred MeV to a few GeV, as available from conventional rf accelerators located at dedicated Compton-photon source facilities, including HIγS (Weller *et al.*, 2009), NewSubaru (Utsunomiya, Hashimoto, and Miyamoto, 2015), and ELI-NP (Gales *et al.*, 2018). However, the advent of compact laser-driven accelerators producing GeV-electron beams has meant Compton scattering has also been investigated all optically (S. Chen *et al.*, 2013; Sarri *et al.*, 2014; Yan *et al.*, 2017); see also Alejo *et al.* (2019).

Increasing the laser intensity, i.e., the photon density, increases the yield of γ rays but also induces nonlinear effects. Redshifting (the "mass shift") and the onset of higher harmonics act to reduce and increase the characteristic photon energy, respectively, thus transforming the emission spectrum from narrowband to broadband and synchrotron-like. This makes it possible to create high-flux γ-ray sources, with photon energies extending up to the initial energy of the electron beam. A useful characteristic of the radiation is the *brightness*, which is a measure of the photon phase-space density. Conventionally measured in units of photons $\mathrm{s}^{-1}\,\mathrm{mrad}^{-2}\,\mathrm{mm}^{-2}$ (at 0.1% bandwidth), it gives the energy $\mathcal{E}$ radiated per unit photon energy $\hbar\omega$, solid angle Ω, area A, and time t:

$$\mathrm{Brightness} = 10^{-3}\frac{\partial^5\mathcal{E}}{\partial\hbar\omega\partial\Omega\partial A\partial t} \tag{90}$$

$$\simeq 10^{-3}\hbar\omega\frac{1}{\pi\sigma_x\sigma_y}\frac{1}{\pi\theta_x\theta_y}\frac{1}{\tau}\frac{dN_\gamma}{d\hbar\omega}. \tag{91}$$

In Eq. (91), $dN_\gamma/d\hbar\omega$ is the number of photons radiated per unit energy, $\sigma_{x,y}$ is the source size in the transverse directions x and y, $\theta_{x,y}$ is the photon divergence in the same directions, and τ is the duration of the radiation burst.

In the beam-driven, nonlinear regime $\gamma \gg a_0 \gg 1$, the radiation emitted by a beam of electrons that collides with a linearly polarized laser pulse is directed into an ellipse with opening half angles $\theta_x \simeq a_0/\gamma$ and $\theta_y \simeq 1/\gamma$, where the major axis x is oriented along the laser polarization (Har-Shemesh and Di Piazza, 2012). The source size $\sigma_{x,y}$ may be estimated as the smaller of the radius of the laser focal spot or the radius of the electron beam and is generally a few microns in magnitude. Similarly, the duration τ is inherited from the duration of the electron bunch. For LWFA electron beams, energies up to a few GeV, durations of tens of femtoseconds (Lundh *et al.*, 2011), and beam radii at focus of a few microns (Schnell *et al.*, 2012) are now achievable. In Fig. 33 we show recent experimental results (S. Chen *et al.*, 2013; Sarri *et al.*, 2014) and theoretical predictions (Thomas *et al.*, 2012; Blackburn *et al.*, 2014; Li *et al.*, 2015; Lobet *et al.*, 2017) for the γ-ray brightness achievable in a collision between an electron beam and a single-laser pulse.

At electron energies and laser intensities large enough for $\chi \gtrsim 1$, it is likely that the highest energy photons decay to electron-positron pairs before escaping the laser pulse. This loss can be reduced by reducing the effective size of the interaction region. Thus, we also show predictions for an electron beam colliding with a dipole wave (Magnusson, Gonoskov *et al.*, 2019) [approximate 4π focusing is achieved by colliding multiple-laser pulses; see Gonoskov *et al.* (2012)], which maximizes the field strength in a region that is subwavelength in size. The same processes may be driven in nonlaser strong-field geometries: Benedetti, Tamburini, and Keitel (2018) showed the magnetic fields generated by filamentation of an electron beam traveling through a solid foil to induce bright, synchrotronlike emission. Del Gaudio *et al.* (2019) studied the collision of two dense electron bunches, each emitting photons in the boosted Coulomb fields of the other bunch; see Sec. I.B.2.

For applications that demand monoenergetic γ rays but also high photon flux, alternative approaches must be explored. Redshifting of the harmonics may be explained as the electron acquiring an intensity-dependent effective mass $m_\star = m\sqrt{1+a_{\mathrm{rms}}^2}$ (Kibble, 1966; Harvey *et al.*, 2012), where $a_{\mathrm{rms}} = a_0$ (circular polarization) or $a_0/\sqrt{2}$ (linear polarization). The variation of this redshift over the pulse envelope $g(t)$ spoils the monochromaticity of the individual harmonics once $a_0 \gtrsim 1$. To benefit from the increased photon yield at a higher laser intensity, Ghebregziabher, Shadwick, and Umstadter (2013), Terzić *et al.* (2014), Rykovanov *et al.* (2016), and Seipt, Kharin, and Rykovanov (2019) proposed chirping the pulse such that the "local frequency" $\omega_0(t) = \omega_0[1 + a_{\mathrm{rms}}^2 g^2(t)]$ (). This compensates for the effective mass increase but is yet to be experimentally demonstrated.

2. Laser-driven radiation sources

In the electron-beam-driven case, the energy of the radiation is largely supplied by the preaccelerated electrons. The laser acts only as the undulator (wiggler) target, thereby separating the acceleration and radiation stages from one another. In the laser-driven case, these stages are combined and the energy of the radiation is drawn ultimately from the laser itself. The combination of simultaneous energy gain and radiation is already a feature of laser-plasma interactions in the classical regime. For example, oscillation of electron bunches accelerated in laser wakefields gives rise to femtosecond bursts of bright, broadband multi-keV x rays, called *betatron*

radiation (Kiselev, Pukhov, and Kostyukov, 2004; Rousse *et al.*, 2004); see the review by Corde *et al.* (2013).

In the low-intensity limit, the response of a plasma is determined by the parameter $n_e/n_{\rm cr}$, where $n_{\rm cr} = \epsilon_0 m\omega_0^2/e^2$ is the classical critical density at frequency ω_0. Plasmas with $n_e/n_{\rm cr} > 1$ are *overdense*, i.e., opaque to the laser light. However, this threshold is altered at high intensity when the electron motion becomes relativistic. In the case of a thin, $\ell \ll \lambda$, solid, $n_e \gg n_{\rm cr}$ density foil, the value of a_0 should exceed $\pi(n_e/n_{\rm cr})\ell/\lambda$, where ℓ is the thickness of the target, for the foil to become transparent (Vshivkov *et al.*, 1998). In the case of extended ($\ell > c\tau_L$) and near-critical density ($n_e \sim n_{\rm cr}$) targets, a_0 should exceed $13.5(n_e/n_{\rm cr})\ell/c\tau_L$ (Bulanov *et al.*, 2010), where τ_L is the laser pulse duration. In both cases realistic parameters for the targets lead to a_0 being around several hundred.

Thus, the relevance for radiation generation is as follows: at higher intensities, an increased penetration of denser targets means that a larger number of electrons are driven by the laser fields. As the emission rate of each individual electron also increases with intensity, dramatic growth of the photon flux and conversion efficiency η are expected. We outline the derivation of an approximate scaling law for η adapted from Popruzhenko, Liseykina, and Macchi (2019). Consider a circularly polarized laser with amplitude a_0 and frequency ω_0 illuminating a plasma with electron areal density $\sigma_e = n_e c/\omega_0$ (i.e., n_e electrons per unit volume in a single skin depth). The radiation intensity $I_{\rm rad}$ is given by the product of the areal density and the radiation power of a single electron $\mathcal{P}_e = (2\alpha mc^2/3\tau_C)\chi^2$, where for circular motion the quantum parameter $\chi = \gamma^2(\hbar\omega_0/mc^2)$. Comparing $I_{\rm rad}$ to the laser intensity I_0, we have $\eta = I_{\rm rad}/I_0 = (2\alpha/3)(\gamma^4/a_0^2)(n_e/n_{\rm cr})\hbar\omega_0/mc^2$. A self-consistent solution for $\gamma(a_0)$ that accounts for radiation losses classically is given in Eq. (77) (Zel'Dovich, 1975). For $n_e = a_0 n_{\rm cr}$, this predicts that $\eta \propto a_0^3$ for $\epsilon_{\rm rad} a_0 < 1$ and $\eta \to 1$ as $a_0 \to \infty$. The conversion efficiency is substantial for $a_0 \gtrsim 439\lambda^{1/3}[\mu\text{m}]$ or, equivalently, $\mathcal{P}[\text{PW}] \gtrsim 13.0 w_0^2[\mu\text{m}]\lambda^{2/3}[\mu\text{m}]$, where w_0 is the focal spot size.

These estimates are borne out by a wide range of simulation studies in the recent literature. In Fig. 34 we show the predicted γ-ray generation efficiency for a variety of laser-driven interaction geometries as a function of the total laser power. The majority of these results were obtained using PIC codes extended to include QED processes; see Sec. III. Nakamura *et al.* (2012) and Ridgers *et al.* (2012) predicted $\eta \simeq 0.3$ for a single 10-PW laser pulse interacting with an aluminum foil and an exponentially rising plasma density ramp, respectively. In both cases, the plasma density is somewhat larger than $a_0 n_{\rm cr}$ and the laser is linearly polarized, which maximizes electron heating. The interaction of circularly polarized lasers with thick plasma targets was investigated by Liseykina, Popruzhenko, and Macchi (2016) and Popruzhenko, Liseykina, and Macchi (2019).

A disadvantage of single-laser irradiation is that the radiation pressure of a high-intensity laser causes longitudinal motion of the plasma electrons, thereby reducing the χ parameter. One way to overcome this is to irradiate a thin plasma target from both sides, with two equally intense laser

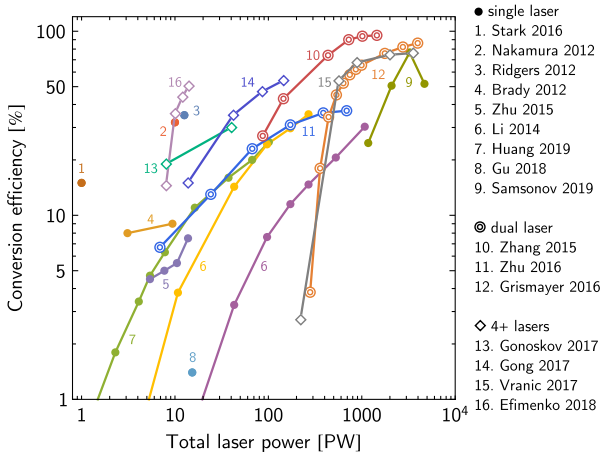

FIG. 34. Efficiency of γ-ray generation in plasmas driven by single (filled circles), dual (double circles), and multiple (diamonds) lasers as predicted by simulations.

pulses. The symmetric radiation pressure arrests longitudinal motion and, by optimizing the electron density, penetration of the laser fields throughout the plasma can be achieved, as well as high (50%) conversion efficiency to gamma radiation (Bashinov and Kim, 2013). The conversion of laser energy to γ radiation can be so efficient that a target expected to be relativistically transparent can instead become optically opaque (Zhang, Ridgers, and Thomas, 2015). The logic of multisided irradiation can be extended to 4 (Gong *et al.*, 2017; Grismayer *et al.*, 2017) or even 12 laser pulses (Gonoskov *et al.*, 2017), creating a two- or three-dimensional optical trap for energetic plasma. Increased axial symmetry of the particle motion in such a field configuration can then enhance the directionality of the radiation emission. The laser and plasma parameters can be chosen to optimize electron-positron pair creation (Vranic *et al.*, 2017) or GeV photon production (Gonoskov *et al.*, 2017; Efimenko *et al.*, 2018).

The use of structured targets provides an opportunity to achieve high conversion efficiency while reducing the required laser power. Ta Phuoc *et al.* (2012) reported how a laser pulse propagating through a gas jet placed in front of a plasma mirror accelerates, then collides with, a trailing electron bunch after the laser pulse is reflected from the mirror. Compton scattering of the electrons then leads to the emission of bright, forward-directed x rays; see also Döpp *et al.* (2016). This "retroreflection" geometry has been studied via simulation, at much higher laser intensities, as a means of generating γ rays and electron-positron pairs (Gu *et al.*, 2018; Huang *et al.*, 2019), as counterpropagation of the laser and electron beams maximizes the quantum parameter χ. Maintaining overlap between the laser pulse and the energetic electrons is a crucial part of achieving high conversion efficiency to synchrotron radiation. One way to do so is to exploit RR-induced trapping (see Sec. IV.D) in a conical target made of a high-density material such as gold and filled with a near-critical-density hydrogen plasma that is irradiated by a laser pulse (Zhu *et al.*, 2015). Electrons are accelerated to GeV energies and confined close to the axis, where the cone has focused the laser pulse to a higher amplitude (Zhu *et al.*, 2015). Two such cones, pointed toward each other and

irradiated from both sides, could be used to generate γ rays with energy densities of the order of 10^{18} J m^{-3} (Zhu *et al.*, 2016) or high orbital angular momentum (Zhu *et al.*, 2018). The relative importance of the laser and plasma fields in driving radiation emission was investigated by Stark, Toncian, and Arefiev (2016) in simulations involving a plasma channel target. They showed that it is a self-generated, quasistatic magnetic field in the channel that allows for high conversion efficiency, as this prevents cancellation between the electric- and magnetic-field contributions to χ for a forward-propagating electron; tens of terawatts of γ rays are predicted for a laser intensity of 5×10^{22} W cm^{-2} (Stark, Toncian, and Arefiev, 2016).

Characteristic of the synchrotron radiation discussed in this section is that the emission is confined to the duration of the laser pulse. This is typically tens of femtoseconds, unlike the radiation from bremsstrahlung of hot electrons, which can persist for picoseconds after the initial interaction due to refluxing (Compant La Fontaine *et al.*, 2013). Numerical solutions of high-intensity lasers impinging on plasma targets show that synchrotron emission dominates over bremsstrahlung, particularly for thin targets, as well as at higher intensities (Martinez, D'Humières, and Gremillet, 2020). Furthermore, the electron population necessary to support efficient radiation generation can be generated by the interaction itself: the development of a QED cascade, when the fields are strong enough that the radiated photons are likely to pair create before leaving the interaction region, can lead to a near-total absorption of the laser energy; see Sec. IV.F.

B. Positron sources

It has long been argued that the problem with the production of positrons in laser-plasma interactions might be one of the bottlenecks for a plasma-based lepton collider. There are several proposals on how to create positrons in laser-plasma interactions for different applications. The most straightforward way was demonstrated by Chen *et al.* (2009, 2015) and Liang *et al.* (2015), who used a moderate intensity laser to irradiate a solid-density target several millimeters thick. As a result, energetic electrons created at the front surface of the target travel through the target emitting bremsstrahlung photons. These photons are converted into electron-positron pairs by colliding with nuclei. Another interesting effect connected with this positron source is that the positrons are accelerated by the sheath fields [typical for target normal sheath acceleration (TNSA)] at the back of the target.

The production of positrons from solid-density foils, but with an externally accelerated electron beam, is a typical procedure used in conventional accelerators. This was recently demonstrated using laser-wakefield-accelerated electron beams (Gahn *et al.*, 2000; Sarri *et al.*, 2013, 2015). Such a setup might be advantageous for plasma-based positron acceleration since it allows for the efficient coupling of produced positrons to the acceleration stage, whether it is laser or electron beam driven; see also U.S. Department of Energy (2016), Cros and Muggli (2019), and Cros *et al.* (2019).

The use of high-intensity lasers and SFQED effects to produce dense bunches of electron-positron pairs is unavoidably coupled to the production of high-energy photons, which is discussed in Sec. VI.A. A common aspect of these geometries is that high-energy photons are produced by Compton scattering inside a strong-field region; thus, it is possible for the photon to "decay" via the nonlinear Breit-Wheeler process before escaping the interaction region. The dependence on field strength, i.e., laser intensity, for pair production is much stronger than for photon emission. Note that the scale for the number of positrons in Fig. 35 covers 10 orders of magnitude for only 3 orders of magnitude in laser power. There are two reasons for this: First, the probability of pair creation is exponentially suppressed at low energy and field strength (see Sec. II.B.4), which means that only the highest energy photons are likely to decay. Second, the production of high-energy photons is itself sensitive to the highest field strength achieved in the interaction.

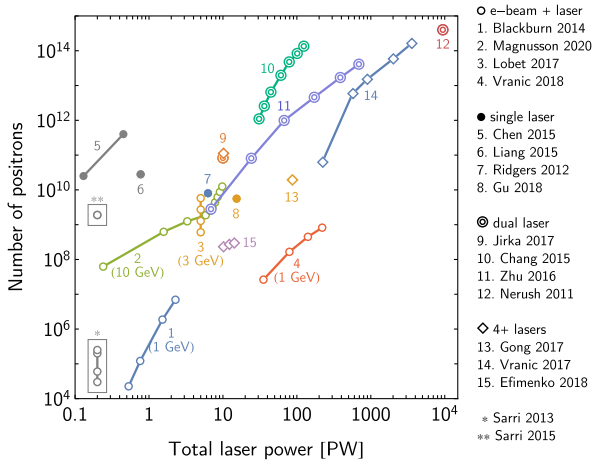

FIG. 35. Number of positrons produced in high-intensity laser-plasma interactions. For laser–electron-beam interactions (empty circles), the energy of the electron beam is noted in brackets. Points marked with asterisks indicate experimental results from LWFA electron-beam interactions with high-Z foils; in these cases the laser power is not indicated.

As one electron is produced for every positron in a pair-creation event, sufficiently prolific pair production should lead to the formation of a "pair plasma." In experiments where LWFA electron beams interact with high-Z materials, these manifest themselves as relativistic, neutral beams (Sarri *et al.*, 2015; Warwick *et al.*, 2017). The possibility of dense positron bunch production via the EM avalanche discussed in Sec. IV.F was first pointed out by Bell and Kirk (2008). Using a single laser and a solid target, thereby exploiting the reflection of the laser to form a standing wave, to generate positrons was proposed by Ridgers *et al.* (2012), who reported a positron density of 10^{26} m^{-3}. Since then, the combination of multiple-laser pulses and structured plasma targets has become a rich field of study for numerical simulations. We present an overview of recent results in Fig. 35, where the number of interacting laser pulses is one (Ridgers *et al.*, 2012; Gu *et al.*, 2018), two (Nerush *et al.*, 2011; Chang *et al.*, 2015; Zhu *et al.*, 2016; Jirka *et al.*, 2017), or more than four (Gong *et al.*, 2017; Vranic *et al.*, 2017; Efimenko *et al.*, 2018). These are compared with the results of experimental campaigns using LWFA electron-beam-driven (Sarri *et al.*, 2013, 2015) or

laser-illuminated (Chen *et al.*, 2015; Liang *et al.*, 2015) high-Z targets.

The results using electron beams and lasers correspond to the shower-type cascade described in Sec. IV.F; i.e., the energy to produce the positrons is supplied by the electron beam rather than the laser itself. The advantages are that the positrons are produced as a collimated beam and the required laser intensity is much lower (Blackburn *et al.*, 2014; Lobet *et al.*, 2017; Vranic *et al.*, 2018; Magnusson, Gonoskov *et al.*, 2019). Radiation reaction means that these positrons are expected to have lower energy than the initial electron beam. We note, however, that a scheme to generate and accelerate positrons was described by Vranic *et al.* (2018), who presented simulations of an electron beam colliding at 90° to an intense laser. Note that if the goal of an experiment is to generate high-energy photons, pair creation instead represents a loss mechanism. The use of highly confined field configurations, such as dipole waves, was proposed as a way to mitigate this loss (Gonoskov *et al.*, 2017; Magnusson, Gonoskov *et al.*, 2019).

C. Polarized particle beams

The elementary processes of photon emission and electron-positron pair creation depend on the spin of the participating particles. While implementation of these processes in simulations using unpolarized rates, which are averaged (summed) over initial (final) spin states, remains standard, the desire to study polarization effects has prompted an extension of these codes to include spin-dependent emission and spin precession, in particular. The underlying theory is reviewed in Sec. II.D; here we discuss the results and implications of this work.

Electrons in a static magnetic field can have their spins aligned parallel or antiparallel to the magnetic field, taking this as the canonical quantization axis. The asymmetric probability of photon emission associated with a change of the electron spin (a spin-flip transition) leads to radiative polarization of the electron population due to the so-called Sokolov-Ternov effect (Sokolov and Ternov, 1968). In storage rings with GeV-electron beams and magnetic fields of a few tesla, the characteristic polarization time ranges from minutes to hours (Mane, Shatunov, and Yokoya, 2005). An equivalent phenomenon is predicted to occur at the magnetic node of the standing wave formed by two counter-propagating, circularly polarized lasers (Del Sorbo *et al.*, 2017). The magnitude of the rotating electric field is such that the polarization time is only a few femtoseconds. The orbit at this node is, however, unstable (Kirk, 2016), which restricts the degree of polarization attainable to approximately 30% (Del Sorbo, Seipt *et al.*, 2018).

Radiative polarization should also occur in the collision between a high-energy electron beam and a single-laser pulse. However, as the magnetic field in a linearly polarized laser oscillates, the polarization built up in one half cycle is lost in the following half cycle. Even for ultrashort laser pulses, where the asymmetry between field oscillations is greatest, the degree of polarization is limited to less than 1% (Seipt *et al.*, 2018). To increase this, it is necessary to break that symmetry, which could be accomplished using a two-color laser pulse (Seipt *et al.*, 2019; Song *et al.*, 2019). Simulations indicate that an average polarization degree of up to 17% could be achieved in the collision of a 5-GeV electron beam with a 160-fs laser pulse that has $a_0 = 16$ and 30% of its energy in the second harmonic (Seipt *et al.*, 2019), or 11% for a 2-GeV electron beam and a 30-fs laser pulse with $a_0 = 100$ and 25% of its energy in the second harmonic (Song *et al.*, 2019). However, as the radiative energy loss and spin polarization are correlated, postselection of electrons below a certain energy can be used to increase the polarization degree to 60%, at the cost of reducing the yield (Seipt *et al.*, 2019; Song *et al.*, 2019). Recent studies also suggest that the spin-field coupling can be enhanced by the use of short, quasiunipolar laser pulses (Aleksandrov *et al.*, 2020; Rosanov, 2021).

Alternatively, spin-dependent radiation reaction in an elliptically polarized (EP) laser pulse can cause an initially unpolarized electron beam to split into two angularly separated beams with opposite polarization degrees. Provided that the degree of ellipticity is a few percent and the laser pulse duration is approximately 5 cycles, postselection of one of the beams yields a polarization degree of up to 65% for an electron initial energy of 4 GeV and $a_0 = 100$ (Li, Shaisultanov *et al.*, 2019). An asymmetry in the angular profile of the radiation, emitted when an initially polarized electron beam collides with such an EP laser pulse, was proposed as a means of diagnosing the polarization degree of that electron beam (Li, Guo *et al.*, 2019). We note that in all the previous cases the spin polarization occurs in the transverse direction.

Polarized electron beams then can be used to generate γ-ray beams with certain polarization properties Li, Shaisultanov *et al.* (2020). These photons could be used to produce polarized positron beams because at high intensity they could decay to electron-positron pairs before escaping the laser pulse, and the pair-creation process is itself spin dependent; see Sec. II.B.2. In a two-color laser pulse with $a_0 = 83$ and 25% of its energy in the second harmonic, Chen *et al.* (2019) showed that, while an initially unpolarized 2-GeV electron beam acquires an average polarization degree of only 8%, the positrons produced by the photons it emits have a much higher polarization degree of 60%. This is because the pair-creation rate is more sensitive to spin than the photon-emission rate (Chen *et al.*, 2019). The same cause underlies polarized positron production in a laser pulse with a small degree of ellipticity. Wan *et al.* (2020) showed that an initially unpolarized 10-GeV electron beam colliding with an EP laser pulse with $a_0 = 100$ drives the creation of two angularly separated positron beams with oppositely oriented polarizations. A yield of positrons equivalent to 1% of the initial electron beam was estimated, with a polarization degree of 86% (Wan *et al.*, 2020). If, however, a prepolarized electron beam is available, photon emission and pair creation in a circularly polarized laser can transfer a high degree of longitudinal polarization (40%–65%) to the created positrons (Li, Chen *et al.*, 2020).

D. Ion acceleration

Laser-based ion acceleration [see Mourou, Tajima, and Bulanov (2006), Daido, Nishiuchi, and Pirozhkov (2012), Macchi, Borghesi, and Passoni (2013), and Bulanov *et al.* (2014, Bulanov *et al.*, 2016) and references cited therein] has

received considerable attention over the last two decades for the potential applications to diverse research areas: fundamental particle physics, inertial confinement fusion, warm dense matter, medical therapy, etc. It is expected that with the fast development of multipetawatt laser facilities, laser ion acceleration will be able to generate ion beams with energies in excess of 100 MeV, as required in many applications. To date laser systems have been able to achieve an acceleration of ions with energies only approaching 100 MeV (Kim *et al.*, 2016; Wagner *et al.*, 2016; Higginson *et al.*, 2018). While most of the experimental results were obtained in the TNSA regime (Maksimchuk *et al.*, 2000; Snavely *et al.*, 2000; Wilks *et al.*, 2001; Fuchs *et al.*, 2006), higher ion energies are expected to be generated by employing advanced regimes of laser ion acceleration, as well as different targets ranging from nanometer-scale solid-density foils to near-critical-density (NCD) slabs, gas jets, and liquid jets. These regimes include *radiation pressure acceleration* (RPA) (Esirkepov *et al.*, 2004; Henig *et al.*, 2009; Kar *et al.*, 2012; Bin *et al.*, 2015), *shockwave acceleration* (Haberberger *et al.*, 2012), *relativistic transparency* (Palaniyappan *et al.*, 2012), *magnetic vortex acceleration* (MVA) (Kuznetsov *et al.*, 2001), and *chirped standing-wave acceleration* (Mackenroth, Gonoskov, and Marklund, 2016). Analytical and computer simulation estimates show that a petawatt or several petawatt laser system may be able to generate ions with energies ranging from several hundred MeV to a GeV per nucleon in these regimes; see Bulanov *et al.* (2016) and references therein. We note that NCD targets, as well as composite targets with NCD parts, have attracted much attention recently for not only ion acceleration (Bin *et al.*, 2015; Bulanov *et al.*, 2015) but also brilliant gamma-ray and electron-positron pair production; see Secs. VI.A and VI.B.

All these results rely on the physics of intense laser pulse interactions with NCD plasma, the basics of which are best illustrated by MVA. At the intensities employed in the aforementioned papers, the effects of the radiation reaction should begin to manifest themselves. However, laser-driven ion acceleration usually does not attract much attention from the point of view of radiation reaction. Moreover, the analytical treatment of the laser ion acceleration is limited to phenomenological one-dimensional models, which employ different simplifications to be solvable. The inclusion of the radiation reaction in these models is questionable since it is not clear if the multidimensional effects that are neglected are more significant than those of radiation reaction. Nevertheless, computer simulation studies of different scenarios of laser ion acceleration, performed with PIC codes, make it significantly easier to include RR effects. Thus, most studies on RR effects in laser ion acceleration employ some kind of numerical description of RR, ranging from classical equations of motion (Landau-Lifshitz) coupled to a 1D PIC code to fully 3D PIC codes with QED modules; see Sec. III.

In most cases, two characteristic targets are considered: a thin solid-density foil and a near-critical-density plasma. In the former, the most relevant mechanism is RPA; in the latter, it is either hole boring (HB) or MVA.

RPA comes into play when the laser is able to push the foil as a whole by its radiation pressure. The idea has a close analogy to the "light sail" scheme for spacecraft propulsion (Zander, 1924; Marx, 1966). The RPA is the realization of the relativistic receding mirror concept (Bulanov, Esirkepov, Kando, Pirozhkov, and Rosanov, 2013), where the role of the mirror is played by an ultrathin solid-density foil. A simple 1D model of RPA describes the foil motion using the following equation (Bulanov *et al.*, 2016):

$$\frac{1}{(1-\beta^2)^{3/2}}\frac{d\beta}{dt}=\frac{2|R|^2+|A|^2}{2}\frac{m_e}{m_i}\frac{a^2(\psi)}{\varepsilon_p}\frac{1-\beta}{1+\beta}. \quad (92)$$

In Eq. (92) $\psi = x - ct$, m_i is the ion mass, β is the foil velocity, R is the reflection coefficient, and A is the absorption coefficient. These coefficients are connected through the energy conservation condition $|R|^2 + |T|^2 + |A|^2 = 1$, where T is the transmission coefficient. The parameter ε_p is defined as $\varepsilon_p = 2\pi e^2 n_e \ell / m_e \omega c$, where ℓ is the target thickness. It governs the transparency of the foil, i.e., $R = R(\varepsilon_p)$: if $a_0 \ll \varepsilon_p$, the foil is opaque to radiation, whereas if $a_0 \gg \varepsilon_p$, the foil is transparent to radiation.

It is plausible that the RR affects both the absorption and reflection of the incident laser pulse. The absorption will be modified through the multiphoton Compton process, i.e., the emission of high-energy photons by the electrons in strong EM field, thus providing the transformation of laser energy into γ's. The reflection will be modified by the creation of electron-positron pairs, through the multiphoton Breit-Wheeler process. Since the absorption is less effective in coupling laser energy to ions and increased opacity leads to a similar effect, one can expect the RR effects to lead to a decrease in the maximum attainable ion energy. This decrease in ion energies has been observed in 1D, 2D, and 3D PIC simulations with classical RR taken into account (Tamburini *et al.*, 2010, 2011; Chen *et al.*, 2011; Wu, Qiao, and He, 2015; Del Sorbo *et al.*, 2018). These studies showed the contraction of the particle phase space due to RR, which manifests itself as a cooling mechanism. However, simulations showed that the effects of RR were significant only in the case of linear polarization of the laser pulse, in which case they lead to a significant reduction of the maximum ion energy. The circular polarization case does not demonstrate any strong influence of RR effects on the process of ion acceleration.

Further studies employed QED-PIC codes to model the interaction of intense laser pulses with solid-density targets (Ridgers *et al.*, 2012; Brady *et al.*, 2014; Zhang, Ridgers, and Thomas, 2015; Del Sorbo *et al.*, 2018; Duff *et al.*, 2018; Samsonov, Nerush, and Kostyukov, 2019), with the production of bright γ rays, laser pulse depletion, and electron-positron cascade development observed. Zhang, Ridgers, and Thomas (2015) developed a model for the relativistic transparency evolution in the presence of SFQED processes. It predicts that a foil, initially transparent for radiation, will turn opaque in strong fields. A significant reduction of the maximum ion energy in the case of linear polarization, as well as no effect in the case of circular polarization, during RPA is also observed in simulations.

Modeling of the laser ion acceleration in the HB regime (Nerush and Kostyukov, 2015; Del Sorbo *et al.*, 2018; Yano *et al.*, 2019), as well as in underdense plasma (Ji, Pukhov, and Shen, 2014; Wang *et al.*, 2017; Wu *et al.*, 2018), shows effects similar to those in thin-foil target interactions, i.e., laser energy depletion due to cascade development, QED-induced opacity, and the decrease of charge-separation fields in plasma.

VII. OUTLOOK

A. Open questions

The state-of-the-art understanding of SFQED phenomena is based on a number of approximations. While in most foreseeable experiments it should be sufficient to characterize the observed phenomena at least at the qualitative level, there are many indications that we are reaching the limits of validity of these approximations. How to go beyond these approximations is among the most pressing questions in the field.

1. Theoretical questions

The plane-wave approximation is the backbone of almost all analytical results in SFQED theory. This is connected with the fact that the Dirac equation for an electron moving in a strong EM plane wave has an exact solution that allows derivation of analytical formulas for the probabilities of quantum process. The existence of an exact solution in this case is due to the fact that plane waves are null fields with a high degree of symmetry (Heinzl and Ilderton, 2017). However, the high-power laser facilities able to deliver high-intensity EM pulses needed for SFQED studies achieve extreme field strengths by focusing laser light on spots comparable in size to the laser wavelength. Tight focusing leads to significant departures from the plane-wave idealization. Furthermore, there is considerable interest in the collisions of multiple laser beams, a field configuration that has many fewer symmetries. This is even more so for EM fields generated in plasma. Thus, looking for new (even approximate) analytic solutions to the Dirac equation in more realistic interaction configurations is necessary. Initial progress in this direction includes focusing (Di Piazza, 2014, 2016, 2017), standing waves (Heinzl, Ilderton, and King, 2016; King and Hu, 2016; Lv *et al.*, 2021), rotating electric fields (Raicher, Eliezer, and Zigler, 2015; Raicher and Hatsagortsyan, 2020), and plasma environments (Raicher and Eliezer, 2013; Mackenroth *et al.*, 2019).

The external field approximation is usually assumed when calculating almost all SFQED process probabilities; i.e., the external field has infinite energy and does not change as a result of photon emission or pair production. However, at certain conditions these processes can lead to the depletion of the EM-field energy, which invalidates the external field approximation (Narozhny *et al.*, 2004a; Bulanov, Fedotov, and Pegoraro, 2005; Bulanov, Esirkepov *et al.*, 2010; Nerush *et al.*, 2011; Seipt *et al.*, 2017; Heinzl, Ilderton, and Seipt, 2018; Ilderton and Seipt, 2018). Here one should distinguish between the previously mentioned quantum depletion and the classical one, which is due to the particle acceleration by the EM field over longer timescales (Meuren, Keitel, and Di Piazza, 2016). A self-consistent analytical framework that accounts for the backreaction of quantum processes, and the particles that they produce on the EM fields, needs to be created (Heinzl, Ilderton, and Seipt, 2018; Ilderton and Seipt, 2018).

In most of the interactions between particles and high-intensity EM fields under consideration, it is plausible that particles undergo multiple quantum processes. Depending on the interaction setup, this could constitute either an avalanche- or a shower-type cascade; see Sec. IV.F. The cascades give rise to a number of interesting phenomena, such as radiative trapping, attractors and chaos in charged particle motion, the generation of positron and photon sources, and the extreme case of plasma structures. Analytical and computational studies of these processes usually rely on the LCFA. A full QED description is limited to two-stage processes such as trident and double Compton; see references in Sec. II.B.6. A full QED treatment of multistaged cascade processes is still lacking, but recently progress has been made in considering beyond-two-vertex processes (Dinu and Torgrimsson, 2020).

The importance of higher-order processes is intrinsically linked to the Ritus-Narozhny conjecture of pertubative SFQED breakdown at $\alpha\chi^{2/3} > 1$ (Ritus, 1972a; Narozhny, 1980; Fedotov, 2017). If one considers the probabilities of Compton and Breit-Wheeler processes at such a field strength, one finds that the mean free paths for electrons, positrons, and photons are of the order of the Compton wavelength. It is questionable, therefore, whether a classical particle trajectory is still a useful concept. However, recent studies show that there is no universal behavior for Compton and Breit-Wheeler processes as $\chi \to \infty$ (Ilderton, King, and Seipt, 2019; Podszus and Di Piazza, 2019). Further studies are needed to determine the exact behavior of SFQED processes in extreme fields and their scalings, which should depend on various initial conditions.

2. Simulation developments

Simulations of the SFQED phenomena are generally based on the LCFA. As discussed in Sec. II.B.4, this is due to the fact that the formation length or time of QED processes is much smaller than the typical inhomogeneities of the EM field in laser-plasma interactions at high intensity. Thus, these processes can be treated as occurring instantaneously and the local value of the EM-field strength can be used to calculate the probabilities. This is expected to be valid if $a_0 \gg 1$ and $a_0^3/\chi \gg 1$ (Ritus, 1985; Dinu *et al.*, 2016; Di Piazza *et al.*, 2019). Otherwise, there are contributions from different formation regions to the same final state (Harvey, Ilderton, and King, 2015). For instance, there always can be photons with the formation length of the order of the EM-field inhomogeneities, even if $a_0 \gg 1$; see Sec. II.B.3. Note that the LCFA is usually accompanied by the assumption of collinear emission, i.e., that the photon is emitted along the instantaneous direction of electron or positron momentum (Blackburn *et al.*, 2018). This is a good approximation for the highest energy photons. Moreover, at the higher intensities considered in laser-plasma interactions,

stronger, ultrashort, and higher frequency EM fields can be generated (Naumova *et al.*, 2004; Teubner and Gibbon, 2009; Gonoskov *et al.*, 2011), so the simple model of a monochromatic carrier wave no longer suffices.

Validity checks of the LCFA were performed by Harvey, Ilderton, and King (2015), Dinu *et al.* (2016), Blackburn *et al.* (2018), and Di Piazza *et al.* (2018). Proposed corrections to the rates include modification of the spectrum at low energy (Di Piazza *et al.*, 2018, 2019), accounting for the dependence on field gradients (Ilderton, King, and Seipt, 2019), and discarding of photons with excessively long formation lengths (Blackburn, Seipt *et al.*, 2020). These proposals have yet to be implemented in the PIC codes used to study laser-matter interactions at high intensity. An alternative strategy is to treat the background field as a locally monochromatic plane wave rather than a locally constant crossed field (Heinzl, King, and Macleod, 2020). This exchanges the flexibility of the LCFA for increased accuracy in modeling interactions with plane-wave-like fields (Blackburn, MacLeod, and King, 2021) and has already been used in connection with experiments (Bamber *et al.*, 1999).

The SFQED emission rates depend on the spin of the electronsand positrons, as well as on the polarization of the photons, as discussed in Sec. II.D and by Ilderton, King, and Tang (2020) and Seipt and King (2020). This can result in the generation of polarized electron, positron, and photon beams [see Chen *et al.* (2019), Seipt *et al.* (2019), King and Tang (2020), and Tang, King, and Hu (2020) and the discussion in Sec. VI.C], which can be important for high-energy physics applications. Studies of spin and polarization effects in the framework of SFQED have started only recently, and more effort is required to advance this topic. Of particular interest is the dependence of the higher-order SFQED effects, such as cascades, on spin and polarization (Seipt *et al.*, 2021).

There are many other important theoretical problems connected with radiative corrections, vacuum polarization, four-wave mixing, photon-photon scattering Cherenkov radiation in strong fields, and beam-beam interactions (Bulanov *et al.*, 2019; Macleod, Noble, and Jaroszynski, 2019; Yakimenko *et al.*, 2019b). We note that beyond the PIC-QED framework used to study SFQED effects there is also the real-time lattice QED approach (Hebenstreit, Berges, and Gelfand, 2013; Shi *et al.*, 2018), which needs to be advanced.

B. Experimental programs

In Sec. IV.A we introduced two basic interaction geometries for the exploration of SFQED effects: a high-energy electron beam colliding with a high-intensity laser pulse and two colliding, high-intensity laser pulses. Based on our discussion of SFQED interaction properties and the availability of lasers and electron beams, we can envisage a three-stage program, with the associated facility development, for experimental research (Zhang *et al.*, 2020). The first two stages correspond to the two basic interaction configurations, whereas the third provides a setup flexible enough to accommodate both at much higher energies and intensities. This three-stage program for laser-based facilities is well aligned with the strategic plans for plasma-based advanced accelerators and novel radiation sources and follows a path from a 10-GeV demonstrator facility to the plasma-based electron-positron collider; for details on plasma-based collider strategic plans, see U.S. Department of Energy (2016), Cros and Muggli (2019), and Cros *et al.* (2019).

In the first stage, the high-power laser facility should be able to investigate the basic quantum processes of SFQED described in Sec. II.B.2 by colliding electron beams and high-intensity laser pulses. This could be realized with two laser beamlines, where one is for particle acceleration (Bulanov *et al.*, 2011; U.S. Department of Energy, 2016; Cros and Muggli, 2019; Cros *et al.*, 2019), or by colocating a petawatt-class laser and an existing conventional lepton accelerator (Meuren *et al.*, 2020). In both cases the laser should be capable of being focused to a spot size comparable to a single wavelength. The parameters required for $\chi \sim 1$ are within reach of existing laser facilities, as 8-GeV electron beams from LWFA have been demonstrated (Gonsalves *et al.*, 2019), as has an intensity of 10^{23} W cm^{-2} from a petawatt of laser power (Yoon *et al.*, 2021). A 10-GeV LWFA module paired with a tightly focused petawatt-class laser or a GeV-class electron beam paired with a multipetawatt laser can satisfy the energy-power requirements, which places the required total laser power into the 1–10 PW range. We note that this setup is similar to that of the E144 experiment at SLAC (Bula *et al.*, 1996) and two recent ones at GEMINI (Cole *et al.*, 2018; Poder *et al.*, 2018). However, it is of critical importance to study SFQED effects in such a configuration at higher precision and energy. As such, it is important that the facility deliver stable, high-repetition-rate collisions, with the ability to tune the electron energy and laser intensity across a few orders of magnitude. This would permit exploration of the classical-to-quantum, perturbative-to-nonperturbative transitions, as well as tests of the approximations underlying analytical and numerical predictions of SFQED; see Sec. VII.A. There are a number of existing, under construction, and planned laser facilities that satisfy the aforementioned requirements of 1–10 PW power (see Fig. 2): L4 at ELI-Beamlines in Czechia, HPLS at ELI-NP in Romania, Apollon (F1) at LULI in France, PEARL-X at IAP in Russia, SULF at SIOM in China, J-EPOCH at ILE or QST in Japan, EP-OPLA at LLE in the USA, CoReLS at IBS in South Korea, ZEUS at CUOS in the USA, and ATLAS-3000 at CALA in Germany.

In the second stage, the high-power laser facility would reach the radiation-dominated regime and produce avalanche-type cascades. The simplest configuration is two counterpropagating laser pulses; however, dividing the same amount of power among multiple colliding laser pulses that arrive at the same interaction point is more beneficial from the point of view of reaching extreme field strengths. Reaching the radiation-dominated regime, assuming a focal spot size of a few wavelengths, demands a total laser power in the range of 10–100 PW. Scientific goals at this stage would be higher-order SFQED processes and the rich dynamical phenomena that accompany them; see Sec. IV. The coupling between

classical, relativistic plasma-physics and quantum effects will put numerical models into the test, particularly as significant field depletion is expected.

In the third stage, the facility would be flexible enough to accommodate both accelerator and SFQED studies. A sketch is shown in Fig. 36. Three modes of operation are possible: (i) a plasma-based electron-positron collider, (ii) a plasma-based electron or positron and laser collider, and (iii) multiple colliding laser pulses. The first mode corresponds to a compact means to achieve electron-positron collisions relevant for high-energy physics. Dense electron or positron beams can themselves induce SFQED phenomena due to the strong fields that accompany them, as discussed in Sec. I.B.2. In the second mode, the lasers from one arm are rerouted to the interaction point to form a standing EM wave, which is probed by the high-energy electron beam accelerated by the lasers in the other arm. This type of interaction was discussed by Magnusson *et al.* (2019) and Magnusson, Gonoskov *et al.* (2019) as a means of studying both shower- and avalanche-type cascades and as a high-brightness source of multi-GeV photons. The third mode should provide the ultimate test for SFQED by achieving the highest possible intensity, with all the lasers focused at the interaction point.

VIII. CONCLUSIONS

The study of charged particle motion, induced by electromagnetic fields of different origin, forms one of the pillars that support our understanding of the natural world. It extends from basic electrostatics and magnetism to classical and quantum electrodynamics and is unavoidable in extreme plasma environments such as those found in terrestrial laboratories and in space.

In this review, we have summarized the results of recent research on charged particle motion and radiation in strong electromagnetic fields. While these strong fields can be encountered in highly magnetized astrophysical environments, during beam-beam interactions in particle colliders, and in heavy-ion collisions, we have focused on the interactions involving high-intensity lasers. Owing to the fast development of laser technology, lasers now produce some of the strongest electromagnetic fields available in the laboratory. While present-day lasers can efficiently accelerate particles to relativistic energies and produce sources of high-frequency radiation, their next-generation counterparts will provide EM-field strengths so much higher that they will access the so-called radiation-dominated regime, where the motion of particles will be determined not by only by external fields but also by the self-generated, i.e., radiation, fields.

Although the problem of radiation reaction in classical electrodynamics dates back to Lorentz, Abraham, and Dirac (see Sec. II.A) and the first results in SFQED were obtained in the 1960s, the advance in laser technology (see Fig. 2) has prompted significant recent progress in theory (Sec. II.B), simulations (Sec. III), and experiments (Sec. V). The coupling between SFQED processes and classical, relativistic plasma physics has unveiled new complex dynamics and raised the possibility of developing new high-flux particle and radiation sources. All these effects are of interest for quantum field theory and will dominate the operation of next-generation laser facilities, whether they are designed specifically for the study of SFQED effects, for particle acceleration at the multi-GeV and TeV levels, or for secondary radiation generation.

Despite the tremendous progress achieved, there are many open questions in SFQED; see Sec. VII.A. Solving these problems will require the coordinated effort of theoretical, simulation, and experimental groups and is likely to occupy the SFQED community for several years to come. Many new puzzles will arise as the next generation of laser facilities comes into operation, when long-held theoretical expectations will be challenged by experimental evidence. We view this as the most exciting prospect in our field.

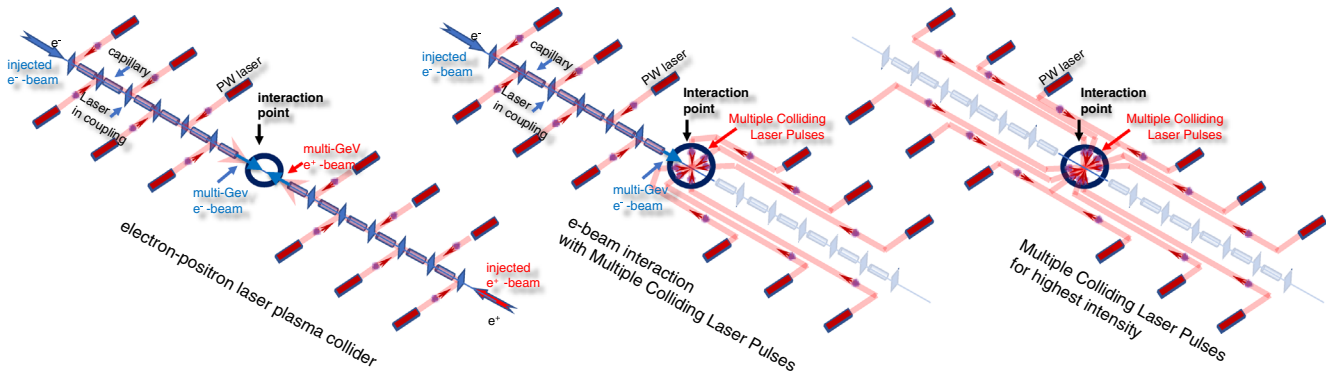

FIG. 36. Dedicated SFQED facility housing multiple petawatt-class lasers. The facility can operate in several modes, including (i) an e^+e^- collider, with all lasers used to drive the staged acceleration of electron and positron beams; (ii) a laser–electron-beam collider where half of the lasers drive the staged acceleration of the electron beam and the remaining half provides the high-field region via the multiple colliding pulses configuration; and (iii) all the laser pulses are brought to the interaction point to generate the highest intensity possible. From Zhang *et al.*, 2020.

IX. LIST OF SYMBOLS AND ABBREVIATIONS

e	1.602×10^{-19} C	elementary charge
m	0.511 MeV$/c^2$	electron mass
c	299 792 458 m s^{-1}	speed of light in vacuum
α	$e^2/4\pi\varepsilon_0\hbar c \simeq 1/137$	fine-structure constant
$\lambda\!\!\!^{-}$	$\hbar/mc \simeq 386$ fm	Compton wavelength
$E_{\rm cr}$	$m^2c^3/(e\hbar) \simeq 1.323 \times 10^{18}$ Vm^{-1}	critical field of QED
$B_{\rm cr}$	$m^2c^2/e\hbar \simeq 4.4 \times 10^9$ T	critical magnetic field of QED
$E_{\rm cr}^{\rm clas}$	$E_{\rm cr}/\alpha \simeq 1.813 \times 10^{20}$ V m^{-1}	classical critical field
p^μ	$\gamma m(c, \mathbf{v})$	particle four-momentum
γ	$(1 - v^2/c^2)^{-1/2}$	Lorentz factor
$\hbar k^\mu$	$\hbar\omega/c(1, \mathbf{k})$	photon four-momentum
$\hbar\kappa^\mu$	$\hbar\omega_0/c(1, \mathbf{k})$	laser four-momentum
$F_{\mu\nu}$	EM-field tensor	
$\tilde{F}_{\mu\nu}$	dual EM-field tensor	
$\mathcal{F}$	$-F_{\mu\nu}F^{\mu\nu}/2E_{\rm cr}^2$	first Poincaré invariant
$\mathcal{G}$	$-F_{\mu\nu}\tilde{F}^{\mu\nu}/2E_{\rm cr}^2$	second Poincaré invariant
χ_e	$\lvert F_{\mu\nu}p^\nu\rvert/mcE_{\rm cr}$	lepton quantum nonlinearity parameter
χ_γ	$\lvert F_{\mu\nu}\hbar k^\nu\rvert/mcE_{\rm cr}$	photon quantum nonlinearity parameter
a_0	$e\lvert F_{\mu\nu}p^\nu\rvert/mc^2\kappa_\mu p^\mu = eE_0/mc\omega_0$	dimensionless EM vector potential
γ_K	$\omega_0\sqrt{2mV_0}/eE_0$	Keldysh parameter
$a_{\rm cr}$	$mc^2/\hbar\omega_0 \simeq 4.1 \times 10^5\lambda[\mu\text{m}]$	a_0 corresponding to a QED-critical field
$\mathcal{P}_{\rm rad}$	power radiated by an electron accelerated by an EM field	
L_i	$\gamma mc^3/\mathcal{P}_{\rm rad}$	depletion length: distance over which electron radiates away energy equal to its own energy
L_q	quantization length: typical distance between photon emissions	
L_f	$\langle\theta^2\rangle^{1/2}\chi_e\lambda\!\!\!^{-}/\gamma^2 \simeq (c\chi^{1/3}/a_0\omega_0)[(1-f_c)/f_c]^{1/3}$	formation length: typical distance over which a photon is emitted
P_b	pair-creation rate	
L_p	c/P_b	pair-creation length
$\varepsilon_{\rm rad}$	$4\pi r_e/3\lambda \simeq 1.17 \times 10^{-8}/\lambda[\mu\text{m}]$	dimensionless parameter that characterizes the role of radiation reaction in charged particle motion
$a_0^{\rm crr}$	$\varepsilon_{\rm rad}^{-1/3} \simeq 440\lambda^{1/3}[\mu\text{m}]$, $(4\pi\varepsilon_{\rm rad}\gamma)^{1/2} \simeq 5.9\lambda^{1/2}[\mu\text{m}]/\mathcal{E}_0[\text{GeV}]$	classical RR threshold (laser-laser and laser–electron-beam interactions, respectively)
$a_0^{\rm qrr}$	$4\alpha^2/9\varepsilon_{\rm rad} \simeq 2000\lambda[\mu\text{m}]$, $\alpha/3\varepsilon_{\rm rad}\gamma \simeq 105\lambda[\mu\text{m}]/\mathcal{E}_0[\text{GeV}]$	quantum threshold (laser-laser and laser–electron-beam interactions, respectively)
$g_{\rm LAD}^\mu$	RR term in Landau-Lifshitz equation	
$g_{\rm LL}^\mu$	RR term in Landau-Lifshitz equation	
$d\mathcal{E}/d\hbar\omega$	energy radiated per unit photon energy	
$dW/d\hbar\omega$	spectral emission rate	
f_c	$\hbar\omega/\gamma mc^2$	energy transfer from electron to photon in Compton scattering
ξ_q	$(2/3\chi_e)f_c/(1-f_c)$	Compton spectrum shape parameter
ψ_{pr}	Volkov solution of the Dirac equation	
P^c	probability rate of the Compton process	

P^b	probability rate of the Breit-Wheeler process
φ_e	electron distribution function
$G(\chi)$	$(3\sqrt{3}/\pi)\int_0^\infty K_{2/3}(u)[(8u+15\chi u^2+18\chi^2u^3)/(2+3\chi u)^4]du$
	ratio between the instantaneous radiation powers predicted by QED and classical theory; also referred to as the Gaunt factor
ε_p	$2\pi e^2 n_e l/m_e\omega_0 c$
	parameter governing the transparency of the thin solid-density foil under the action of EM wave

TABLE II. Parameters of the laser facilities shown in Fig. 2.

Name	Facility	Country	Wavelength (μm)	Energy (J)	Duration (fs)	Power (PW)
Station of Extreme Light	SIOM	China	0.9	1500	15	100
EP-OPAL	LLE	USA	0.8	500	20	25
SULF	SIOM	China	0.8	220	21	10
Apollon (F1)	LULI	France	0.82	150	15	10
PEARL-X	IAP	Russia	0.527	200	20	10
L4	ELI-Beamlines	Czechia	1.057	1500	150	10
HPLS	ELI-NP	Romania	0.814	200	20	10
J-EPOCH	ILE + QST	Japan	0.8	200	20	10
SULF (current)	SIOM	China	0.8	130	24	5.4
SG-II 5 PW	SIOM	China	0.808	150	30	5
CAEP-PW	CAEP	China	0.8	91	19	4.8
CoReLS	IBS	South Korea	0.8	83	20	4.15
ZEUS	CUOS	USA	0.8	60	20	3
ATLAS-3000	CALA	Germany	0.8	60	25	2.4
Qiangguang	SIOM	China	0.8	52	26	2
SG-II 5 PW	SIOM	China	0.808	37	21	1.8
Apollon	LULI	France	0.82	38	22	1.7
Nova Petawatt	LLNL	USA	1.054	660	440	1.5
BELLA	LBNL	USA	0.8	40	30	1.3
LFEX	GEKKO XII	Japan	1.054	2000	1500	1.3
J-KAREN-P	KPSI	Japan	0.82	40	30	1.3
PETAL	CEA	France	1.053	850	700	1.2
Xtreme Light III	NLCM	China	0.8	32	28	1.1
CoReLS	IBS	South Korea	0.8	33	30	1.1
Z-Petawatt	Sandia	USA	1.054	500	500	1
Vulcan Petawatt	CLF, RAL	UK	1.054	500	500	1
Orion	AWE	UK	1.053	500	500	1
Apollon (F2)	LULI	France	0.82	15	15	1
PEnELOPE	HZDR	Germany	1.03	150	150	1
VEGA-3	CLPU	Spain	0.8	30	30	1
CETAL	INFLPR	Romania	0.8	25	25	1
L2	ELI-Beamlines	Czechia	0.82	15	15	1
L3 (HAPLS)	ELI-Beamlines	Czechia	0.82	30	30	1
SG-II UP (Shenguang II)	SIOM	China	1.054	1000	1000	1
PWM (Petawatt Module)	GEKKO XII	Japan	1.054	420	470	0.89
Texas Petawatt	Univ. of Texas at Austin	USA	1.057	120	140	0.86
J-KAREN	KPSI	Japan	0.8	28	33	0.85
Xingguang-III (fs beam)	LFRC	China	0.8	20	27	0.74
OMEGA-EP (short pulse)	LLE	USA	1.053	500	700	0.71
Diocles	ELL	USA	0.8	20	30	0.67
NIF	LLNL	USA	0.3516	1.80×10^6	3.00×10^6	0.6
PEARL	IAP	Russia	0.91	24	45	0.53

(Table continued)

TABLE II. *(Continued)*

Name	Facility	Country	Wavelength (μm)	Energy (J)	Duration (fs)	Power (PW)
HERCULES	CUOS	USA	0.8	15	30	0.5
Gemini	CLF	UK	0.8	15	30	0.5
Laser Megajoule	CEA	France	0.351	1.50×10^6	3.00×10^6	0.5
PHELIX	HI GSI	Germany	1.054	200	400	0.5
Titan (west)	LLNL	USA	1.053	300	700	0.43
SCAPA	Univ. of Strathclyde	UK	0.8	8.75	25	0.35
Scarlet	Ohio State Univ.	USA	0.8	10	30	0.33
Jeti200	HI Jena	Germany	0.8	4	17	0.24
ALEPH	Colorado State Univ.	USA	0.4	10	45	0.2
POLARIS	HI Jena	Germany	1.03	17	98	0.17
Arcturus	Heinrich-Heine Univ.	Germany	0.8	3.5	30	0.12
DRACO	HZDR	Germany	0.8	3.5	30	0.12

ACKNOWLEDGMENTS

The authors acknowledge fruitful discussions with the members of the International Quantum Plasma Initiative (IQPI) collaboration T. Heinzl, A. Ilderton, and D. Seipt, as well as with A. Arefiev, S. V. Bulanov, A. Di Piazza, E. Esarey, C. H. Keitel, J. K. Koga, J. Magnusson, S. P. D. Mangles, C. P. Ridgers, C. B. Schroeder, L. O. Silva, and A. G. R. Thomas. S. S. B. acknowledges the support from the U.S. DOE Office of Science, Offices of HEP and FES (through LaserNetUS), under Contract No. DE-AC02-05CH11231. A. G. acknowledges the support of the Swedish Research Council (Grant No. 2017-05148). M. M. also acknowledges the support of the Swedish Research Council (Grant No. 2020-06768).

REFERENCES

Aaboud, M., *et al.* (ATLAS Collaboration), 2017, Nat. Phys. **13**, 852.
Abraham, M., 1902, Ann. Phys. (Berlin) **315**, 105.
Abramowicz, H., *et al.*, 2019, arXiv:1909.00860.
Abramowicz, H., *et al.*, 2021, Eur. Phys. J. Special Topics **230**, 2445.
Adler, S. L., 1971, Ann. Phys. (N.Y.) **67**, 599.
Adolphsen, C., *et al.*, 2022, arXiv:2201.07895.
Akhmadaliev, S. Z., *et al.*, 2002, Phys. Rev. Lett. **89**, 061802.
Akhmedov, E. K., 1983, Sov. Phys. JETP **58**, 883.
Akhmedov, E. K., 2011, Phys. At. Nucl. **74**, 1299.
Akiyama, K., *et al.* (Event Horizon Telescope Collaboration), 2019, Astrophys. J. **875**, L5.
Albert, F., and A. G. Thomas, 2016, Plasma Phys. Controlled Fusion **58**, 103001.
Alejo, A., G. M. Samarin, J. R. Warwick, and G. Sarri, 2019, Front. Phys. **7**, 49.
Aleksandrov, I. A., D. A. Tumakov, A. Kudlis, V. M. Shabaev, and N. N. Rosanov, 2020, Phys. Rev. A **102**, 023102.
An, X. Y., M. Chen, J. X. Li, S. M. Weng, F. He, Z. M. Sheng, and J. Zhang, 2019, Phys. Plasmas **26**, 123106.
an der Brügge, D., and A. Pukhov, 2010, Phys. Plasmas **17**, 033110.
Andersen, K. K., J. Esberg, H. Knudsen, H. D. Thomsen, U. I. Uggerhøj, P. Sona, A. Mangiarotti, T. J. Ketel, A. Dizdar, and S. Ballestrero (CERN NA63 Collaboration), 2012, Phys. Rev. D **86**, 072001.
Apolonski, A., A. Poppe, G. Tempea, C. Spielmann, T. Udem, R. Holzwarth, T. W. Hänsch, and F. Krausz, 2000, Phys. Rev. Lett. **85**, 740.
Arber, T. D., *et al.*, 2015, Plasma Phys. Controlled Fusion **57**, 113001.
Arefiev, A. V., G. E. Cochran, D. W. Schumacher, A. P. Robinson, and G. Chen, 2015, Phys. Plasmas **22**, 013103.
Arran, C., J. M. Cole, E. Gerstmayr, T. G. Blackburn, S. P. Mangles, and C. P. Ridgers, 2019, Plasma Phys. Controlled Fusion **61**, 074009.
Assous, F., T. Pougeard Dulimbert, and J. Segré, 2003, J. Comput. Phys. **187**, 550.
Babzien, M., *et al.*, 2006, Phys. Rev. Lett. **96**, 054802.
Baier, V. N., and V. M. Katkov, 1968, Sov. Phys. JETP **26**, 854.
Baier, V. N., and V. M. Katkov, 1999, Phys. Rev. D **59**, 056003.
Baier, V. N., and V. M. Katkov, 2005, Phys. Rep. **409**, 261.
Baier, V. N., V. M. Katkov, and V. M. Strakhovenko, 1975a, Sov. Phys. JETP **41**, 198.
Baier, V. N., V. M. Katkov, and V. M. Strakhovenko, 1975b, Sov. Phys. JETP **40**, 225.
Baier, V. N., V. M. Katkov, and V. M. Strakhovenko, 1998, *Electromagnetic Processes at High Energies in Oriented Single Crystals* (World Scientific, Singapore).
Baird, C. D., C. D. Murphy, T. G. Blackburn, A. Ilderton, S. P. Mangles, M. Marklund, and C. P. Ridgers, 2019, New J. Phys. **21**, 053030.
Bamber, C., *et al.*, 1999, Phys. Rev. D **60**, 092004.
Bargmann, V., L. Michel, and V. L. Telegdi, 1959, Phys. Rev. Lett. **2**, 435.
Baring, M. G., and A. K. Harding, 2001, Astrophys. J. **547**, 929.
Bashinov, A. V., and A. V. Kim, 2013, Phys. Plasmas **20**, 113111.
Bashinov, A. V., A. V. Kim, and A. M. Sergeev, 2015, Phys. Rev. E **92**, 043105.
Bashinov, A. V., P. Kumar, and A. V. Kim, 2017, Phys. Rev. A **95**, 042127.
Bashmakov, V. F., E. N. Nerush, I. Y. Kostyukov, A. M. Fedotov, and N. B. Narozhny, 2014, Phys. Plasmas **21**, 013105.

Bassett, I. M., 1986, Opt. Acta **33**, 279.
Bassompierre, G., *et al.*, 1995, Phys. Lett. B **355**, 584.
Bauer, D., P. Mulser, and W. H. Steeb, 1995, Phys. Rev. Lett. **75**, 4622.
Baumann, C., E. N. Nerush, A. Pukhov, and I. Y. Kostyukov, 2019, Sci. Rep. **9**, 9407.
Baumann, C., and A. Pukhov, 2019, Plasma Phys. Controlled Fusion **61**, 074010.
Baur, G., K. Hencken, and D. Trautmann, 2007, Phys. Rep. **453**, 1.
Baur, G., K. Hencken, D. Trautmann, S. Sadovsky, and Y. Kharlov, 2002, Phys. Rep. **364**, 359.
Baylis, W. E., and J. Huschilt, 2002, Phys. Lett. A **301**, 7.
Becker, W., 1977, Physica (Amsterdam) **87A**, 601.
Becker, W., and H. Mitter, 1975, J. Phys. A **8**, 1638.
Behm, K. T., *et al.*, 2018, Rev. Sci. Instrum. **89**, 113303.
Behnke, T., J. E. Brau, B. Foster, J. Fuster, M. Harrison, J. M. Paterson, M. Peskin, M. Stanitzki, N. Walker, and H. Yamamoto, 2013, International Linear Collider Technical Report No. ILC-REPORT-2013-040.
Belkacem, A., *et al.*, 1987, Phys. Rev. Lett. **58**, 1196.
Bell, A. R., and J. G. Kirk, 2008, Phys. Rev. Lett. **101**, 200403.
Benedetti, A., M. Tamburini, and C. H. Keitel, 2018, Nat. Photonics **12**, 319.
Bin, J. H., *et al.*, 2015, Phys. Rev. Lett. **115**, 064801.
Blackburn, T. G., 2020, Rev. Mod. Plasma Phys. **4**, 5.
Blackburn, T. G., E. Gerstmayr, S. P. Mangles, and M. Marklund, 2020, Phys. Rev. Accel. Beams **23**, 064001.
Blackburn, T. G., A. A. Gonoskov, and M. Marklund, 2018, Phys. Rev. A **98**, 023421.
Blackburn, T. G., A. Ilderton, M. Marklund, and C. P. Ridgers, 2019, New J. Phys. **21**, 053040.
Blackburn, T. G., A. J. MacLeod, and B. King, 2021, New J. Phys. **23**, 085008.
Blackburn, T. G., and M. Marklund, 2018, Plasma Phys. Controlled Fusion **60**, 054009.
Blackburn, T. G., C. P. Ridgers, J. G. Kirk, and A. R. Bell, 2014, Phys. Rev. Lett. **112**, 015001.
Blackburn, T. G., D. Seipt, S. S. Bulanov, and M. Marklund, 2018, Phys. Plasmas **25**, 083108.
Blackburn, T. G., D. Seipt, S. S. Bulanov, and M. Marklund, 2020, Phys. Rev. A **101**, 012505.
Blankenbecler, R., and S. D. Drell, 1987, Phys. Rev. D **36**, 277.
Blankenbecler, R., and S. D. Drell, 1988, Phys. Rev. Lett. **61**, 2324.
Boca, M., V. Dinu, and V. Florescu, 2012, Nucl. Instrum. Methods Phys. Res., Sect. B **279**, 12.
Boca, M., and V. Florescu, 2009, Phys. Rev. A **80**, 053403.
Bøgh, E., J. A. Davies, and K. O. Nielsen, 1964, Phys. Lett. **12**, 129.
Boland, M. J., *et al.* (CLIC and CLICdp Collaborations), 2016, Compact Linear Collider Technical Report No. CERN-2016-004.
Bonnor, W. B., 1974, Proc. R. Soc. A **337**, 591.
Bordovitsyn, V. A., I. M. Ternov, and V. G. Bagrov, 1995, Phys. Usp. **38**, 1037.
Bottcher, C., and M. R. Strayer, 1989, Phys. Rev. D **39**, 1330.
Brady, C. S., C. P. Ridgers, T. D. Arber, and A. R. Bell, 2014, Phys. Plasmas **21**, 033108.
Breit, G., and J. A. Wheeler, 1934, Phys. Rev. **46**, 1087.
Bromage, J., *et al.*, 2019, High Power Laser Sci. Eng. **7**, e4.
Brown, L. S., and T. W. Kibble, 1964, Phys. Rev. **133**, A705.
Bula, C., *et al.*, 1996, Phys. Rev. Lett. **76**, 3116.
Bulanov, S. S., E. Esarey, C. B. Schroeder, S. V. Bulanov, T. Z. Esirkepov, M. Kando, F. Pegoraro, and W. P. Leemans, 2015, Phys. Rev. Lett. **114**, 105003.
Bulanov, S. S., E. Esarey, C. B. Schroeder, S. V. Bulanov, T. Z. Esirkepov, M. Kando, F. Pegoraro, and W. P. Leemans, 2016, Phys. Plasmas **23**, 056703.
Bulanov, S. S., T. Z. Esirkepov, A. G. Thomas, J. K. Koga, and S. V. Bulanov, 2010, Phys. Rev. Lett. **105**, 220407.
Bulanov, S. S., A. M. Fedotov, and F. Pegoraro, 2005, Phys. Rev. E **71**, 016404.
Bulanov, S. S., A. Maksimchuk, K. Krushelnick, K. I. Popov, V. Y. Bychenkov, and W. Rozmus, 2010, Phys. Lett. A **374**, 476.
Bulanov, S. S., A. Maksimchuk, C. B. Schroeder, A. G. Zhidkov, E. Esarey, and W. P. Leemans, 2012, Phys. Plasmas **19**, 020702.
Bulanov, S. S., V. D. Mur, N. B. Narozhny, J. Nees, and V. S. Popov, 2010, Phys. Rev. Lett. **104**, 220404.
Bulanov, S. S., N. B. Narozhny, V. D. Mur, and V. S. Popov, 2006, J. Exp. Theor. Phys. **102**, 9.
Bulanov, S. S., C. B. Schroeder, E. Esarey, and W. P. Leemans, 2013, Phys. Rev. A **87**, 062110.
Bulanov, S. S., *et al.*, 2010, Phys. Plasmas **17**, 043105.
Bulanov, S. S., *et al.*, 2012, AIP Conf. Proc. **1507**, 825.
Bulanov, S. V., T. Esirkepov, and T. Tajima, 2003, Phys. Rev. Lett. **91**, 085001.
Bulanov, S. V., T. Z. Esirkepov, M. Kando, S. S. Bulanov, S. G. Rykovanov, and F. Pegoraro, 2013, Phys. Plasmas **20**, 123114.
Bulanov, S. V., T. Z. Esirkepov, M. Kando, J. K. Koga, and S. S. Bulanov, 2011, Phys. Rev. E **84**, 056605.
Bulanov, S. V., T. Z. Esirkepov, M. Kando, A. S. Pirozhkov, and N. N. Rosanov, 2013, Usp. Fiz. Nauk **183**, 449.
Bulanov, S. V., T. Z. Esirkepov, J. Koga, and T. Tajima, 2004, Plasma Phys. Rep. **30**, 196.
Bulanov, S. V., T. Z. Esirkepov, J. K. Koga, S. S. Bulanov, Z. Gong, X. Q. Yan, and M. Kando, 2017, J. Plasma Phys. **83**, 905830202.
Bulanov, S. V., N. M. Naumova, and F. Pegoraro, 1994, Phys. Plasmas **1**, 745.
Bulanov, S. V., P. Sasorov, S. S. Bulanov, and G. Korn, 2019, Phys. Rev. D **100**, 016012.
Bulanov, S. V., J. J. Wilkens, T. Z. Esirkepov, G. Korn, G. Kraft, S. D. Kraft, M. Molls, and V. S. Khoroshkov, 2014, Phys. Usp. **57**, 1149.
Bulanov, S. V., *et al.*, 2011, Nucl. Instrum. Methods Phys. Res., Sect. A **660**, 31.
Burke, D. L., *et al.*, 1997, Phys. Rev. Lett. **79**, 1626.
Burton, D. A., and A. Noble, 2014, Contemp. Phys. **55**, 110.
Caldirola, P., 1979, Riv. Nuovo Cimento Soc. Ital. Fis. **2**, 1.
Capdessus, R., E. d'Humières, and V. T. Tikhonchuk, 2012, Phys. Rev. E **86**, 036401.
Capdessus, R., A. Noble, P. McKenna, and D. A. Jaroszynski, 2016, Phys. Rev. D **93**, 045034.
Capparelli, L. M., A. Damiano, L. Maiani, and A. D. Polosa, 2017, Eur. Phys. J. C **77**, 754.
Cartlidge, E., 2018, Science **359**, 382.
Chang, H., Z. Xu, W. Yao, Y. Xie, and B. Qiao, 2017, Chin. J. Comput. Phys. **34**, 526.
Chang, H. X., B. Qiao, Z. Xu, X. R. Xu, C. T. Zhou, X. Q. Yan, S. Z. Wu, M. Borghesi, M. Zepf, and X. T. He, 2015, Phys. Rev. E **92**, 053107.
Chen, A. Y., F. Cruz, and A. Spitkovsky, 2020, Astrophys. J. **889**, 69.
Chen, H., S. C. Wilks, J. D. Bonlie, E. P. Liang, J. Myatt, D. F. Price, D. D. Meyerhofer, and P. Beiersdorfer, 2009, Phys. Rev. Lett. **102**, 105001.
Chen, H., *et al.*, 2015, Phys. Rev. Lett. **114**, 215001.
Chen, M., E. Esarey, C. G. Geddes, C. B. Schroeder, G. R. Plateau, S. S. Bulanov, S. Rykovanov, and W. P. Leemans, 2013, Phys. Rev. ST Accel. Beams **16**, 030701.

Chen, M., A. Pukhov, T.-P. P. Yu, and Z.-M. M. Sheng, 2011, Plasma Phys. Controlled Fusion **53**, 014004.

Chen, P., 1992, Phys. Rev. D **46**, 1186.

Chen, P., G. Horton-Smith, T. Ohgaki, A. W. Weidemann, and K. Yokoya, 1995, Nucl. Instrum. Methods Phys. Res., Sect. A **355**, 107.

Chen, P., and V. I. Telnov, 1989, Phys. Rev. Lett. **63**, 1796.

Chen, P., and K. Yokoya, 1988, Phys. Rev. D **38**, 987.

Chen, S., *et al.*, 2013, Phys. Rev. Lett. **110**, 155003.

Chen, S. Y., A. Maksimchuk, and D. Umstadter, 1998, Nature (London) **396**, 653.

Chen, Y.-Y., P.-L. He, R. Shaisultanov, K. Z. Hatsagortsyan, and C. H. Keitel, 2019, Phys. Rev. Lett. **123**, 174801.

Ciappina, M. F., S. V. Popruzhenko, S. V. Bulanov, T. Ditmire, G. Korn, and S. Weber, 2019, Phys. Rev. A **99**, 043405.

Cole, J. M., *et al.*, 2018, Phys. Rev. X **8**, 011020.

Compant La Fontaine, A., C. Courtois, E. Lefebvre, J. L. Bourgade, O. Landoas, K. Thorp, and C. Stoeckl, 2013, Phys. Plasmas **20**, 123111.

Corde, S., K. Ta Phuoc, G. Lambert, R. Fitour, V. Malka, A. Rousse, A. Beck, and E. Lefebvre, 2013, Rev. Mod. Phys. **85**, 1.

Crinquand, B., B. Cerutti, A. Philippov, K. Parfrey, and G. Dubus, 2020, Phys. Rev. Lett. **124**, 145101.

Cros, B., and P. Muggli, 2019, arXiv:1901.08436.

Cros, B., *et al.*, 2019, arXiv:1901.10370.

Cruz, F., T. Grismayer, and L. O. Silva, 2021, Astrophys. J. **908**, 149.

Daido, H., M. Nishiuchi, and A. S. Pirozhkov, 2012, Rep. Prog. Phys. **75**, 056401.

Danson, C. N., *et al.*, 2019, High Power Laser Sci. Eng. **7**, e54.

Darwin, C. G., 1928, Proc. R. Soc. A **118**, 654.

Daugherty, J. K., and A. K. Harding, 1982, Astrophys. J. **252**, 337.

Del Gaudio, F., T. Grismayer, R. A. Fonseca, W. B. Mori, and L. O. Silva, 2019, Phys. Rev. Accel. Beams **22**, 023402.

Del Sorbo, D., D. Seipt, T. G. Blackburn, A. G. R. Thomas, C. D. Murphy, J. G. Kirk, and C. P. Ridgers, 2017, Phys. Rev. A **96**, 043407.

Del Sorbo, D., D. Seipt, A. G. R. Thomas, and C. P. Ridgers, 2018, Plasma Phys. Controlled Fusion **60**, 064003.

Del Sorbo, D., *et al.*, 2018, New J. Phys. **20**, 033014.

d'Enterria, D., and G. G. da Silveira, 2013, Phys. Rev. Lett. **111**, 080405.

Dinu, V., C. Harvey, A. Ilderton, M. Marklund, and G. Torgrimsson, 2016, Phys. Rev. Lett. **116**, 044801.

Dinu, V., and G. Torgrimsson, 2018, Phys. Rev. D **97**, 036021.

Dinu, V., and G. Torgrimsson, 2019, Phys. Rev. D **99**, 096018.

Dinu, V., and G. Torgrimsson, 2020, Phys. Rev. D **102**, 016018.

Di Piazza, A., 2008, Lett. Math. Phys. **83**, 305.

Di Piazza, A., 2014, Phys. Rev. Lett. **113**, 040402.

Di Piazza, A., 2016, Phys. Rev. Lett. **117**, 213201.

Di Piazza, A., 2017, Phys. Rev. A **95**, 032121.

Di Piazza, A., 2018, Phys. Lett. B **782**, 559.

Di Piazza, A., K. Z. Hatsagortsyan, and C. H. Keitel, 2008, Phys. Rev. Lett. **100**, 010403.

Di Piazza, A., K. Z. Hatsagortsyan, and C. H. Keitel, 2009, Phys. Rev. Lett. **102**, 254802.

Di Piazza, A., K. Z. Hatsagortsyan, and C. H. Keitel, 2010, Phys. Rev. Lett. **105**, 220403.

Di Piazza, A., and M. A. Lopez-Lopez, 2020, Phys. Rev. D **102**, 076018.

Di Piazza, A., and A. I. Milstein, 2008, Phys. Rev. A **77**, 042102.

Di Piazza, A., A. I. Milstein, and C. H. Keitel, 2007, Phys. Rev. A **76**, 032103.

Di Piazza, A., C. Muller, K. Z. Hatsagortsyan, and C. H. Keitel, 2012, Rev. Mod. Phys. **84**, 1177.

Di Piazza, A., M. Tamburini, S. Meuren, and C. H. Keitel, 2018, Phys. Rev. A **98**, 012134.

Di Piazza, A., M. Tamburini, S. Meuren, and C. H. Keitel, 2019, Phys. Rev. A **99**, 022125.

Di Piazza, A., T. N. Wistisen, M. Tamburini, and U. I. Uggerhøj, 2020, Phys. Rev. Lett. **124**, 044801.

Dirac, P. A. M., 1938, Proc. R. Soc. A **167**, 148.

Dittrich, W., and H. Gies, 2000, *Probing the Quantum Vacuum* (Springer, Berlin).

Dodin, I. Y., and N. J. Fisch, 2008, Phys. Rev. E **77**, 036402.

Döpp, A., E. Guillaume, C. Thaury, J. Gautier, I. Andriyash, A. Lifschitz, V. Malka, A. Rousse, and K. Ta Phuoc, 2016, Plasma Phys. Controlled Fusion **58**, 034005.

Dremin, I. M., 2002, JETP Lett. **76**, 151.

Dromey, B., *et al.*, 2009, Nat. Phys. **5**, 146.

Duclous, R., J. G. Kirk, and A. R. Bell, 2011, Plasma Phys. Controlled Fusion **53**, 015009.

Duff, M. J., R. Capdessus, D. D. Sorbo, C. P. Ridgers, M. King, and P. McKenna, 2018, Plasma Phys. Controlled Fusion **60**, 064006.

Duncan, R. C., and C. Thompson, 1992, Astrophys. J. **392**, L9.

Dunne, G. V., 2005, *From Fields to Strings: Circumnavigating Theoretical Physics: Ian Kogan Memorial Collection*, Vol. 1 (World Scientific, Singapore), pp. 445–522.

Eckmann, J. P., and D. Ruelle, 1985, Rev. Mod. Phys. **57**, 617.

Edwards, J. P., and A. Ilderton, 2021, Phys. Rev. D **103**, 016004.

Efimenko, E. S., A. V. Bashinov, S. I. Bastrakov, A. A. Gonoskov, A. A. Muraviev, I. B. Meyerov, A. V. Kim, and A. M. Sergeev, 2018, Sci. Rep. **8**, 2329.

Efimenko, E. S., A. V. Bashinov, A. A. Gonoskov, S. I. Bastrakov, A. A. Muraviev, I. B. Meyerov, A. V. Kim, and A. M. Sergeev, 2019, Phys. Rev. E **99**, 031201.

Ehlotzky, F., K. Krajewska, and J. Z. Kamiński, 2009, Rep. Prog. Phys. **72**, 046401.

Einstein, A., 1905, Ann. Phys. (Berlin) **322**, 891.

Ekman, R., T. Heinzl, and A. Ilderton, 2021a, New J. Phys. **23**, 055001.

Ekman, R., T. Heinzl, and A. Ilderton, 2021b, Phys. Rev. D **104**, 036002.

Eliezer, C. J., 1943, Proc. Cambridge Philos. Soc. **39**, 173.

Eliezer, C. J., 1948, Proc. R. Soc. A **194**, 543.

Elkina, N. V., A. M. Fedotov, I. Y. Kostyukov, M. V. Legkov, N. B. Narozhny, E. N. Nerush, and H. Ruhl, 2011, Phys. Rev. ST Accel. Beams **14**, 054401.

Erber, T., 1966, Rev. Mod. Phys. **38**, 626.

Esarey, E., S. K. Ride, and P. Sprangle, 1993, Phys. Rev. E **48**, 3003.

Esarey, E., C. B. Schroeder, and W. P. Leemans, 2009, Rev. Mod. Phys. **81**, 1229.

Esirkepov, T., M. Borghesi, S. V. Bulanov, G. Mourou, and T. Tajima, 2004, Phys. Rev. Lett. **92**, 175003.

Esirkepov, T. Z., S. S. Bulanov, J. K. Koga, M. Kando, K. Kondo, N. N. Rosanov, G. Korn, and S. V. Bulanov, 2015, Phys. Lett. A **379**, 2044.

Esirkepov, T. Z., and S. V. Bulanov, 2017, Phys. Lett. A **381**, 2559.

Esirkepov, T. Z., S. V. Bulanov, M. Kando, A. S. Pirozhkov, and A. G. Zhidkov, 2009, Phys. Rev. Lett. **103**, 025002.

Faghihi, D., V. Carey, C. Michoski, R. Hager, S. Janhunen, C. S. Chang, and R. D. Moser, 2020, J. Comput. Phys. **409**, 109317.

Fedotov, A., 2017, J. Phys. Conf. Ser. **826**, 012027.

Fedotov, A. M., N. V. Elkina, E. G. Gelfer, N. B. Narozhny, and H. Ruhl, 2014, Phys. Rev. A **90**, 053847.

Fedotov, A. M., N. B. Narozhny, G. Mourou, and G. Korn, 2010, Phys. Rev. Lett. **105**, 080402.
Flood, S. P., and D. A. Burton, 2015, Phys. Lett. A **379**, 1966.
Foldy, L. L., and S. A. Wouthuysen, 1950, Phys. Rev. **78**, 29.
Ford, G. W., and R. F. O'Connell, 1991, Phys. Lett. A **157**, 217.
Formanek, M., S. Evans, J. Rafelski, A. Steinmetz, and C. T. Yang, 2018, Plasma Phys. Controlled Fusion **60**, 074006.
Frenkel, J., 1926, Z. Phys. **37**, 243.
Fuchs, J., *et al.*, 2006, Nat. Phys. **2**, 48.
Furry, W. H., 1951, Phys. Rev. **81**, 115.
Gahn, C., G. D. Tsakiris, G. Pretzler, K. J. Witte, C. Delfin, C. G. Wahlström, and D. Habs, 2000, Appl. Phys. Lett. **77**, 2662.
Gales, S., *et al.*, 2018, Rep. Prog. Phys. **81**, 094301.
Gaponov, A. V., and M. A. Miller, 1958, Sov. Phys. JETP **7**, 168.
Gaunt, J. A., 1930, Phil. Trans. R. Soc. A **229**, 163, http://www.jstor.org/stable/91269.
Gelfer, E. G., A. A. Mironov, A. M. Fedotov, V. F. Bashmakov, E. N. Nerush, I. Y. Kostyukov, and N. B. Narozhny, 2015, Phys. Rev. A **92**, 022113.
Geng, X. S., L. L. Ji, B. F. Shen, B. Feng, Z. Guo, Q. Yu, L. G. Zhang, and Z. Z. Xu, 2019, Commun. Phys. **2**, 66.
Geng, X. S., *et al.*, 2020, New J. Phys. **22**, 013007.
Gerlach, W., and O. Stern, 1922, Z. Phys. **9**, 349.
Gershtein, S. S., and V. S. Popov, 1973, Lett. Nuovo Cimento Soc. Ital. Fis. **6**, 593.
Ghebregziabher, I., B. A. Shadwick, and D. Umstadter, 2013, Phys. Rev. ST Accel. Beams **16**, 030705.
Gies, H., F. Karbstein, and C. Kohlfürst, 2018, Phys. Rev. D **97**, 036022.
Ginzburg, V. L., and V. N. Tsytovich, 1979, Phys. Rep. **49**, 1.
Goldman, I. I., 1964, Phys. Lett. **8**, 103.
Goldreich, P., and W. H. Julian, 1969, Astrophys. J. **157**, 869.
Gong, Z., R. H. Hu, Y. R. Shou, B. Qiao, C. E. Chen, X. T. He, S. S. Bulanov, T. Z. Esirkepov, S. V. Bulanov, and X. Q. Yan, 2017, Phys. Rev. E **95**, 013210.
Gong, Z., F. Mackenroth, X. Q. Yan, and A. V. Arefiev, 2019, Sci. Rep. **9**, 17181.
Gonoskov, A., 2022, Comput. Phys. Commun. **271**, 108200.
Gonoskov, A., 2018, Phys. Plasmas **25**, 013108.
Gonoskov, A., A. Bashinov, S. Bastrakov, E. Efimenko, A. Ilderton, A. Kim, M. Marklund, I. Meyerov, A. Muraviev, and A. Sergeev, 2017, Phys. Rev. X **7**, 041003.
Gonoskov, A., A. Bashinov, I. Gonoskov, C. Harvey, A. Ilderton, A. Kim, M. Marklund, G. Mourou, and A. Sergeev, 2014, Phys. Rev. Lett. **113**, 014801.
Gonoskov, A., S. Bastrakov, E. Efimenko, A. Ilderton, M. Marklund, I. Meyerov, A. Muraviev, A. Sergeev, I. Surmin, and E. Wallin, 2015, Phys. Rev. E **92**, 023305.
Gonoskov, A., I. Gonoskov, C. Harvey, A. Ilderton, A. Kim, M. Marklund, G. Mourou, and A. Sergeev, 2013, Phys. Rev. Lett. **111**, 060404.
Gonoskov, A., and M. Marklund, 2018, Phys. Plasmas **25**, 093109.
Gonoskov, A. A., A. V. Korzhimanov, A. V. Kim, M. Marklund, and A. M. Sergeev, 2011, Phys. Rev. E **84**, 046403.
Gonoskov, I., A. Aiello, S. Heugel, and G. Leuchs, 2012, Phys. Rev. A **86**, 053836.
Gonsalves, A. J., *et al.*, 2019, Phys. Rev. Lett. **122**, 084801.
Gordienko, S., A. Pukhov, O. Shorokhov, and T. Baeva, 2005, Phys. Rev. Lett. **94**, 103903.
Gordon, W., 1928, Z. Phys. **48**, 11.
Green, D. G., and C. N. Harvey, 2015, Comput. Phys. Commun. **192**, 313.
Grismayer, T., M. Vranic, J. L. Martins, R. A. Fonseca, and L. O. Silva, 2016, Phys. Plasmas **23**, 056706.
Grismayer, T., M. Vranic, J. L. Martins, R. A. Fonseca, and L. O. Silva, 2017, Phys. Rev. E **95**, 023210.
Gu, Y. J., M. Jirka, O. Klimo, and S. Weber, 2019, Matter Radiat. Extremes **4**, 064403.
Gu, Y.-J., O. Klimo, S. V. Bulanov, and S. Weber, 2018, Commun. Phys. **1**, 93.
Haberberger, D., S. Tochitsky, F. Fiuza, C. Gong, R. A. Fonseca, L. O. Silva, W. B. Mori, and C. Joshi, 2012, Nat. Phys. **8**, 95.
Habs, D., M. Hegelich, J. Schreiber, M. Gross, A. Henig, D. Kiefer, and D. Jung, 2008, Appl. Phys. B **93**, 349.
Hadad, Y., L. Labun, J. Rafelski, N. Elkina, C. Klier, and H. Ruhl, 2010, Phys. Rev. D **82**, 096012.
Harding, A. K., and D. Lai, 2006, Rep. Prog. Phys. **69**, 2631.
Har-Shemesh, O., and A. Di Piazza, 2012, Opt. Lett. **37**, 1352.
Hartemann, F. V., W. J. Brown, D. J. Gibson, S. G. Anderson, A. M. Tremaine, P. T. Springer, A. J. Wootton, E. P. Hartouni, and C. P. Barty, 2005, Phys. Rev. ST Accel. Beams **8**, 100702.
Hartin, A., A. Ringwald, and N. Tapia, 2019, Phys. Rev. D **99**, 036008.
Harvey, C., T. Heinzl, N. Iji, and K. Langfeld, 2011, Phys. Rev. D **83**, 076013.
Harvey, C., T. Heinzl, A. Ilderton, and M. Marklund, 2012, Phys. Rev. Lett. **109**, 100402.
Harvey, C. N., 2018, Phys. Rev. Accel. Beams **21**, 114001.
Harvey, C. N., A. Gonoskov, A. Ilderton, and M. Marklund, 2017, Phys. Rev. Lett. **118**, 105004.
Harvey, C. N., A. Gonoskov, M. Marklund, and E. Wallin, 2016, Phys. Rev. A **93**, 022112.
Harvey, C. N., A. Ilderton, and B. King, 2015, Phys. Rev. A **91**, 013822.
He, C. Z., A. Longman, J. A. Pérez-Hernández, M. D. Marco, C. Salgado, G. Zeraouli, G. Gatti, L. Roso, R. Fedosejevs, and W. T. Hill, 2019, Opt. Express **27**, 30020.
He, Y., T. G. Blackburn, T. Toncian, and A. V. Arefiev, 2021, Commun. Phys. **4**, 139.
Heaviside, O., 1902, Nature (London) **67**, 6.
Hebenstreit, F., J. Berges, and D. Gelfand, 2013, Phys. Rev. D **87**, 105006.
Heintzmann, H., and M. Grewing, 1972, Z. Phys. **251**, 77.
Heinzl, T., and A. Ilderton, 2009, Opt. Commun. **282**, 1879.
Heinzl, T., and A. Ilderton, 2017, Phys. Rev. Lett. **118**, 113202.
Heinzl, T., A. Ilderton, and B. King, 2016, Phys. Rev. D **94**, 065039.
Heinzl, T., A. Ilderton, and M. Marklund, 2010, Phys. Lett. B **692**, 250.
Heinzl, T., A. Ilderton, and D. Seipt, 2018, Phys. Rev. D **98**, 016002.
Heinzl, T., B. King, and A. J. Macleod, 2020, Phys. Rev. A **102**, 063110.
Heisenberg, W., and H. Euler, 1936, Z. Phys. **98**, 714.
Henig, A., *et al.*, 2009, Phys. Rev. Lett. **103**, 245003.
Herrera, J. C., 1977, Phys. Rev. D **15**, 453.
Higginson, A., *et al.*, 2018, Nat. Commun. **9**, 724.
Hirotani, K., and H.-Y. Pu, 2016, Astrophys. J. **818**, 50.
Hollebeek, R., 1981, Nucl. Instrum. Methods **184**, 333.
Hooker, C. J., *et al.*, 2006, J. Phys. IV (France) **133**, 673.
Hu, H., C. Müller, and C. H. Keitel, 2010, Phys. Rev. Lett. **105**, 080401.
Huang, T. W., C. M. Kim, C. T. Zhou, M. H. Cho, K. Nakajima, C. M. Ryu, S. C. Ruan, and C. H. Nam, 2019, New J. Phys. **21**, 013008.
Huang, X. G., 2016, Rep. Prog. Phys. **79**, 076302.
Ilderton, A., 2011, Phys. Rev. Lett. **106**, 020404.

Ilderton, A., 2019, Phys. Rev. D **99**, 085002.
Ilderton, A., B. King, and D. Seipt, 2019, Phys. Rev. A **99**, 042121.
Ilderton, A., B. King, and S. Tang, 2020, Phys. Rev. D **102**, 076013.
Ilderton, A., and D. Seipt, 2018, Phys. Rev. D **97**, 016007.
Ilderton, A., and G. Torgrimsson, 2013a, Phys. Rev. D **88**, 025021.
Ilderton, A., and G. Torgrimsson, 2013b, Phys. Lett. B **725**, 481.
Jackson, J. D., 1976, Rev. Mod. Phys. **48**, 417.
Jackson, J. D., 1999, *Classical Electrodynamics*, 3rd ed. (John Wiley & Sons, New York).
Jansen, M. J., J. Z. Kamiński, K. Krajewska, and C. Müller, 2016, Phys. Rev. D **94**, 013010.
Jeandet, A., A. Borot, K. Nakamura, S. W. Jolly, A. J. Gonsalves, C. Tóth, H. S. Mao, W. P. Leemans, and F. Quéré, 2019, J. Phys. Photonics **1**, 35001.
Jeong, T. M., S. V. Bulanov, P. V. Sasorov, S. S. Bulanov, J. K. Koga, and K. Korn, 2020, Opt. Express **28**, 13991.
Jeong, T. M., S. V. Bulanov, P. Valenta, G. Korn, T. Z. Esirkepov, J. K. Koga, A. S. Pirozhkov, M. Kando, and S. S. Bulanov, 2021, Phys. Rev. A **104**, 053533.
Ji, L., A. Pukhov, and B. Shen, 2014, New J. Phys. **16**, 063047.
Ji, L. L., A. Pukhov, I. Y. Kostyukov, B. F. Shen, and K. Akli, 2014, Phys. Rev. Lett. **112**, 145003.
Ji, L. L., J. Snyder, and B. F. Shen, 2019, Plasma Phys. Controlled Fusion **61**, 065019.
Jirka, M., O. Klimo, S. V. Bulanov, T. Z. Esirkepov, E. Gelfer, S. S. Bulanov, S. Weber, and G. Korn, 2016, Phys. Rev. E **93**, 023207.
Jirka, M., O. Klimo, M. Vranic, S. Weber, and G. Korn, 2017, Sci. Rep. **7**, 15302.
Kando, M., T. Esirkepov, J. Koga, A. Pirozhkov, and S. Bulanov, 2018, Quantum Beam Sci. **2**, 9.
Kando, M., *et al.*, 2007, Phys. Rev. Lett. **99**, 135001.
Kaplan, A. E., and A. L. Pokrovsky, 2005, Phys. Rev. Lett. **95**, 053601.
Kar, S., *et al.*, 2012, Phys. Rev. Lett. **109**, 185006.
Kaw, P., and J. Dawson, 1970, Phys. Fluids **13**, 472.
Keldysh, L. V., 1965, Sov. Phys. JETP **20**, 1307.
Kettle, B., *et al.*, 2021, New J. Phys. **23**, 115006.
Khrennikov, K., J. Wenz, A. Buck, J. Xu, M. Heigoldt, L. Veisz, and S. Karsch, 2015, Phys. Rev. Lett. **114**, 195003.
Kibble, T. W., 1966, Phys. Rev. Lett. **16**, 1054.
Kim, H. T., K. H. Pae, H. J. Cha, I. J. Kim, T. J. Yu, J. H. Sung, S. K. Lee, T. M. Jeong, and J. Lee, 2013, Phys. Rev. Lett. **111**, 165002.
Kim, I. J., *et al.*, 2016, Phys. Plasmas **23**, 070701.
King, B., 2015, Phys. Rev. A **91**, 033415.
King, B., and N. Elkina, 2016, Phys. Rev. A **94**, 062102.
King, B., N. Elkina, and H. Ruhl, 2013, Phys. Rev. A **87**, 042117.
King, B., and A. M. Fedotov, 2018, Phys. Rev. D **98**, 016005.
King, B., and T. Heinzl, 2016, High Power Laser Sci. Eng. **4**, e5.
King, B., and H. Hu, 2016, Phys. Rev. D **94**, 125010.
King, B., and H. Ruhl, 2013, Phys. Rev. D **88**, 013005.
King, B., and S. Tang, 2020, Phys. Rev. A **102**, 022809.
Kiriyama, H., *et al.*, 2018, Opt. Lett. **43**, 2595.
Kiriyama, H., *et al.*, 2020, High Energy Density Phys. **36**, 100771.
Kirk, J. G., 2016, Plasma Phys. Controlled Fusion **58**, 085005.
Kirk, J. G., A. R. Bell, and I. Arka, 2009, Plasma Phys. Controlled Fusion **51**, 085008.
Kirk, J. G., A. R. Bell, and C. P. Ridgers, 2013, Plasma Phys. Controlled Fusion **55**, 095016.
Kirsebom, K., U. Mikkelsen, E. Uggerhøj, K. Elsener, S. Ballestrero, P. Sona, and Z. Z. Vilakazi, 2001, Phys. Rev. Lett. **87**, 054801.
Kiselev, S., A. Pukhov, and I. Kostyukov, 2004, Phys. Rev. Lett. **93**, 135004.
Klepikov, N. P., 1985, Sov. Phys. Usp. **28**, 506.
Kneip, S., *et al.*, 2009, Phys. Rev. Lett. **103**, 035002.
Koga, J., 2004, Phys. Rev. E **70**, 046502.
Koga, J., T. Z. Esirkepov, and S. V. Bulanov, 2005, Phys. Plasmas **12**, 093106.
Koga, J. K., and T. Hayakawa, 2017, Phys. Rev. Lett. **118**, 204801.
Kostyukov, I., S. Kiselev, and A. Pukhov, 2003, Phys. Plasmas **10**, 4818.
Kostyukov, I. Y., and E. N. Nerush, 2016, Phys. Plasmas **23**, 093119.
Krajewska, K., and J. Z. Kamiński, 2012, Phys. Rev. A **86**, 052104.
Krajewska, K., and J. Z. Kamiński, 2013, Laser Part. Beams **31**, 503.
Krajewska, K., and J. Z. Kamiński, 2014, Phys. Rev. A **90**, 052117.
Krausz, F., and M. Ivanov, 2009, Rev. Mod. Phys. **81**, 163.
Kravets, Y., A. Noble, and D. Jaroszynski, 2013, Phys. Rev. E **88**, 011201.
Krivitski, V. S., and V. N. Tsytovich, 1991, Sov. Phys. Usp. **34**, 250.
Kulagin, V. V., V. A. Cherepenin, M. S. Hur, and H. Suk, 2007, Phys. Rev. Lett. **99**, 124801.
Kuznetsov, A. V., T. Z. Esirkepov, F. F. Kamenets, and S. V. Bulanov, 2001, Plasma Phys. Rep. **27**, 211.
Landau, L. D., and E. M. Lifshitz, 1981, *Quantum Mechanics: Non-Relativistic Theory*, Course of Theoretical Physics Vol. 3 (Butterworth-Heinemann, Oxford).
Landau, L. D., and E. M. Lifshitz, 1987, *The Classical Theory of Fields*, Course of Theoretical Physics Vol. 2 (Butterworth-Heinemann, Oxford).
Lapenta, G., and J. U. Brackbill, 1994, J. Comput. Phys. **115**, 213.
Lapenta, G., and J. U. Brackbill, 1995, Comput. Phys. Commun. **87**, 139.
Larmor, J., 1897, London Edinburgh Dublin Philos. Mag. J. Sci. **44**, 503.
Lawson, J. D., 1979, IEEE Trans. Nucl. Sci. **26**, 4217.
Leemans, W. P., *et al.*, 2014, Phys. Rev. Lett. **113**, 245002.
Lehmann, G., and K. H. Spatschek, 2012, Phys. Rev. E **85**, 056412.
Li, J. X., Y. Y. Chen, K. Z. Hatsagortsyan, and C. H. Keitel, 2018, Phys. Rev. Lett. **120**, 124803.
Li, J. X., K. Z. Hatsagortsyan, B. J. Galow, and C. H. Keitel, 2015, Phys. Rev. Lett. **115**, 204801.
Li, Y. F., Y. Y. Chen, W. M. Wang, and H. S. Hu, 2020, Phys. Rev. Lett. **125**, 044802.
Li, Y. F., R. T. Guo, R. Shaisultanov, K. Z. Hatsagortsyan, and J. X. Li, 2019, Phys. Rev. Applied **12**, 014047.
Li, Y. F., R. Shaisultanov, Y. Y. Chen, F. Wan, K. Z. Hatsagortsyan, C. H. Keitel, and J. X. Li, 2020, Phys. Rev. Lett. **124**, 014801.
Li, Y. F., R. Shaisultanov, K. Z. Hatsagortsyan, F. Wan, C. H. Keitel, and J. X. Li, 2019, Phys. Rev. Lett. **122**, 154801.
Liang, E., *et al.*, 2015, Sci. Rep. **5**, 13968.
Liénard, A., 1898, Éclairage Électr. **16**, 5.
Lindhard, J., 1964, Phys. Lett. **12**, 126.
Lindhard, J., 1991, Phys. Rev. A **43**, 6032.
Link, A., *et al.*, 2006, Rev. Sci. Instrum. **77**, 10E723.
Liseykina, T. V., S. V. Popruzhenko, and A. Macchi, 2016, New J. Phys. **18**, 072001.
Liu, J.-J., T.-P. Yu, Y. Yin, X.-L. Zhu, and F.-Q. Shao, 2016, Opt. Express **24**, 15978.
Lobet, M., X. Davoine, E. D'Humières, and L. Gremillet, 2017, Phys. Rev. Accel. Beams **20**, 043401.
Lobet, M., E. D'Humieres, M. Grech, C. Ruyer, X. Davoine, and L. Gremillet, 2016, J. Phys. Conf. Ser. **688**, 012058.
Lorentz, H. A., 1892, Arch. Neerl. Sci. Exactes Nat. **25**, 363.
Lorentz, H. A., 1904, *Encyklopädie der Mathematischen Wissenschaften*, Vol. 14 (Gauthier-Villars, Villiers-sur-Orge, France), p. 145.

Lötstedt, E., and U. D. Jentschura, 2009, Phys. Rev. Lett. **103**, 110404.
Lundh, O., *et al.*, 2011, Nat. Phys. **7**, 219.
Luo, W., W. Y. Liu, T. Yuan, M. Chen, J. Y. Yu, F. Y. Li, D. Del Sorbo, C. P. Ridgers, and Z. M. Sheng, 2018, Sci. Rep. **8**, 8400.
Luo, W., Y. B. Zhu, H. B. Zhuo, Y. Y. Ma, Y. M. Song, Z. C. Zhu, X. D. Wang, X. H. Li, I. C. Turcu, and M. Chen, 2015, Phys. Plasmas **22**, 063112.
Luu, P. T., T. Tückmantel, and A. Pukhov, 2016, Comput. Phys. Commun. **202**, 165.
Lv, Q. Z., E. Raicher, C. H. Keitel, and K. Z. Hatsagortsyan, 2021, Phys. Rev. Research **3**, 013214.
Macchi, A., M. Borghesi, and M. Passoni, 2013, Rev. Mod. Phys. **85**, 751.
Mackenroth, F., and A. Di Piazza, 2011, Phys. Rev. A **83**, 032106.
Mackenroth, F., and A. Di Piazza, 2013, Phys. Rev. Lett. **110**, 070402.
Mackenroth, F., and A. Di Piazza, 2018, Phys. Rev. D **98**, 116002.
Mackenroth, F., A. Di Piazza, and C. H. Keitel, 2010, Phys. Rev. Lett. **105**, 063903.
Mackenroth, F., A. Gonoskov, and M. Marklund, 2016, Phys. Rev. Lett. **117**, 104801.
Mackenroth, F., and A. R. Holkundkar, 2019, Sci. Rep. **9**, 19607.
Mackenroth, F., A. R. Holkundkar, and H. P. Schlenvoigt, 2019, New J. Phys. **21**, 123028.
Mackenroth, F., N. Kumar, N. Neitz, and C. H. Keitel, 2019, Phys. Rev. E **99**, 033205.
Macleod, A. J., A. Noble, and D. A. Jaroszynski, 2019, Phys. Rev. Lett. **122**, 161601.
Magnusson, J., A. Gonoskov, M. Marklund, T. Z. Esirkepov, J. K. Koga, K. Kondo, M. Kando, S. V. Bulanov, G. Korn, and S. S. Bulanov, 2019, Phys. Rev. Lett. **122**, 254801.
Magnusson, J., *et al.*, 2019, Phys. Rev. A **100**, 063404.
Mahajan, S. M., F. A. Asenjo, and R. D. Hazeltine, 2015, Mon. Not. R. Astron. Soc. **446**, 4112.
Maier, A. R., *et al.*, 2020, Phys. Rev. X **10**, 031039.
Mainfray, G., and G. Manus, 1991, Rep. Prog. Phys. **54**, 1333.
Maksimchuk, A., S. Gu, K. Flippo, D. Umstadter, and A. Y. Bychenkov, 2000, Phys. Rev. Lett. **84**, 4108.
Mane, S. R., Y. M. Shatunov, and K. Yokoya, 2005, Rep. Prog. Phys. **68**, 1997.
Marklund, M., and P. K. Shukla, 2006, Rev. Mod. Phys. **78**, 591.
Martin, R. S., and J. L. Cambier, 2016, J. Comput. Phys. **327**, 943.
Martinez, B., E. D'Humières, and L. Gremillet, 2020, Phys. Rev. Research **2**, 043341.
Martins, J. L., S. F. Martins, R. A. Fonseca, and L. O. Silva, 2009, in *Harnessing Relativistic Plasma Waves as Novel Radiation Sources from Terahertz to X-Rays and Beyond*, edited by D. A. Jaroszynski and A. Rousse, SPIE Proceedings Vol. 7359 (SPIE—International Society for Optical Engineering, Bellingham, WA), p. 73590V.
Martins, J. L., M. Vranic, T. Grismayer, J. Vieira, R. A. Fonseca, and L. O. Silva, 2016, Plasma Phys. Controlled Fusion **58**, 014035.
Martins, S. F., J. P. Santos, R. A. Fonseca, and L. O. Silva, 2004, Phys. Scr. **2004**, 118.
Marx, G., 1966, Nature (London) **211**, 22.
Matlis, N. H., *et al.*, 2006, Nat. Phys. **2**, 749.
Mendonça, J. T., 1983, Phys. Rev. A **28**, 3592.
Meuren, S., 2019, in *Proceedings of the FACET-II Science Workshop, Menlo Park, CA, 2019*, https://conf.slac.stanford.edu/facet-2-2019/sites/facet-2-2019.conf.slac.stanford.edu/files/basic-page-docs/sfqed_2019.pdf.
Meuren, S., P. H. Bucksbaum, N. J. Fisch, F. Fiúza, S. Glenzer, M. J. Hogan, K. Qu, D. A. Reis, G. White, and V. Yakimenko, 2020, arXiv:2002.10051.
Meuren, S., and A. Di Piazza, 2011, Phys. Rev. Lett. **107**, 260401.
Meuren, S., C. H. Keitel, and A. Di Piazza, 2016, Phys. Rev. D **93**, 085028.
Meyer-ter-Vehn, J., and H. C. Wu, 2009, Eur. Phys. J. D **55**, 433.
Mignani, R. P., V. Testa, D. González Caniulef, R. Taverna, R. Turolla, S. Zane, and K. Wu, 2017, Mon. Not. R. Astron. Soc. **465**, 492.
Milstein, A. I., and M. Schumacher, 1994, Phys. Rep. **243**, 183.
Mironov, A. A., S. Meuren, and A. M. Fedotov, 2020, Phys. Rev. D **102**, 053005.
Mironov, A. A., N. B. Narozhny, and A. M. Fedotov, 2014, Phys. Lett. A **378**, 3254.
Mitter, H., 1975, in *Electromagnetic Interactions and Field Theory*, edited by P. O. Urban (Springer, Vienna), pp. 397–468.
Mo, T. C., and C. H. Papas, 1971, Phys. Rev. D **4**, 3566.
Morley, P. D., and D. J. Buettner, 2015, Astropart. Phys. **62**, 7.
Morozov, D. A., and N. B. Narozhnyi, 1977, Sov. Phys. JETP **45**, 44.
Morozov, D. A., N. B. Narozhnyi, and V. I. Ritus, 1981, Sov. Phys. JETP **53**, 1103.
Mourou, G. A., T. Tajima, and S. V. Bulanov, 2006, Rev. Mod. Phys. **78**, 309.
Muraviev, A., A. Bashinov, E. Efimenko, A. Gonoskov, I. Meyerov, and A. Sergeev, 2021, Phys. Rev. E **104**, 065201.
Muraviev, A., A. Bashinov, E. Efimenko, V. Volokitin, I. Meyerov, and A. Gonoskov, 2021, Comput. Phys. Commun. **262**, 107826.
Muraviev, A. A., S. I. Bastrakov, A. V. Bashinov, A. A. Gonoskov, E. S. Efimenko, A. V. Kim, I. B. Meyerov, and A. M. Sergeev, 2015, JETP Lett. **102**, 148.
Nakamura, T., 2020, Phys. Rev. E **102**, 033210.
Nakamura, T., J. K. Koga, T. Z. Esirkepov, M. Kando, G. Korn, and S. V. Bulanov, 2012, Phys. Rev. Lett. **108**, 195001.
Narozhny, N. B., 1979, Phys. Rev. D **20**, 1313.
Narozhny, N. B., 1980, Phys. Rev. D **21**, 1176.
Narozhny, N. B., S. S. Bulanov, V. D. Mur, and V. S. Popov, 2004a, Phys. Lett. A **330**, 1.
Narozhny, N. B., S. S. Bulanov, V. D. Mur, and V. S. Popov, 2004b, JETP Lett. **80**, 382.
Narozhny, N. B., and M. S. Fofanov, 2000, J. Exp. Theor. Phys. **90**, 753.
Narozhnyi, N. B., 1969, Sov. Phys. JETP **28**, 371.
Narozhnyi, N. B., and M. S. Fofanov, 1996, Sov. Phys. JETP **83**, 14.
Narozhnyi, N. B., A. I. Nikishov, and V. I. Ritus, 1965, Sov. Phys. JETP **20**, 662.
National Academies of Sciences, Engineering, and Medicine, 2018, *Opportunities in Intense Ultrafast Lasers: Reaching for the Brightest Light* (National Academies Press, Washington, DC).
Naumova, N. M., J. A. Nees, I. V. Sokolov, B. Hou, and G. A. Mourou, 2004, Phys. Rev. Lett. **92**, 063902.
Nees, J., *et al.*, 2020, in *Proceedings of the Conference on Lasers and Electro-Optics, Washington, DC, 2020* (Optical Society of America, Washington, DC), p. JW2B.9.
Neitz, N., and A. Di Piazza, 2013, Phys. Rev. Lett. **111**, 054802.
Nerush, E. N., and I. Y. Kostyukov, 2015, Plasma Phys. Controlled Fusion **57**, 035007.
Nerush, E. N., I. Y. Kostyukov, A. M. Fedotov, N. B. Narozhny, N. V. Elkina, and H. Ruhl, 2011, Phys. Rev. Lett. **106**, 035001.
Niel, F., C. Riconda, F. Amiranoff, R. Duclous, and M. Grech, 2018, Phys. Rev. E **97**, 043209.
Nikishov, A. I., and V. I. Ritus, 1964, Sov. Phys. JETP **19**, 529.
Noble, R. J., 1987, Nucl. Instrum. Methods Phys. Res., Sect. A **256**, 427.
Okun', L. B., 1991, Sov. Phys. Usp. **161**, 177.

Olausen, S. A., and V. M. Kaspi, 2014, Astrophys. J. Suppl. Ser. **212**, 6.
Oleinik, V., 1967, Sov. Phys. JETP **25**, 697.
Palaniyappan, S., *et al.*, 2012, Nat. Phys. **8**, 763.
Palmer, R. B., 1995, AIP Conf. Proc. **335**, 90.
Panek, P., J. Z. Kamiński, and F. Ehlotzky, 2002, Phys. Rev. A **65**, 022712.
Papadopoulos, D. N., *et al.*, 2016, High Power Laser Sci. Eng. **4**, e34.
Pariente, G., V. Gallet, A. Borot, O. Gobert, and F. Quéré, 2016, Nat. Photonics **10**, 547.
Pfeiffer, M., A. Mirza, C. D. Munz, and S. Fasoulas, 2015, Comput. Phys. Commun. **191**, 9.
Philippov, A., A. Timokhin, and A. Spitkovsky, 2020, Phys. Rev. Lett. **124**, 245101.
Pike, O. J., F. MacKenroth, E. G. Hill, and S. J. Rose, 2014, Nat. Photonics **8**, 434.
Pirozhkov, A. S., *et al.*, 2007, Phys. Plasmas **14**, 123106.
Poder, K., *et al.*, 2018, Phys. Rev. X **8**, 031004.
Podszus, T., and A. Di Piazza, 2019, Phys. Rev. D **99**, 076004.
Popov, V. S., 2001, Phys. At. Nucl. **64**, 367.
Popov, V. S., 2004, Phys. Usp. **47**, 855.
Popruzhenko, S. V., T. V. Liseykina, and A. Macchi, 2019, New J. Phys. **21**, 033009.
Pryce, M. H. L., 1938, Proc. R. Soc. A **168**, 389.
Quéré, F., and H. Vincenti, 2021, High Power Laser Sci. Eng. **9**, e6.
Quesnel, B., and P. Mora, 1998, Phys. Rev. E **58**, 3719.
Raicher, E., and S. Eliezer, 2013, Phys. Rev. A **88**, 022113.
Raicher, E., S. Eliezer, and A. Zigler, 2015, Phys. Lett. B **750**, 76.
Raicher, E., and K. Z. Hatsagortsyan, 2020, Phys. Rev. Research **2**, 013240.
Reinhardt, J., and W. Greiner, 1977, Rep. Prog. Phys. **40**, 219.
Reiss, H. R., 1962, J. Math. Phys. (N.Y.) **3**, 59.
Reiss, H. R., 1971, Phys. Rev. Lett. **26**, 1072.
Reiss, H. R., 1979, Phys. Rev. A **19**, 1140.
Reville, B., and J. G. Kirk, 2010, Astrophys. J. **724**, 1283.
Ridgers, C. P., C. S. Brady, R. Duclous, J. G. Kirk, K. Bennett, T. D. Arber, and A. R. Bell, 2013, Phys. Plasmas **20**, 056701.
Ridgers, C. P., C. S. Brady, R. Duclous, J. G. Kirk, K. Bennett, T. D. Arber, A. P. Robinson, and A. R. Bell, 2012, Phys. Rev. Lett. **108**, 165006.
Ridgers, C. P., J. G. Kirk, R. Duclous, T. G. Blackburn, C. S. Brady, K. Bennett, T. D. Arber, and A. R. Bell, 2014, J. Comput. Phys. **260**, 273.
Ridgers, C. P., *et al.*, 2017, J. Plasma Phys. **83**, 715830502.
Rimbault, C., P. Bambade, O. Dadoun, G. Le Meur, F. Touze, M. D. C. Alabau, and D. Schulte, 2007, in *Proceedings of the IEEE Particle Accelerator Conference, Albuquerque, 2007*, edited by C. Petit-Jean-Genaz (IEEE, New York), pp. 2728–2730.
Ritus, V. I., 1970, JETP Lett. **12**, 289.
Ritus, V. I., 1972a, Ann. Phys. (N.Y.) **69**, 555.
Ritus, V. I., 1972b, Nucl. Phys. **B44**, 236.
Ritus, V. I., 1985, J. Sov. Laser Res. **6**, 497.
Rjasanow, S., T. Schreiber, and W. Wagner, 1998, J. Comput. Phys. **145**, 382.
Rjasanow, S., and W. Wagner, 1996, J. Comput. Phys. **124**, 243.
Rohrlich, F., 2007, *Classical Charged Particles* (World Scientific, Singapore).
Rosanov, N. N., 2021, JETP Lett. **113**, 145.
Rousse, A., *et al.*, 2004, Phys. Rev. Lett. **93**, 135005.
Ruffini, R., G. Vereshchagin, and S. S. Xue, 2010, Phys. Rep. **487**, 1.
Rykovanov, S. G., C. G. Geddes, C. B. Schroeder, E. Esarey, and W. P. Leemans, 2016, Phys. Rev. Accel. Beams **19**, 030701.
Sakai, Y., *et al.*, 2015, Phys. Rev. ST Accel. Beams **18**, 060702.
Samarin, G. M., M. Zepf, and G. Sarri, 2018, J. Mod. Opt. **65**, 1362.
Sampath, A., and M. Tamburini, 2018, Phys. Plasmas **25**, 083104.
Samsonov, A. S., E. N. Nerush, and I. Y. Kostyukov, 2018, Phys. Rev. A **98**, 053858.
Samsonov, A. S., E. N. Nerush, and I. Y. Kostyukov, 2019, Sci. Rep. **9**, 11133.
Sarachik, E. S., and G. T. Schappert, 1970, Phys. Rev. D **1**, 2738.
Sarri, G., *et al.*, 2013, Phys. Rev. Lett. **110**, 255002.
Sarri, G., *et al.*, 2014, Phys. Rev. Lett. **113**, 224801.
Sarri, G., *et al.*, 2015, Nat. Commun. **6**, 6747.
Sauter, F., 1931, Z. Phys. **69**, 742.
Schael, S., *et al.* (ALEPH, DELPHI, L3, and OPAL Collaborations), 2013, Phys. Rep. **532**, 119.
Schlegel, T., and V. T. Tikhonchuk, 2012, New J. Phys. **14**, 073034.
Schnell, M., *et al.*, 2012, Phys. Rev. Lett. **108**, 075001.
Schoeffler, K. M., T. Grismayer, D. Uzdensky, R. A. Fonseca, and L. O. Silva, 2019, Astrophys. J. **870**, 49.
Schumacher, M., 1999, Radiat. Phys. Chem. **56**, 101.
Schwinger, J., 1949, Phys. Rev. **75**, 1912.
Schwinger, J., 1951, Phys. Rev. **82**, 664.
Schwinger, J., 1954, Proc. Natl. Acad. Sci. U.S.A. **40**, 132.
Schwinger, J., W. y. Tsai, and T. Erber, 1976, Ann. Phys. (N.Y.) **96**, 303.
Schwoerer, H., B. Liesfeld, H. P. Schlenvoigt, K. U. Amthor, and R. Sauerbrey, 2006, Phys. Rev. Lett. **96**, 014802.
Seipt, D., 2017, in *Proceedings of the Helmholtz International Summer School 2016: Quantum Field Theory at the Limits: From Strong Fields to Heavy Quarks, Dubna, Russian, 2016*, edited by A. Ali, D. Blaschke, A. Issadykov, and M. Ivanov, p. 24, https://bib-pubdb1.desy.de/record/330321.
Seipt, D., D. Del Sorbo, C. P. Ridgers, and A. G. Thomas, 2018, Phys. Rev. A **98**, 023417.
Seipt, D., D. Del Sorbo, C. P. Ridgers, and A. G. R. Thomas, 2019, Phys. Rev. A **100**, 061402(R).
Seipt, D., T. Heinzl, M. Marklund, and S. S. Bulanov, 2017, Phys. Rev. Lett. **118**, 154803.
Seipt, D., and B. Kämpfer, 2011, Phys. Rev. A **83**, 022101.
Seipt, D., and B. Kämpfer, 2012, Phys. Rev. D **85**, 101701.
Seipt, D., and B. Kämpfer, 2013, Phys. Rev. A **88**, 012127.
Seipt, D., V. Kharin, S. Rykovanov, A. Surzhykov, and S. Fritzsche, 2016, J. Plasma Phys. **82**, 655820203.
Seipt, D., V. Y. Kharin, and S. G. Rykovanov, 2019, Phys. Rev. Lett. **122**, 204802.
Seipt, D., and B. King, 2020, Phys. Rev. A **102**, 052805.
Seipt, D., C. P. Ridgers, D. D. Sorbo, and A. G. R. Thomas, 2021, New J. Phys. **23**, 053025.
Seipt, D., S. G. Rykovanov, A. Surzhykov, and S. Fritzsche, 2015, Phys. Rev. A **91**, 033402.
Seipt, D., and A. G. Thomas, 2019, Plasma Phys. Controlled Fusion **61**, 074005.
Şengül, M. Y., M. C. Güçlü, O. Mercan, and N. G. Karakuş, 2016, Eur. Phys. J. C **76**, 428.
Shen, B., Z. Bu, J. Xu, T. Xu, L. Ji, R. Li, and Z. Xu, 2018, Plasma Phys. Controlled Fusion **60**, 044002.
Shen, C. S., and D. White, 1972, Phys. Rev. Lett. **28**, 455.
Sheng, Z. M., K. Mima, Y. Sentoku, M. S. Jovanović, T. Taguchi, J. Zhang, and J. Meyer-ter-Vehn, 2002, Phys. Rev. Lett. **88**, 055004.
Shi, Y., 2019, Ann. Phys. (N.Y.) **405**, 130.
Shi, Y., J. Xiao, H. Qin, and N. J. Fisch, 2018, Phys. Rev. E **97**, 053206.
Shore, G. M., 2007, Nucl. Phys. **B778**, 219.
Silenko, A. J., 2008, Phys. Rev. A **77**, 012116.

Slade-Lowther, C., D. Del Sorbo, and C. P. Ridgers, 2019, New J. Phys. **21**, 013028.

Snavely, R. A., *et al.*, 2000, Phys. Rev. Lett. **85**, 2945.

Sokolov, A. A., N. P. Klepikov, and I. M. Ternov, 1953, Dokl. Akad. Nauk SSSR **89**, 665.

Sokolov, A. A., and I. M. Ternov, 1968, *Synchrotron Radiation* (Pergamon Press, Oxford).

Sokolov, I. V., 2009, J. Exp. Theor. Phys. **109**, 207.

Sokolov, I. V., N. M. Naumova, and J. A. Nees, 2011, Phys. Plasmas **18**, 093109.

Sokolov, I. V., N. M. Naumova, J. A. Nees, and G. A. Mourou, 2010, Phys. Rev. Lett. **105**, 195005.

Song, H.-H., W.-M. Wang, J.-X. Li, Y.-F. Li, and Y.-T. Li, 2019, Phys. Rev. A **100**, 033407.

Sørensen, A. H., 1996, Nucl. Instrum. Methods Phys. Res., Sect. B **119**, 2.

Spohn, H., 2000, Europhys. Lett. **50**, 287.

Stark, D. J., T. Toncian, and A. V. Arefiev, 2016, Phys. Rev. Lett. **116**, 185003.

Strickland, D., and G. Mourou, 1985, Opt. Commun. **56**, 219.

Sturrock, P. A., 1971, Astrophys. J. **164**, 529.

Sun, C., and Y. K. Wu, 2011, Phys. Rev. ST Accel. Beams **14**, 044701.

Sung, J. H., H. W. Lee, J. Y. Yoo, J. W. Yoon, C. W. Lee, J. M. Yang, Y. J. Son, Y. H. Jang, S. K. Lee, and C. H. Nam, 2017, Opt. Lett. **42**, 2058.

Tajima, T., and J. M. Dawson, 1979, Phys. Rev. Lett. **43**, 267.

Tamburini, M., A. Di Piazza, and C. H. Keitel, 2017, Sci. Rep. **7**, 5694.

Tamburini, M., F. Pegoraro, A. Di Piazza, C. H. Keitel, T. V. Liseykina, and A. MacChi, 2011, Nucl. Instrum. Methods Phys. Res., Sect. A **653**, 181.

Tamburini, M., F. Pegoraro, A. Di Piazza, C. H. Keitel, and A. MacChi, 2010, New J. Phys. **12**, 123005.

Tang, S., M. A. Bake, H. Y. Wang, and B. S. Xie, 2014, Phys. Rev. A **89**, 022105.

Tang, S., B. King, and H. Hu, 2020, Phys. Lett. B **809**, 135701.

Tangtartharakul, K., G. Chen, and A. Arefiev, 2021, J. Comput. Phys. **434**, 110233.

Ta Phuoc, K., S. Corde, C. Thaury, V. Malka, A. Tafzi, J. P. Goddet, R. C. Shah, S. Sebban, and A. Rousse, 2012, Nat. Photonics **6**, 308.

Ternov, I. M., Y. M. Loskutov, and L. I. Korovina, 1962, Sov. Phys. JETP **14**, 1294.

Terzić, B., K. Deitrick, A. S. Hofler, and G. A. Krafft, 2014, Phys. Rev. Lett. **112**, 074801.

Teubner, U., and P. Gibbon, 2009, Rev. Mod. Phys. **81**, 445.

Thomas, A. G. R., 2010, Phys. Rev. ST Accel. Beams **13**, 020702.

Thomas, A. G. R., C. P. Ridgers, S. S. Bulanov, B. J. Griffin, and S. P. D. Mangles, 2012, Phys. Rev. X **2**, 041004.

Thomas, J., A. Hützen, A. Lehrach, A. Pukhov, L. Ji, Y. Wu, X. Geng, and M. Büscher, 2020, Phys. Rev. Accel. Beams **23**, 064401.

Thomas, L. H., 1926, Nature (London) **117**, 514.

Timokhin, A. N., 2010, Mon. Not. R. Astron. Soc. **408**, 2092.

Timokhin, A. N., and A. K. Harding, 2015, Astrophys. J. **810**, 144.

Titov, A. I., and B. Kämpfer, 2020, Eur. Phys. J. D **74**, 218.

Titov, A. I., B. Kämpfer, H. Takabe, and A. Hosaka, 2013, Phys. Rev. A **87**, 042106.

Titov, A. I., H. Takabe, B. Kämpfer, and A. Hosaka, 2012, Phys. Rev. Lett. **108**, 240406.

Torgrimsson, G., 2020, Phys. Rev. D **102**, 116008.

Torgrimsson, G., 2021, Phys. Rev. Lett. **127**, 111602.

Trebino, R., K. W. DeLong, D. N. Fittinghoff, J. N. Sweetser, M. A. Krumbügel, B. A. Richman, and D. J. Kane, 1997, Rev. Sci. Instrum. **68**, 3277.

Tsai, Y. S., 1974, Rev. Mod. Phys. **46**, 815.

Tuchin, K., 2013, Adv. High Energy Phys. 490495.

Turcu, I. C. E., *et al.*, 2016, Rom. Rep. Phys. **68**, S145.

Uggerhøj, U. I., 2005, Rev. Mod. Phys. **77**, 1131.

U.S. Department of Energy, 2016, Technical Report No. 1358081, https://www.osti.gov/biblio/1358081.

Utsunomiya, H., S. Hashimoto, and S. Miyamoto, 2015, Nucl. Phys. News **25**, 25.

Vais, O. E., A. G. Thomas, A. M. Maksimchuk, K. Krushelnick, and V. Y. Bychenkov, 2020, New J. Phys. **22**, 023003.

Vieira, J., C. K. Huang, W. B. Mori, and L. O. Silva, 2011, Phys. Rev. ST Accel. Beams **14**, 071303.

Vincenti, H., 2019, Phys. Rev. Lett. **123**, 105001.

Vincenti, H., S. Monchocé, S. Kahaly, G. Bonnaud, P. Martin, and F. Quéré, 2014, Nat. Commun. **5**, 3403.

Vlasov, A. A., 1938, J. Exp. Theor. Phys. **8**, 291.

Volokitin, V., S. Bastrakov, A. Bashinov, E. Efimenko, A. Muraviev, A. Gonoskov, and I. Meyerov, 2020, J. Phys. Conf. Ser. **1640**, 012015.

Vranic, M., R. A. Fonseca, and L. O. Silva, 2018, Plasma Phys. Controlled Fusion **60**, 034002.

Vranic, M., T. Grismayer, R. A. Fonseca, and L. O. Silva, 2016, New J. Phys. **18**, 073035.

Vranic, M., T. Grismayer, R. A. Fonseca, and L. O. Silva, 2017, Plasma Phys. Controlled Fusion **59**, 014040.

Vranic, M., T. Grismayer, J. L. Martins, R. A. Fonseca, and L. O. Silva, 2015, Comput. Phys. Commun. **191**, 65.

Vranic, M., T. Grismayer, S. Meuren, R. A. Fonseca, and L. O. Silva, 2019, Phys. Plasmas **26**, 053103.

Vranic, M., O. Klimo, G. Korn, and S. Weber, 2018, Sci. Rep. **8**, 4702.

Vranic, M., J. L. Martins, R. A. Fonseca, and L. O. Silva, 2016, Comput. Phys. Commun. **204**, 141.

Vranic, M., J. L. Martins, J. Vieira, R. A. Fonseca, and L. O. Silva, 2014, Phys. Rev. Lett. **113**, 134801.

Vshivkov, V. A., N. M. Naumova, F. Pegoraro, and S. V. Bulanov, 1998, Phys. Plasmas **5**, 2727.

Wagner, F., *et al.*, 2016, Phys. Rev. Lett. **116**, 205002.

Wallin, E., A. Gonoskov, C. Harvey, O. Lundh, and M. Marklund, 2017, J. Plasma Phys. **83**, 905830208.

Wallin, E., A. Gonoskov, and M. Marklund, 2015, Phys. Plasmas **22**, 033117.

Wan, F., R. Shaisultanov, Y.-F. Li, K. Z. Hatsagortsyan, C. H. Keitel, and J.-X. Li, 2020, Phys. Lett. B **800**, 135120.

Wang, H. Y., X. Q. Yan, and M. Zepf, 2015, Phys. Plasmas **22**, 093103.

Wang, W. M., P. Gibbon, Z. M. Sheng, Y. T. Li, and J. Zhang, 2017, Phys. Rev. E **96**, 013201.

Wang, X., *et al.*, 2013, Nat. Commun. **4**, 1988.

Warwick, J., *et al.*, 2017, Phys. Rev. Lett. **119**, 185002.

Weber, S., *et al.*, 2017, Matter Radiat. Extremes **2**, 149.

Weinberg, S., 1995, *The Quantum Theory of Fields* (Cambridge University Press, Cambridge, England).

Welch, D. R., T. C. Genoni, R. E. Clark, and D. V. Rose, 2007, J. Comput. Phys. **227**, 143.

Weller, H. R., M. W. Ahmed, H. Gao, W. Tornow, Y. K. Wu, M. Gai, and R. Miskimen, 2009, Prog. Part. Nucl. Phys. **62**, 257.

Wen, M., H. Bauke, and C. H. Keitel, 2016, Sci. Rep. **6**, 31624.

Wen, M., C. H. Keitel, and H. Bauke, 2017, Phys. Rev. A **95**, 042102.

Wen, M., M. Tamburini, and C. H. Keitel, 2019, Phys. Rev. Lett. **122**, 214801.
Wiechert, E., 1900, Arch. Neerl. Sci. Exactes Nat. **5**, 549.
Wilks, S. C., W. L. Kruer, M. Tabak, and A. B. Langdon, 1992, Phys. Rev. Lett. **69**, 1383.
Wilks, S. C., A. B. Langdon, T. E. Cowan, M. Roth, M. Singh, S. Hatchett, M. H. Key, D. Pennington, A. MacKinnon, and R. A. Snavely, 2001, Phys. Plasmas **8**, 542.
Wistisen, T. N., A. Di Piazza, H. V. Knudsen, and U. I. Uggerhøj, 2018, Nat. Commun. **9**, 795.
Wistisen, T. N., A. Di Piazza, C. F. Nielsen, A. H. Sørensen, and U. I. Uggerhøj, 2019, Phys. Rev. Research **1**, 033014.
Wolkow, D. M., 1935, Z. Phys. **94**, 250.
Wu, D., B. Qiao, and X. T. He, 2015, Phys. Plasmas **22**, 093108.
Wu, Y., *et al.*, 2018, Phys. Plasmas **25**, 093101.
Yakimenko, V., *et al.*, 2019a, Phys. Rev. Accel. Beams **22**, 101301.
Yakimenko, V., *et al.*, 2019b, Phys. Rev. Lett. **122**, 190404.
Yan, W., *et al.*, 2017, Nat. Photonics **11**, 514.
Yano, M., A. Zhidkov, J. K. Koga, T. Hosokai, and R. Kodama, 2019, Phys. Plasmas **26**, 093108.
Yanovsky, V., *et al.*, 2008, Opt. Express **16**, 2109.
Yoffe, S. R., Y. Kravets, A. Noble, and D. A. Jaroszynski, 2015, New J. Phys. **17**, 053025.
Yoffe, S. R., A. Noble, A. J. Macleod, and D. A. Jaroszynski, 2016, Nucl. Instrum. Methods Phys. Res., Sect. A **829**, 243.
Yokoya, K., 1986, Nucl. Instrum. Methods Phys. Res., Sect. A **251**, 1.
Yokoya, K., and P. Chen, 1992, in *Frontiers of Particle Beams: Intensity Limitations*, edited by M. Dienes (Springer, Berlin), pp. 415–445.
Yoon, J. W., Y. G. Kim, I. Choi, J. H. Sung, H. W. Lee, S. K. Lee, and C. H. Nam, 2021, Optica **8**, 630.
Zander, F. A., 1924, Technika i Zhizn **13**, 15.
Zel'Dovich, Y. B., 1975, Sov. Phys. Usp. **18**, 79.
Zhang, P., S. S. Bulanov, D. Seipt, A. V. Arefiev, and A. G. Thomas, 2020, Phys. Plasmas **27**, 050601.
Zhang, P., C. P. Ridgers, and A. G. Thomas, 2015, New J. Phys. **17**, 043051.
Zhang, S., 2013, Prog. Theor. Exp. Phys. 123A01.
Zhu, X. L., Y. Yin, T. P. Yu, F. Q. Shao, Z. Y. Ge, W. Q. Wang, and J. J. Liu, 2015, New J. Phys. **17**, 053039.
Zhu, X. L., T. P. Yu, M. Chen, S. M. Weng, and Z. M. Sheng, 2018, New J. Phys. **20**, 083013.
Zhu, X. L., T. P. Yu, Z. M. Sheng, Y. Yin, I. C. E. Turcu, and A. Pukhov, 2016, Nat. Commun. **7**, 13686.